UNIVERSITY OF TRENTO

Doctoral School in Civil, Environmental and
Mechanical Engineering

Curriculum 2. Mechanics, Materials, Chemistry and Energy

Teferi Sitotaw Yallew

Design and application of MEMS platforms for micromanipulation

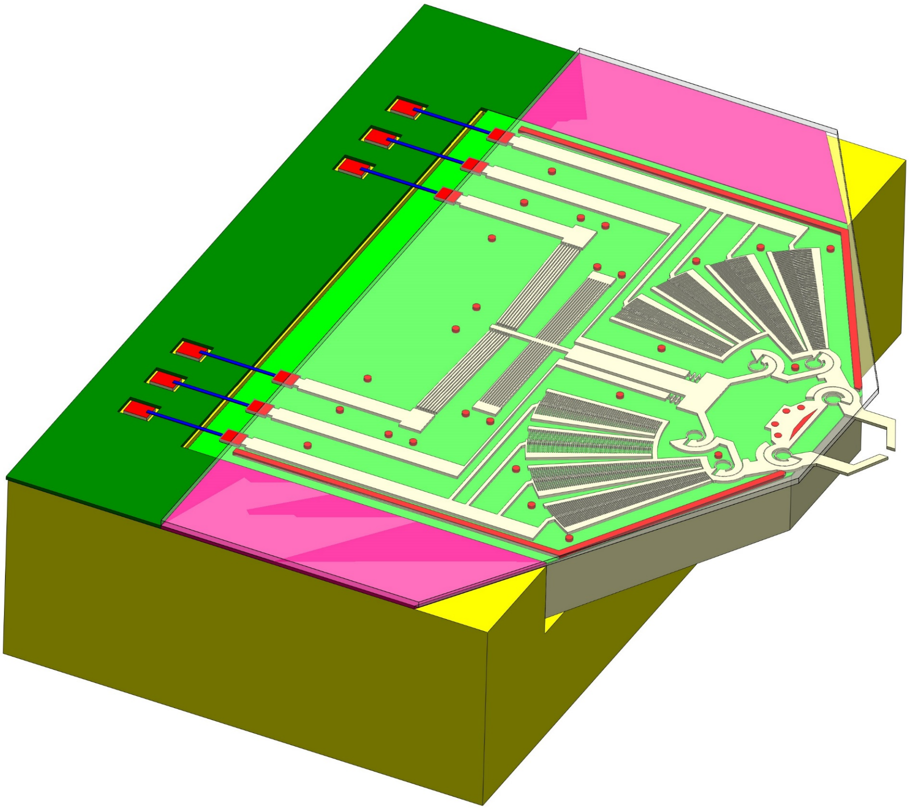

The designed microgripper with its packaging system

2023 – Doctoral thesis

UNIVERSITY OF TRENTO - Italy
Department of Civil, Environmental and Mechanical Engineering

Doctoral School in Civil, Environmental and Mechanical Engineering
Topic 2. Mechanics, Materials, Chemistry and Energy – 35º cycle 2019/2024

Doctoral Thesis – January 2024

Teferi Sitotaw Yallew

Design and application of MEMS platforms for micromanipulation

Supervisors

Ass. Prof. Maria F. Pantano, University of Trento (Unitn)
Mr. Alvise Bagolini, Foundation Bruno Kessler (FBK)

University of Trento
Doctoral School in Civil, Environmental and Mechanical Engineering
http://web.unitn.it/en/dricam
Via Mesiano 77, I-38123 Trento
Tel. +39 0461 282670 / 2611 - *dicamphd@unitn.it*

Acknowledgments

I am extremely grateful for the countless blessings and guidance I have received throughout my PhD journey. Above all, I want to express my deepest appreciation to the Almighty God for giving me strength and countless opportunities. Your grace has been a guiding force in my life, shaping my path and giving me the resilience to overcome challenges.

I am incredibly thankful to my esteemed supervisors, Ass. Prof. Maria F. Pantano and Mr. Alvise Bagolini, for their valuable guidance, support, and unwavering belief in me. Their mentorship has not only enhanced my skills, but also motivated me to aim for even more remarkable accomplishments.

I would like to sincerely thank Foundation of Bruno Kessler (FBK) for providing the necessary research facilities and resources that are crucial for the advancement of my study. Furthermore, I am deeply grateful to the University of Trento for giving me the invaluable opportunity to pursue my studies and for awarding me scholarships that have played a vital role in facilitating my educational journey.

I want to express my heartfelt appreciation to all my friends from the University of Trento and FBK (Foundation of Bruno Kessler). Their companionship and support have been a tremendous source of strength. Your presence has brought happiness, laughter, and shared experiences into my life, making every challenge easier and every success more fulfilling. In particular, I want to express my gratitude to my best friend, Naga Manikanta K., for being by my side throughout this journey, from the very beginning to the end.

Last but certainly not least, I extend my deepest gratitude to my beloved family. Their enduring love, sacrifices, and unwavering faith in me have been the foundation of my journey. Your support has been a constant motivation, inspiring me to pursue my dreams and conquer obstacles.

Abstract

The exploration of Microelectromechanical systems (MEMS) represents a crucial aspect in the advancement of modern science and technology. They offer low-cost solutions to miniaturize numerous devices. The increasing use of MEMS applications in biological research has created a pressing need for reliable micromanipulation tools. In this context, microgrippers have emerged as promising tools for the precise handling and characterization of biological samples. This thesis presents a novel biocompatible microgripper that utilizes electrothermal actuation integrated with a rotary capacitive position sensor. To overcome the limited displacement possibilities associated with electrothermal actuators, this microgripper incorporates conjugate surface flexure hinges (CSFH). These hinges enhance the desired tweezers output displacement. The designed microgripper can in principle manipulate biological samples ranging in size from 15 to 120 µm. Based on the sensitivity calculation of the rotary capacitive position sensors, the sensitivity of the displacement measurement is 102 $fF/\mu m$. By employing a kinematics modeling approach based on the pseudo-rigid-body method (PRBM), an equation for the displacement amplification factor is developed, and this equation is subsequently verified through FEM-based simulations. By comparing the amplification ratio value obtained from the analytical modeling and simulations, there is an excellent match, with a relative difference of only ~1%, thus demonstrating the effectiveness of the PRBM approach in modeling the kinematics of the structure under investigation. In addition to this, by using analytical modeling based on finite elements method (FEM), the design of the electrothermal actuator and the heat dissipation mechanism is optimized. FEM-based simulations are used to validate the theoretical modeling, demonstrating good agreement between the displacements derived from analytical modeling and simulations. The temperature difference (ΔT) across a range from room temperature to 278°C exhibits a relative difference of ~2.8%. Moreover, underpass technology is implemented to ensure that electrical signals or disturbances from other parts of the device, such as the electrothermal actuation system, do not interfere with the operation and integrity of the gripping mechanism. Ultimately, the microgripper is fabricated using conventional MEMS technology from a silicon-on-insulator (SOI) wafer through the deep reactive ion etching (DRIE) technique. The integration of theoretical modeling, simulations, and practical fabrication highlights a compelling approach that has the potential for transformative applications in the field of micromanipulation and biological sample handling.

Furthermore, we propose a C-shaped structure with a curved beam mechanism to improve the movement provided by the thermal actuators. The design of experiment (DOE) method is used to optimize the geometrical parameters of our proposed device. Analytical modeling based on Castigliano's second theorem and finite element method (FEM) simulations are used to predict the behavior of the symmetrical C-shaped structure; the results are in good agreement. The MEMS-based rotational structures are fabricated on silicon-on-insulator (SOI) wafers using bulk micromachining and deep reactive ion etching (DRIE). The fabricated devices are tested; our findings reveal that our proposed MEMS rotational structure outperforms the symmetrical lancet structure by 28% in terms of delivered displacement. Furthermore, the experimental results agree well with those obtained through numerical analysis.

Contents

Introduction

Mechanical manipulation and biological sample characterization are essential activities in biological and medicinal research. Traditional biological sample manipulation and characterization approaches do not provide adequate precision and performance due to the microscale size and highly fragile nature of the materials involved.

Microelectromechanical systems are widely recognized as highly valuable tools for advancing biological sample manipulation, analysis and characterization. Their unique characteristics, including size compatibility with single cells and the capability to quantify microscale motions and forces, make them particularly well-suited for various applications in the life sciences [1].

This thesis presents a novel MEMS-based microgripper that can be used to manipulate and characterize biological samples.

Biological samples can be manipulated using either contact-based or contactless methods [2]–[4]. Mechanical contact (microgripper) systems and optical field approaches (optical trapping forces for cell refraction and optical tweezers for cell reorientation) are examples of contact-based methods. Magnetic, electric, acoustic, and hydrodynamic fields are examples of contactless methods.

Contact-based manipulation methods are widely utilized in micromanipulation systems. The mechanical contact between the object and the system allows for a controlled gripping force. These methods are particularly advantageous for pick and place operations. However, they can encounter issues with releasing due to problems with adhesive force (the force that holds two materials together at their surfaces). On the other hand, contactless manipulation methods provide the advantage of not generating any adhesion forces between the object and the system. Nevertheless, the blocking forces applied to the object are weak and the gripping forces remain uncontrollable. Moreover, these techniques are typically designed for the manipulation of objects with specific physical properties [5]. The papers [6]–[10] provide comprehensive insights in-depth on various manipulation techniques.

1.1. Microelectromechanical Systems (MEMS)

MEMS is a technique used to fabricate miniature integrated devices containing mechanical and electrical elements. These devices are produced through the utilization of batch-processing integrated circuits (IC) and can vary in size from a few micrometers to millimeters. Moreover, they have the ability to sense, control, and actuate mechanical processes on a small scale, and can operate individually or together to produce effects on a larger scale [11]. In the broadest sense, MEMS consist of microsensors, microactuators, and microelectronics, all seamlessly integrated onto a single silicon chip. Microsensors have the role of detecting changes in the system's surroundings by measuring mechanical, thermal, magnetic, chemical, or electromagnetic signals. These signals are then processed by microelectronics technology, which in turn triggers the microactuators to react and make adjustments to the physical environment [12].

MEMS devices effectively replace large actuators and sensors with equivalents that are only a few microns in size. These equivalents can be produced in large numbers using the same fabrication process used for integrated circuits. Consequently, they provide significant enhancements, including lower cost, reduced bulk and weight, and reduced power consumption. At the same time, they greatly improve performance, production volume, and functionality by several orders of magnitude [13].

1.1.1. Applications

The competitive advantage of MEMS devices over other options has already been proven through the successful commercialization of various MEMS devices in different areas. Ever since the initial introduction of a MEMS device, MEMS technology has rapidly expanded into numerous fields of engineering, physical sciences, biology, and medicine. Figure 1 provides a partial summary of various current or potential fields where MEMS and its associated devices can be applied.

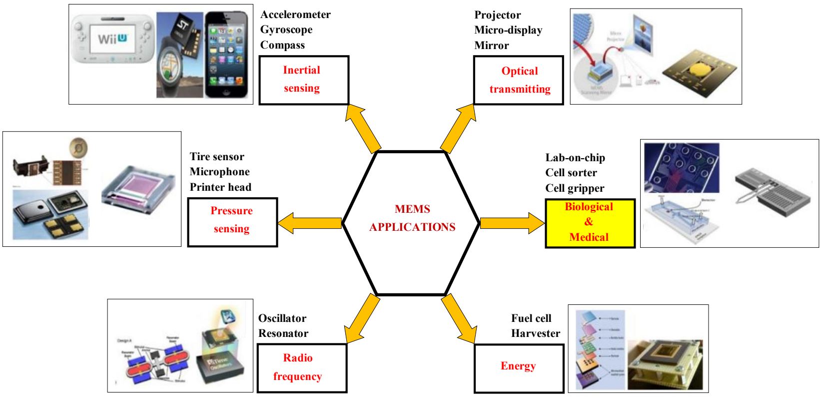

Figure 1. Applications of MEMS in a wide range of fields [14].

1.2. Dissertation Outline

This thesis presents the design, analysis, and application of MEMS microgripper and C-shaped rotating device for micromanipulation and displacement amplification, respectively. This thesis body is divided into seven chapters. The first chapter provides an overview of MEMS, its potential applications, and the fundamental background knowledge required to understand the thesis context. The second chapter focuses on an in-depth review of existing microgripper designs and the ongoing development of micromanipulation systems. This chapter discusses various actuating, sensing, and displacement amplification mechanisms used in MEMS devices. The design and FEM-based analysis of the proposed MEMS micro-gripper are presented in Chapter 3. Simulations are conducted to evaluate the device performance, including numerical calculations to determine the capacitive sensor sensitivity. Analytical modeling and FEM-based simulations are included in Chapter 4 to further analyze the performance of the microgripper, actuation system, and heat dissipation mechanism. Chapter 5 discusses the design of a novel C-shaped hinge and compares its performance to that of other existing device. In Chapter 6, the practical aspects of the research are described in detail, including the fabrication of the microgripper and the C-shaped hinge.

The experimental characterization of these devices describes how they were tested and the results obtained. Additionally, this chapter includes an initial design for the packaging system of the microgripper. Chapter 7 of the thesis summarizes the key findings of the research presented in the thesis, as well as the implications of the findings and future research suggestions.

Literature review

2.1. MEMS Microgripper Designs

Microgrippers are micro-sized devices that have been developed to manipulate objects at the micrometer scale. These devices have various applications, including pick-and-place of biological samples [15], biological materials characterization [16], and microassembly [17], [18]. During the design phase, it is crucial to consider certain gripper characteristics to ensure the proper operation of the device. These characteristics include the type of actuator, power consumption, compliant mechanisms' geometry (which facilitates force and motion transmission through elastic body deformation), the shape of gripping jaws, displacement and force range available at jaws, and material type [19].

In the literature, Several MEMS-based platforms that are based on MEMS technology have been reported, which have different geometry [20], actuators and sensors [21].

Regarding the actuation system, various types of microactuators have been proposed. The most commonly used are electrostatic, piezoelectric, electromagnetic and electrothermal actuators. The performance of the microgripper is reliant on the type of actuator utilized. Different MEMS actuation options have been reported in the literature [22]. Thin film piezoelectric microactuators provide fast response, high accuracy and large output force but require high actuation voltages, have small output displacement. Electromagnetic microactuators require an external magnetic field, typically exhibit a bulky dimension and provide low output force. Capacitive actuators are the state of the art for micromanipulation but they require high operating voltage, which becomes dangerous for living cells and makes technically difficult to operate in the aqueous environment. Moreover, these actuators occupy a large area that is not favored in a compact integrated system. Electrothermal microactuators have a more compact structure, and are able to provide a large force under a relatively low voltage. However, the induced high temperature during operation may restrict their applications in manipulating temperature sensitive materials such as handling biological specimens. Moreover, electrothermal actuation only provides relatively small displacements.

In order to achieve a significant increase in output displacement from the microgripper, it is essential to include a magnification stage between the actuator and the gripper. Amplification mechanisms [23], [24] based on complaint structures are becoming increasingly important in MEMS applications, particularly in situations where precision, reliability, accuracy, and compactness are required. Micro-flexures and hinges provide many advantages for displacement amplification designs, including motion repeatability, and the absence of backlash and lubrication [25]–[28].

Due to the delicate nature of biological cells, they are sensitive to applied forces and pressures. Research findings [29] has indicated that the maximum cell breakdown force is only a few micronewtons. The study in [30] highlights that a strain change between 72-76% can result in the cell bursting. Therefore, it is crucial to utilize a position/a force sensor along with high resolution, sensitivity and accuracy to prevent excessive force from being applied to the sample during the gripping process. Several types of sensors have been proposed for microgrippers [31]. For instance, the optical sensing method was reported in [32], [33] but the overall measuring setup is bulky and expensive. Additionally, when working in liquids, the method presents significant challenges due to light beam refraction and distortion. In [34]–[36], electrothermally and electrostatically actuated microgrippers, and in [37], [38] a hybrid microgripper designs with piezoresistive force sensors are introduced. Nevertheless, these sensors exhibit a high degree of sensitivity towards fluctuations in both temperature and size. Furthermore, their complicated assembly process can impose certain constraints on their overall performance. A magnetically actuated gripper with piezoelectric force sensing is reported in [39]. The spatial resolution of these sensors is poor since drift occurs with the presence of static forces based on the working principle of piezoelectric sensors. This type of sensor is often utilized for dynamic force sensing rather than static force sensing.

2.1.1. Construction of the microgripper

2.1.1.1. Conventional mechanisms

Conventional mechanisms made of rigid bodies have been used for a long time as the backbone of countless mechanical systems, enabling a wide range of functions and movements. These mechanisms usually consist of several intricately designed parts that perform their intended tasks with accuracy. Consequently, they encounter issues such as backlash, wear, an increase in the number of parts, concerns about weight, higher costs for assembly, longer assembly times, and the need for regular maintenance [40], [41].

A rigid-link gripper [42] is a type of robotic end-effector or manipulator designed to grasp and manipulate objects with a set of rigid links and pin joints. This gripper uses solid, unyielding components for grasping and holding as shown in Figure 2.

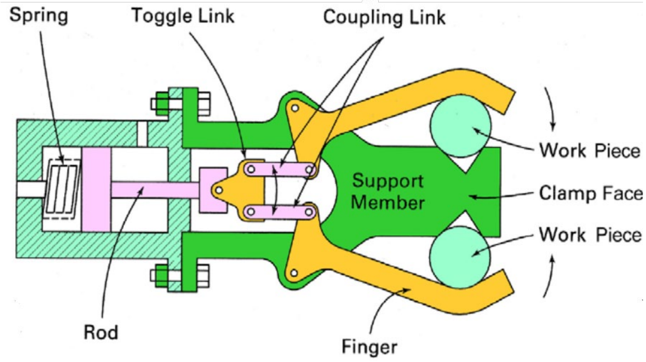

Figure 2. Conventional rigid-link gripper mechanism [42].

2.1.1.2. Compliant mechanisms

Compliant mechanisms are an interesting category of mechanical systems that differ from conventional rigid-body mechanisms in variety of ways. These benefits include simplified manufacturing, lower assembly costs, absence of wear and backlash, reduced noise, easier maintenance, elimination of the need for lubrication, scalability, and enhanced accuracy [43]. They achieve motion, force transmission, or other desired functions through the elastic deformation of their flexible parts, commonly referred to as flexure hinges. The notch type of flexible rotating pair is commonly used and has the advantages of a simple structure and manufacturing process.

However, it has a limited range of motion and the rotation angle typically does not exceed 5°. The notch-type flexible hinge encompasses circular, rectangular, elliptical, and chamfered types, distinguished by their respective hinge cut contours [44]. Various microgripper models are presented, which are equipped with a notch-type hinges, as shown in Figure 3 (a) – (d).

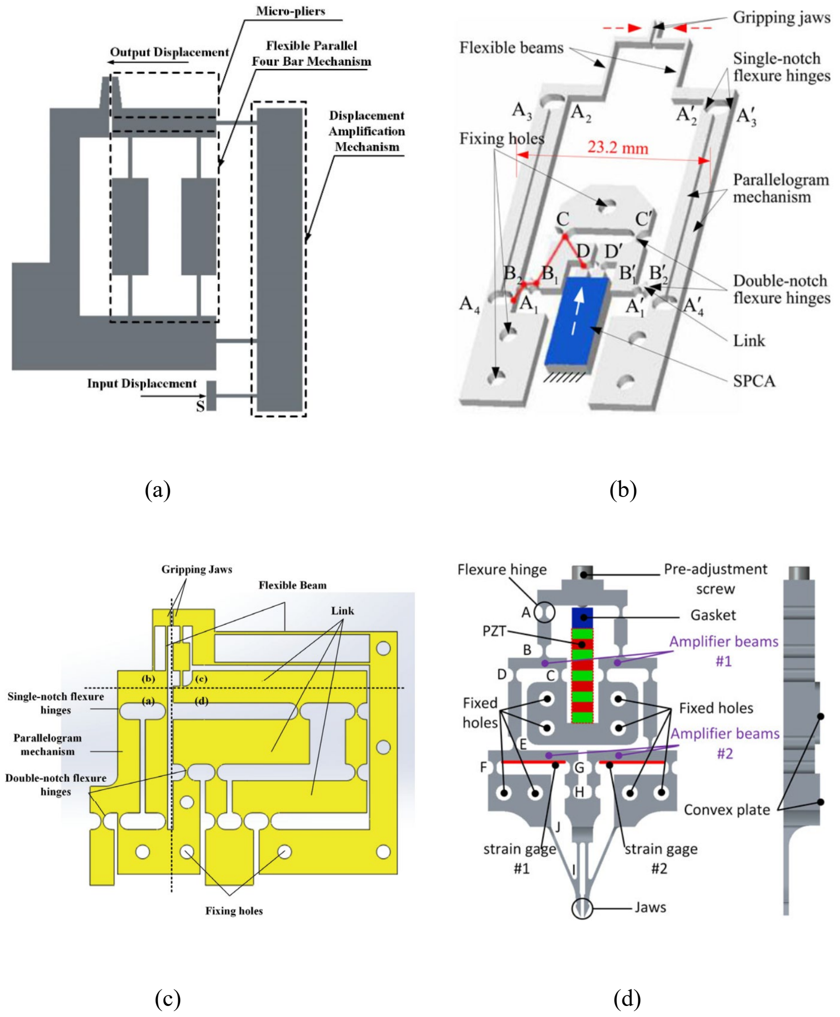

Figure 3. Microgripper mechanisms based on a notch-type hinges. (a) microgripper with single lever mechanism [45], (b) microgripper with L-shaped lever and levered parallelograms [46], (c) microgripper with different lever mechanisms [47], and (d) microgripper with symmetrical dual-stage lever mechanisms [48].

The conjugate surface flexure hinge (CSFH) is a new type of flexure hinge that was recently introduced [49]. The CSFH combines a curved beam as the flexible component with a pair of conjugate surfaces, in order to enhance motion accuracy and increase resistance to yielding. This hinge can be built as a unified monolithic body and easily integrated into any MEMS mechanical framework. The CSFH provides significant advantages such as reduced internal stresses, increased motion range, robustness in operation, and improved overall relative rotations of the hinge [50]. CSFH based microgripper [51], [52] is shown in Figure 4 (a) and (b).

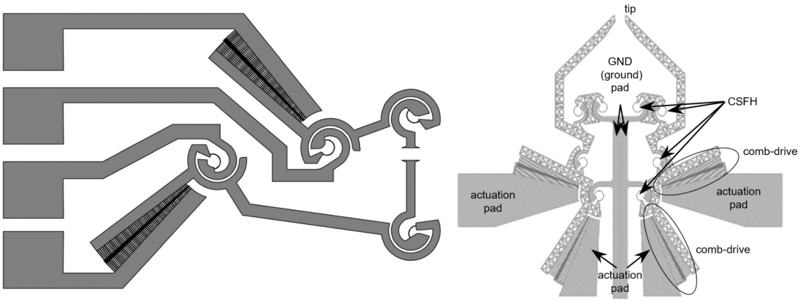

(a) (b)

Figure 4. (a) CSFH based microgrippers embedding rotary comb-drive actuators [51], and (b) Overall geometry of the proposed CSFH- based four-bar linkage microgripper with co-operative electrostatic actuation [52].

2.2. Actuation mechanisms in MEMS

A microactuator is a miniature device that transforms a specific quantity of energy, usually electrical or thermal energy, into mechanical motion. These actuators are designed to operate at the microscale, making them suitable for precision tasks and applications in micro- and nanotechnology.

In micromanipulation, a microactuator plays a crucial role in the functionality of the micromanipulator device. Its primary function is to produce a suitable magnitude of force and displacement, which enables the precise and controlled manipulation of delicate microscale objects.

Given that micromanipulation involves physical interactions with small and fragile objects, achieving the necessary levels of accuracy and precision can be challenging for an unaided human hand. The microactuator, as a critical component of the micromanipulator, provides the necessary reliability and accuracy to carry out effective micromanipulation tasks. Any uncertainty or instability in the actuator's performance could result in damage to the microscale objects or hinder the completion of the desired manipulation tasks. As a result, ensuring the actuator's reliability and sufficient accuracy is fundamental to the success of micromanipulation.

In general, the selection of a microactuator depends on the specific requirements and limitations of the given application. Among several types of microactuators, the most important microactuators are electrostatic, piezoelectric, electrothermal, and electromagnetic actuators via Lorentz forces (commonly used, e.g., in micromirrors) [53].

2.2.1. Electrostatic Actuator

The electrostatic actuators operate on the principle of electrostatic force, which is generated when there is a potential difference between two conductive surfaces. Upon application of a voltage, the electrostatic force either attracts or repels the surfaces, resulting in movement of the actuator. Depending on the arrangement of the electrodes, the most commonly used electrostatic actuators are based on either simple parallel-plate capacitors or comb-drive configuration of multiple interdigitated or non-interdigitated fingers [54].

Parallel plate actuators are composed of two plates that are parallel to each other and are separated by an insulator. When an electrical voltage is applied to these plates, an electric field is generated, which produces electrostatic forces that lead to the plates either attracting or repelling each other. This electrostatic force has the potential to cause the plates to move, resulting in the activation of the device. The top plate that can be moved is connected to an elastic support system, which generates the force for the return stroke through the vertical z-axis. On the other hand, the lower plate that is fixed remains unmovable with respect to the ground as depicted in Figure 5.

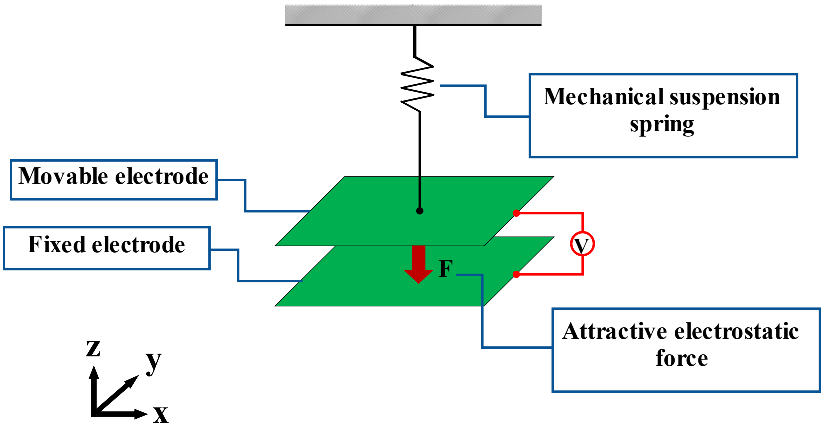

Figure 5. Schematic diagram of electrostatic actuation with a parallel plate actuator configuration.

The primary drawback and constraint of parallel-plate actuators is their limited actuation stroke and output force reliance on the gap size between electrodes. When functioning in an attractive mode, the maximum output force increases as the gap between electrodes is minimized. However, the minimal gap size is restricted by the collapse (pull in) effect [55].

Comb drive actuators are comprised of two sets of interdigitated comb-shaped electrodes. One of the sets remains fixed, while the other is movable and suspended by the mechanical structure above the stationary set as shown in Figure 6. The movable comb structure has the capacity to move parallel to the stationary set. Upon applying a voltage between the comb structures, electrostatic force is generated among the interdigitated fingers. This force has the capability to attract or repel the movable structure in relation to the stationary structure. The electrostatic force can be controlled by varying the applied voltage, leading to the displacement of the movable comb structure.

The resulting motion is useful for generating linear or rotational motion.

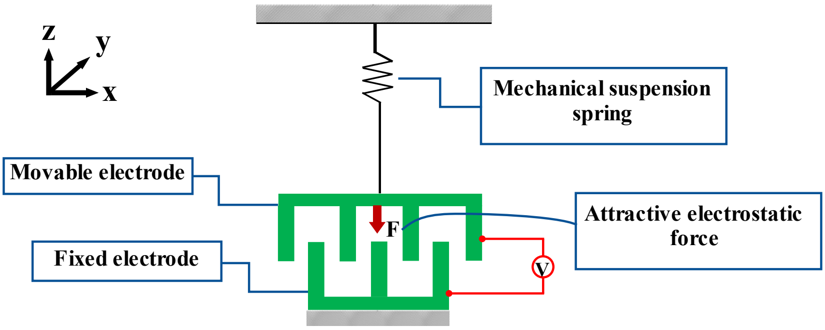

Figure 6. Schematic diagram of electrostatic actuation with a comb drive actuator configuration.

The most significant disadvantages of comb-drive actuators are a requirement for high driving voltage, a limited displacement in direct current driving mode and a large layout area [56].

A microgripper based on parallel-plate actuator [57] has been proposed, as depicted in Figure 7. It is worth noting that the range of usability for displacing the actuator's structures is restricted to a fraction of the total gap between the plates. This limitation has been imposed to prevent the structures from collapsing. Nevertheless, this poses a significant challenge in applications that require precise position control. Moreover, a microgripper with a comb drive actuator has been developed with the design of linear [58] and rotary [59] configurations as shown in Figure 8 and 9 but a high driving voltage is required to reach the maximum displacement.

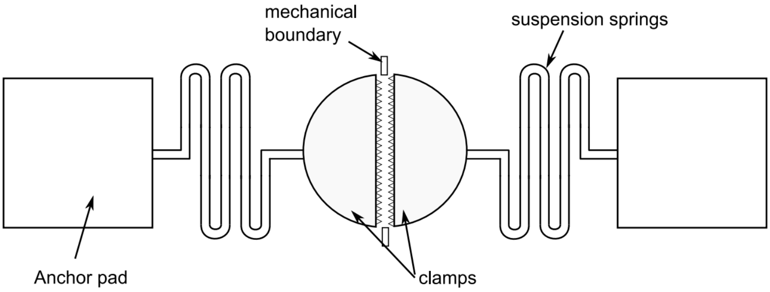

Figure 7. Schematic diagram of parallel plate actuator based microgripper [57].

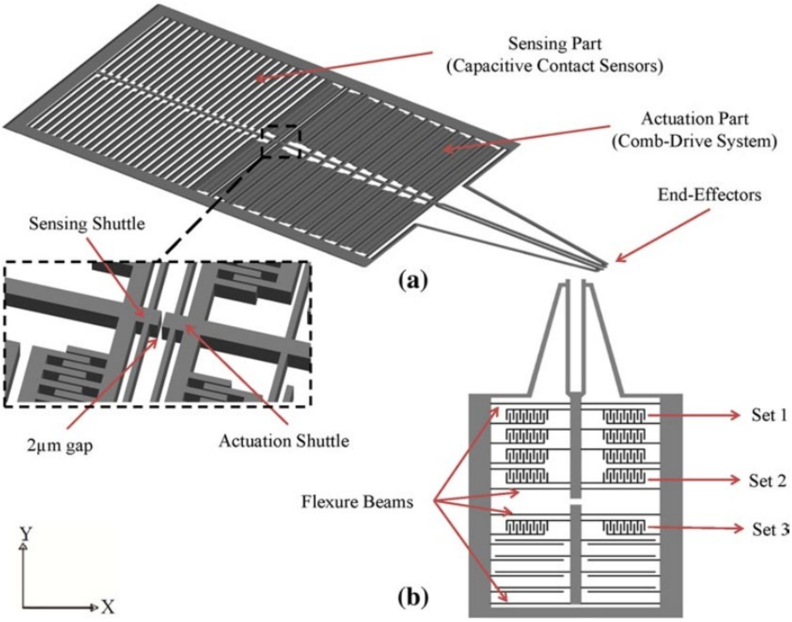

Figure 8. Schematic and detail view of the microgripper with linear comb drive actuator [58].

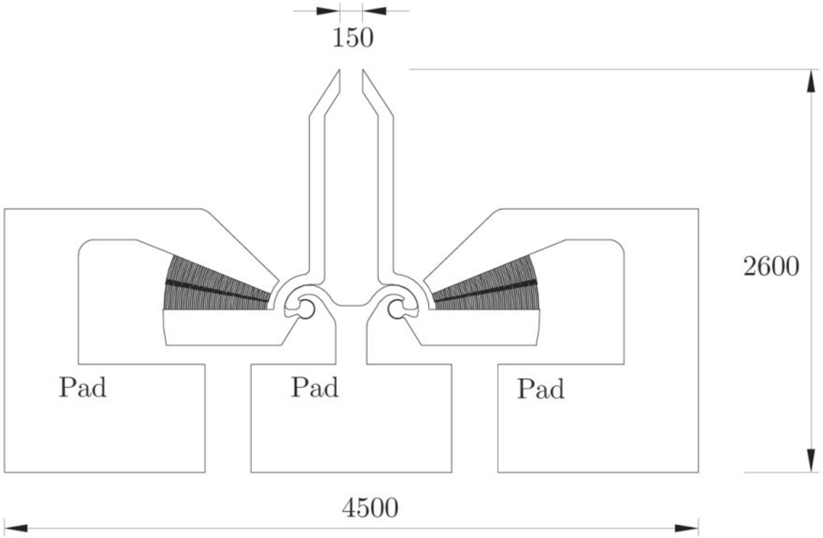

Figure 9. CSFH-based microgripper with rotary comb drive actuator [59].

2.2.2. Piezoelectric actuator

Piezoelectricity is a distinctive characteristic of specific materials such as quartz (SiO2), lead zirconate titanate (PZT), lithium niobate ($LiNbO_3$), and polymers such as polyvinyledene fluoride (PVDF). It enables the transformation of mechanical energy into electrical energy and vice versa. This phenomenon is based on the interdependence between mechanical strain and electric polarization within the material. Upon application of mechanical stress or strain to a piezoelectric material, it induces a displacement of positive and negative charges within the material, thus resulting in the generation of an electric charge across its surfaces. This is known as the direct piezoelectric effect.

On the other hand, when a piezoelectric material is subjected to an electric field, it induces a change in its size or shape, leading to mechanical deformation or displacement. This is referred to as the inverse piezoelectric effect.

Due to its advantages of fast response time, high sensitivity, large output force and precise positioning resolution, piezoelectric actuated microgripper is reported in [60]. Piezoelectric actuators are typically constrained by their ability to produce large displacements. In order to enhance the magnitude of these displacements, an amplification mechanism is incorporated into the structure. However, the implementation of such a complex system is ultimately affects the compactness of the overall structure.

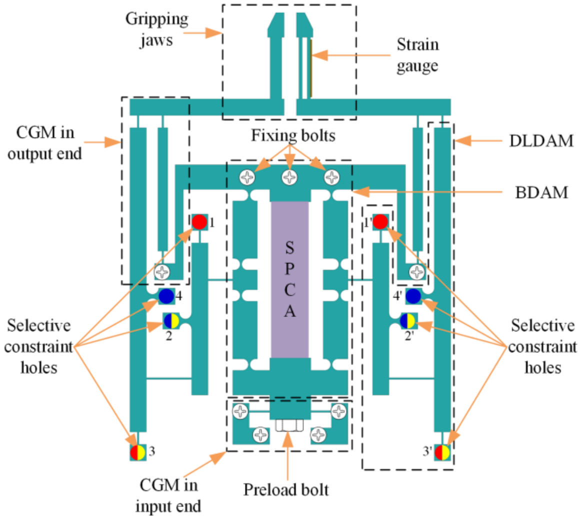

Figure 10. Multimode PZT microgripper [60].

2.2.3. Electrothermal actuator

An electrothermal actuator is one of the type of actuators that produces mechanical movement or deformation when an electrical current passes through it. This type of actuation is based on the principle of Joule heating, wherein electrical resistance in a material generates heat, leading to the expansion of the material and the subsequent generation of mechanical motion. There are two main types of electrothermal actuators, each employing different designs and principles to convert electrical energy into mechanical motion through the generation of heat. The first one is an asymmetric electrothermal actuator (bimorph) as depicted in Figure11 (a).

This actuator is constructed with a U-shape beam configuration in which one arm is thicker than the other one. The difference in the arm dimensions results in non-uniform heat generation through Joule heating, causing the temperature of the thinner arm to exceed that of the thicker one. This induces a difference in thermal expansion and consequently leads to a bending motion. The other type of electrothermal actuator is a symmetric thermal actuator (chevron) as shown in Figure 11 (b). This actuator comprises of a set of inclined beams that are connected to a central shuttle. The inclination angle facilitates the movement of the beam in the intended direction. Upon applying current to the beam structure, it induces thermal expansion in the beam and generates a displacement/force in the pre-bent direction.

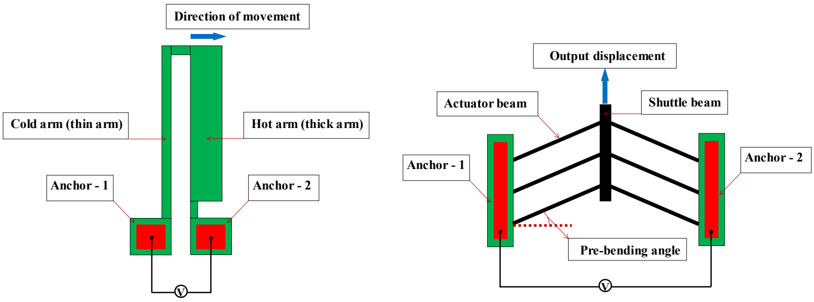

Figure 11. Schematic diagram of standard MEMS thermal actuators. (a) Biomorph type (asymmetric thermal actuator), and (b) Chevron type (symmetric thermal actuator).

Electrothermal actuators provide a large output force under a relatively low voltage but the induced high temperature during operation may restrict their applications in manipulating temperature sensitive materials as reported in [61], [62].

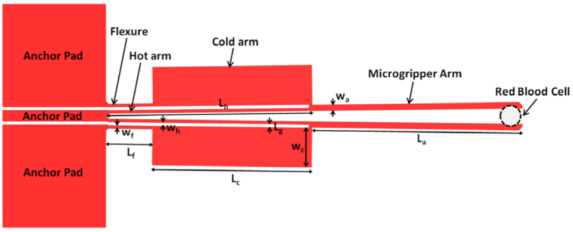

Figure 12. Schematic diagram of a microgripper with a bimorph type actuator [61].

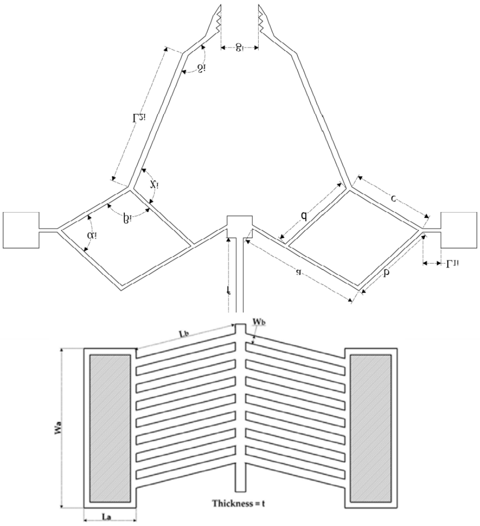

Figure 13. Schematic diagram of a microgripper with a chevron type actuator [62].

2.3. Sensing mechanisms in MEMS

Sensors have a crucial role in a variety of devices and systems by converting physical properties into measurable signals. They achieve a higher accuracy, repeatability, and lower power consumption compared to a conventional macro sensors. Micromanipulation tasks require force sensors, as they are essential for handling delicate samples. These sensors play a critical role in monitoring and controlling the forces exerted on the sample during the manipulation process to ensure that excessive or damaging forces are not applied. Several sensing methods have been developed and implemented for force measurement, each with its own set of advantages and limits. The three most common sensing technologies used in microsystems are piezoelectric, piezoresistive, and capacitive sensing [63], and the devices sensing performance is based on design parameters, fabrication constraints, and its application.

2.3.1. Piezoelectric sensor

Piezoelectric materials are known for their ability to generate an electric charge in response to mechanical stress or pressure applied to them.

When used in sensors, they can effectively measure changes in pressure, force, acceleration, and strain. The composition of a piezoelectric sensor typically involves three layers that form a wafer, with the piezoelectric material situated between two electrode plates. This configuration allows for the generation and collection of electric charges in response to external forces, leading to the production of an output voltage that corresponds to the applied stress or strain.

In the case of the MEMS piezoelectric sensor, the device is designed to detect physical deformations in structures. When the piezoelectric material is subjected to an external force or pressure in the longitudinal direction (parallel to polarization), charges are produced as a result. These charges work to restore the material to its original shape, and the electrodes play a crucial role in collecting the generated charges resulting from the in-plane stress or strains within the substrate. The accumulated charge is then converted into an output voltage that can be measured and analyzed.

One of the notable applications of piezoelectric sensors is as a force sensor in a microgripper, as reported in [39]. Piezoelectric force sensors exhibit excellent performance in dynamic mode, however, their capabilities are restricted when measuring static forces [64].

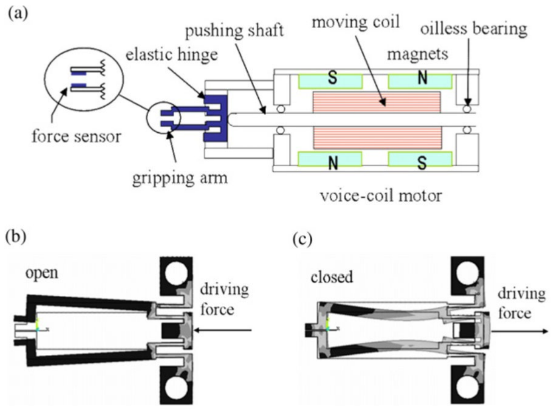

Figure 14. Configuration of microgripper with piezoelectric force sensor [39].

2.3.2. Piezoresistive sensor

The principle of the piezoresistive sensor is based on the piezoresistive effect, where the electrical resistance of certain materials changes when subjected to mechanical stress or deformation. This property is used to convert applied force or pressure into a measurable electrical signal. The most commonly used materials for piezoresistive sensors are silicon (Si), polysilicon (poly Si), silicon dioxide (SiO_2), and zinc oxide (ZnO).

To convert the physical deformation of the piezoresistive sensor into an output voltage, a Wheatstone bridge is often employed as the readout circuit. The Wheatstone bridge configuration helps to measure the change in resistance of the piezoresistive material, which is directly related to the applied force or pressure.

The piezoresistive sensors are specifically used as a force sensor in the microgripper mentioned in [65]. These sensors have a very simple fabrication process, however it has a low sensitivity and cannot detect small forces [66].

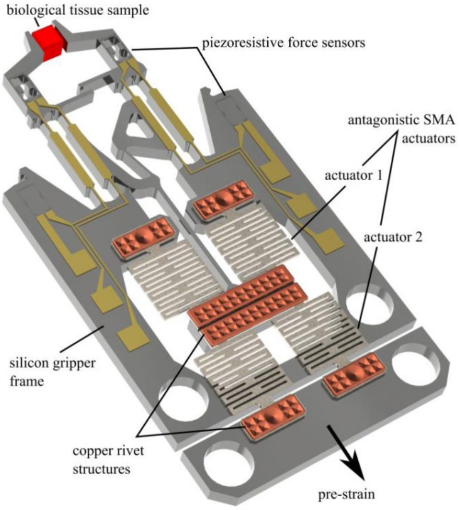

Figure 15. Model of the microgripper with piezoresistive force sensors [65].

2.3.3. Capacitive sensor

Capacitive sensors are commonly used in conjunction with microactuators to enable high-resolution sensing and precise control of micro and nano-sized motions. Capacitive sensors, as a non-contact sensing approach, work on the basis of measuring the capacitance change generated by the moving electrode shuttle between the stator and the movable electrodes. They have a number of advantages, including high sensitivity, low power consumption, and the ability to operate across a large dynamic range. Furthermore, they provide long-term durability and stability, making them ideal for applications needing long-term dependability. The use of the capacitive sensor is reported in [67].

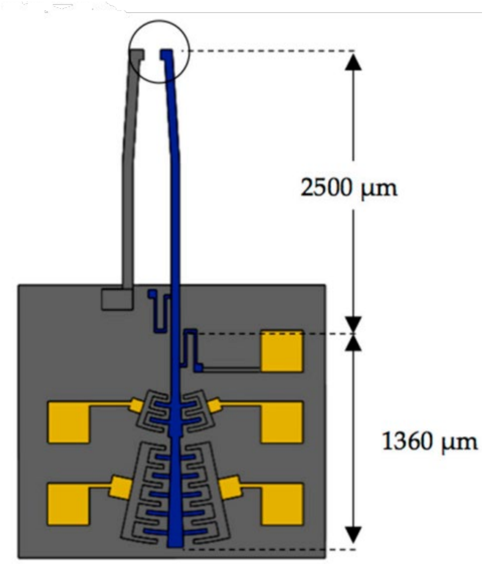

Figure 16. Schematic view of the MEMS microgripper design with a capacitive sensor [67].

2.4. Displacement amplification mechanisms

In many sensor systems, MEMS devices often have a limited function of converting the initial physical signal into a mechanical displacement or deformation. This mechanical change then results in a variation in capacitance or resistance. Typically, the resulting electrical changes are quite small and require amplification, which is commonly achieved using electronic amplifiers. However, the presence of noise and other sources of disturbance at the front-end of the electronic amplifier, such as parasitic capacitances, as well as the inherent noise sources of the amplifier itself, are amplified. Consequently, the sensitivity of such sensor systems is limited. Therefore, instead of amplifying the measurement signal in the electrical domain for the first time, an alternative data acquisition chain is used as reported in [68]. In this chain, a primary amplification is carried out in the mechanical domain using a compliant mechanical amplifier. This allows for the amplification of the measurement signal before any electrical noise disturbances can affect the analog signal.

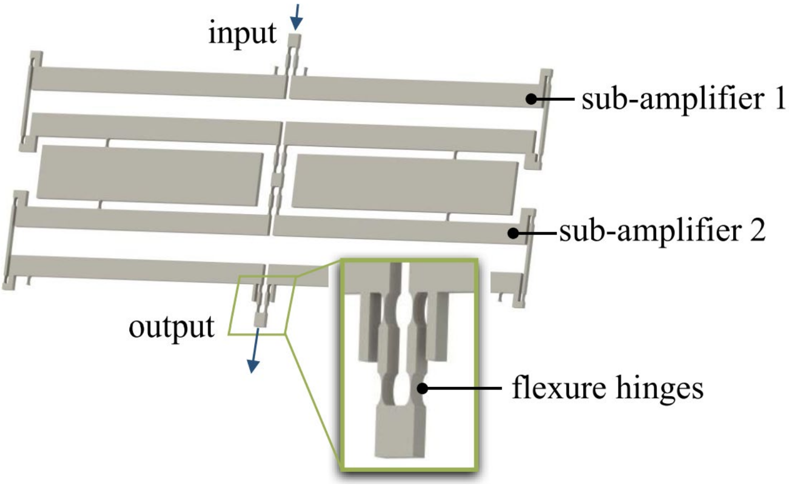

Figure 17. Schematic of the mechanical amplifier double configuration [68].

Amplifying displacement is a crucial aspect of MEMS technology, particularly in applications where there is a need for a large movement or change in capacitance. Various methods have been proposed to enhance the displacements in the actuators, sensors, and stress diagnosis structures [69], [70].

In particular, producing high displacement in micro-actuators has been challenging and highly important in the field of MEMS. The improvement of microactuator performance can be achieved by incorporating an intermediate mechanism that can amplify the displacement output. These miniaturized amplification mechanisms have the advantage of low power consumption, lightweight construction, and can be easily manufactured using standard MEMS fabrication techniques [69]. Flexure-based compliant mechanisms are increasingly showing potential in precision engineering, robotics, microgrippers, and other applications due to their exceptional benefits in addressing issues such as friction, backlash, and wear in conventional precision systems [26]. In general, flexure-based mechanisms can be divided into two types: planar mechanisms and 3D mechanisms [71]. However, planar flexure-based mechanisms are the most commonly used. These planar mechanisms have monolithically machined structures, which enable them to achieve precise motion control. They typically consist of single-axis flexure hinges [72], such as circular, corner-filleted, elliptical, and constant rectangular cross-section flexure hinges, which allow for two-dimensional motion. Various designs of flexure-based planar compliant mechanisms for motion amplification are reported in [73], [74].

Furthermore, a more recent development in the field is the conjugate surface flexure hinge (CSFH), which is discussed in section 2.1.1.2. This hinge can be constructed as a single unit and easily integrated into any MEMS mechanical structure. The CSFH provides several advantages, such as reducing internal stress, providing durability during operation, and optimizing overall relative hinge rotations. These hinges are used to create planar, compliant, and monolithic microgrippers that support rotational motion for manipulating cells and tissues [59], [75], [76].

MEMS-based rotational structures, like structures based on lancets [70], [77]–[79], are extensively used to measure stress, which is a crucial factor in optimizing residual stresses left by microfabrication processes.

One key advantage of rotational structures is their capability to measure both tensile and compressive stresses with a continuous readout. This feature is significant as it allows for the real-time characterization of stress distribution.

Currently, the MEMS-based fabrication technology employed in rotational structures allows them to occupy a limited area on the wafer, making them more suitable for high-density integration. Additionally, rotational structures possess the ability to directly amplify displacement, resulting in enhanced sensitivity. This makes them more suitable for stress measurements in small devices. However, despite their advantages, rotational structures do have some limitations. For example, they may not achieve significant displacement with a smaller input force and are more prone to breakage due to localized stress [70].

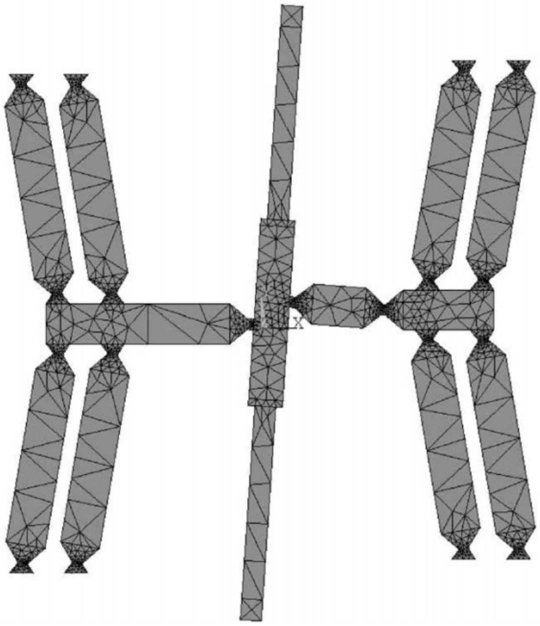

Figure 18. A symmetric lacet MEMS rotational structure [70].

2.5. Research motivation

The motivation behind this study originates from the identified limitations and challenges in existing CSFH-based micro-gripper designs that employ electrostatic actuation. The high actuation voltage and the absence of suitable packaging systems for microgrippers operating in liquid environments have hindered the development of efficient and reliable micromanipulation systems.

The primary goal of this study is to address these shortcomings by developing a novel electrothermally actuated CSFH-based microgripper. This innovative design aims to overcome the challenges posed by high actuation voltages while introducing a liquid-proof housing that enables the microgripper operation in immersed liquid environments. This functionality is crucial for manipulating delicate micron-sized biological samples in vitro.

To achieve high precision and repeatability in movement, to implement an accurate displacement sensor, and to validate the effectiveness of the proposed design of the micro-gripper, a combination of analytical modeling, finite element method (FEM)-based simulations and a series of experimental tests are conducted.

Furthermore, the study addresses the critical need for displacement amplification in MEMS rotational structures. By incorporating a C-shaped structure with a curved beam mechanism, the study aims to enhance displacement output in rotating structures. Optimization of geometrical parameters using the design of experiments (DOE) method, analytical modeling based on Castigliano’s second theorem, and FEM simulations have been employed to predict and understand the behavior of the proposed symmetrical C-shaped structure. The fabricated MEMS-based rotational structures on silicon-on-insulator (SOI) wafers underwent experimental characterization to validate the theoretical predictions.

Overall, this research strives to overcome the limitations of existing micro-gripper designs, advance the capabilities of MEMS-based micromanipulation systems, and contribute to the development of efficient tools for handling micron-sized objects, especially in liquid environments required for manipulating biological samples.

Electrothermally actuated MEMS Microgripper with integrated capacitive sensor: Design and FEM-based simulations

3.1. Design requirements

The presented microgripper is primarily composed of an actuation mechanism and a set of tweezers that are closely aligned. The core functionality of this microgripper lies in its ability to be controlled through the use of electrical power. This allows for the tweezers to open and close, facilitating a grasping motion.

Due to its designed application and foreseen experimental application, the initial requirements and restrictions to the design are:

(i) Need for tweezers thermally and electrically insulated from the actuation mechanism;
(ii) Target tweezer maximum acceptable temperature of 22 °C;
(iii) Target displacement range as large as 52.5 μm for each gripper arm (i.e., to provide more than 100 μm gripper offset since cells vary in size; therefore, a microgripper with wide gripping range is desired);
(iv) Minimum feature size of 6 μm; and minimum gap size of 2 μm due to MEMS fabrication technology constraints on a 25 μm thick SOI device layer.

3.2. Overall design of the microgripper

The development of the microgripper requires careful consideration of both the device concept and the capabilities of the fabrication technologies involved to achieve the desired functionality and performance within the constraints of miniaturization. The process of the microgripper development begins by defining the size of the biological sample required to be manipulated. In this study, the microgripper is specifically designed to manipulate chondrocytes, with the typical cell diameter ranging from 15–30 μm.

Following that, the key parameters such as the number of links, number of conjugate surface flexure hinges (CSFH), and lengths of the links are decided based on the application requirements. These parameters play a crucial role in determining the range of motion, precision, and ability of the gripping mechanism to accurately manipulate the target biological samples.

Subsequently, the focus of the design process shifts towards implementing actuation and thermal management mechanisms. The actuator, which is responsible for generating motion, is carefully designed to meet the necessary output displacement requirements at the tip of the tweezer for precise sample manipulation. Concurrently, a heat sink mechanism is developed to regulate the temperature around the microgripper, ensuring the integrity of the biological samples and optimal operating conditions.

Furthermore, the design process encompasses the development of a capacitive readout system. This system is designed based on the minimum sensitivity requirement of a capacitance measuring tool in our laboratory. It enables precise measurement and feedback regarding the position or displacement of the microgripper, contributing to enhanced control and manipulation accuracy.

Throughout the above stages, a combination of design iterations and Finite Element Method (FEM) simulations are used to refine the microgripper mechanism, ensuring that it meets the demanding requirements of its intended application.

The proposed microgripper is composed of a pair of gripping tweezers that are controlled by an electrothermal actuator, and it includes a built-in rotary capacitive position sensor as depicted in Figure 18. The electrothermal actuator is made up of v-shaped beams with varying widths. By applying a voltage to the anchors, a current flows through the beams, resulting in resistive heating and subsequently heating up the beams. This rise in temperature leads to thermal expansion of the beams, causing the central shuttle to move upward. To achieve the desired upward motion of the central shuttle, beams with a small angle are utilized [80]. These beams also have thin hinges at both ends to decrease their rigidity and enable a wider range of movement.

Furthermore, a displacement magnification mechanism is implemented using conjugate surface flexure hinges (CSFH) [51], [81] to create a compact design and enhance the actuator's movement.

In a CSFH mechanism, a series of bump-shaped structures are usually incorporated (Figure 19b). These structures function as a mechanical constraint and are employed to restrict the motion of the hinge's center of rotation while also holding the interdigitated capacitive readout fingers securely in position [82].

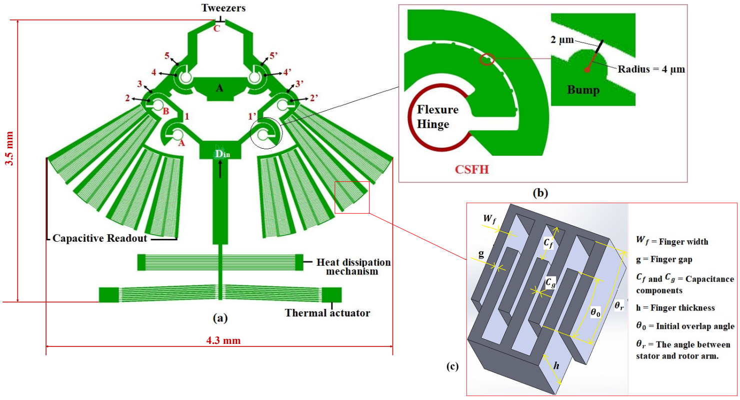

Figure 19. (a) Microgripper model with all its main components; (b) layout of a conjugate surface flexure hinge (CSFH) with a series of bump-shaped structures; (c) capacitive readout.

3.2.1. Working principle of the microgripper

The CSFH consists of a slender curved beam acting as a flexible component, along with a pair of conjugate surfaces (2 and 3, 4 and 5, 2' and 3', 4' and 5'). These flexure hinges facilitate the transmission and amplification of displacement. In order to achieve the desired opening of the tweezers, our device incorporates six CSFHs.

As Figure 19a illustrates, the thermal actuator delivers an actuation force that exerts an upward force on the links (1 and 1'). Consequently, the conjugate surfaces (2 and 2') rotate in a clockwise direction around the center of rotation formed by the revolute conjugate surfaces and the flexible hinges. Simultaneously, the opposite end of the flexure hinges generates a reaction force to counteract the rotation. This reaction force causes the bottom edges of the links (3 and 3') to move upward, resulting in the counter clockwise rotation of the conjugate surfaces (5 and 5') around the center of rotation formed by the revolute conjugate surfaces and the flexure hinges. Ultimately, this rotation generates a gripping force at the tip of the tweezers.

Table 1. Main parameters of microgripper and actuator structural elements.

Geometrical parameters	Values
Length of tweezers arms	290 µm
Width of curved beam	8 µm
Radius of curvature of the curved beam	60 µm
Number of beams	8
Pre-bending angle of beams	2°
Length of longest beam (with thin hinges)	1150 µm
Length of longest beam (without thin hinges)	1230 µm
Width of longest beam	15 µm
Length of shortest beam	40 µm
Width of shortest beam	6 µm
Gap between beams	8 µm
Shuttle width	40 µm

3.3. Finite Element Analysis of electrothermal actuator

The performance of the designed microgripper is evaluated using a finite element analysis (FEA) conducted in ANSYS^{TM} multiphysics. The present design incorporates an electrothermal actuator with thin hinges, as shown in Table 1. Besides the classical layout, a modified design with thin hinges [82] is simulated (Figure 20). The relationship between the delivered displacements and the applied voltage is shown in Figure 20, with the voltage ranging from 1V to 9V.

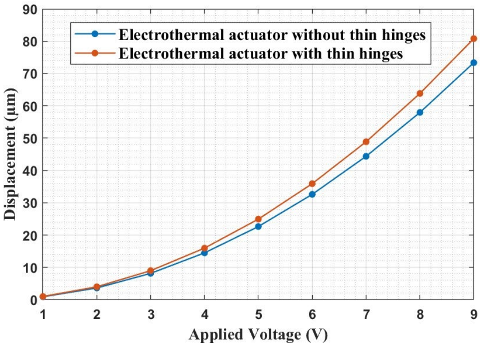

Figure 20. Displacement vs. Voltage for the electrothermal actuator with and without thin hinges.

As can be seen from the simulation, the thin hinges layout is preferable for this application due to the increased displacement it permits.

a) Thermal-Electric Analysis

This combined analysis enables the study of the effects of the applied voltage and the resulting joule heating on the microgripper. When a voltage difference is applied across the two ends of the actuator pad, joule heat is generated. This occurrence leads to an increase in temperature within the actuator and certain parts of the microgripper.

To simplify the simulation process, only one half of the microgripper is simulated, as both halves are identical. One half of the microgripper is anchored at three locations (Figure 21), which are considered to be an ambient temperature of 22 ºC. The silicon properties used in the simulations are reported in Table 2.

Table 2. Silicon properties used in the simulation of the microgripper [83].

Properties	Values
Density	2330 kg/m^3
Thermal expansion coefficient	2.5×10^{-6} °C^{-1}
Room temperature	22 ℃
Young’s modulus	130.1 GPa
Poisson’s ratio	0.22
Thermal conductivity	148 W/(m ℃)
Resistivity	0.005 Ω.cm
Melting point	1415 ℃

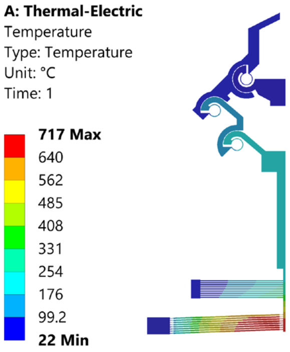

Figure 21. Temperature profile when the actuator is biased with 3.8 V.

From the temperature profile reported in Figure 21, the maximum temperature @ 3.8 V is around 717 ºC. This result is below the melting point of silicon, i.e. 1415 ºC, and with this temperature, the device will operate safely.

b) Static structural analysis

This analysis takes temperature as input data from the thermal-electric model to simulate the effects of the thermal expansion of the actuator and other parts of the microgripper. The three anchor regions are mechanically fixed here (Figure 22).

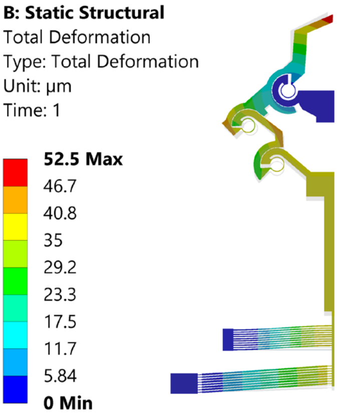

Figure 22. Total displacement when the actuator is biased with 3.8 V

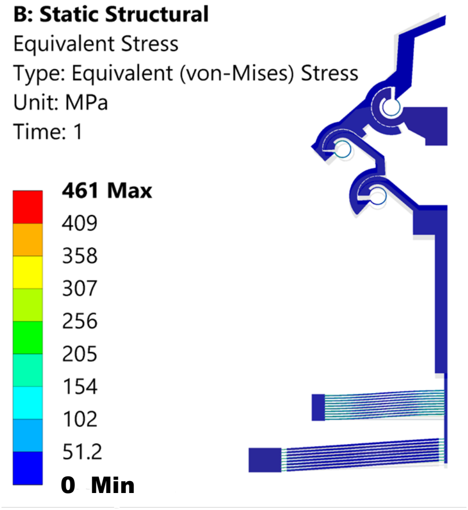

Figure 23. Stress field when the actuator is biased with 3.8 V.

From the displacement result (Figure 22), the tweezer tips move 52.5 µm one with respect to the other (i.e., 105 µm in total; such displacement corresponds to the initial target value). Stress is another crucial parameter to evaluate the performance of the microgripper. The result (Figure 23) shows that the maximum stress of 461 MPa is generated especially around the curved beam regions. Such stress level is significantly lower than the yield strength of silicon, i.e., 7 GPa [84], and thus has no significant impact on the life time of the microgripper.

3.4. Temperature profile analysis

Temperature analysis is crucial since high temperature can lead to the formation of bubbles or even damage biological samples. In this section, we examine the temperature field in the electrothermally actuated microgripper, specifically focusing on the gripper tweezers as they come into contact with the biological sample. Furthermore, we explain the importance of incorporating a heat sink with the microgripper, which effectively reduces the temperature at the gripper tweezers. Heat sink beams are placed in cascade with the actuator (Figure 19a) to facilitate temperature reduction towards the grippers (refer to Table 3 for the geometry). These beams dissipate heat through conduction to the substrate layer, which remains at room temperature.

Table 3. Geometry of the heat sink beams.

Geometrical parameters	Values
Length of heat sink beams	900 µm
Width of heat sink beams	10 µm
Distance between heat sink beams (Gap width)	10 µm
Number of heat sink beam pairs	10

a) Computational analysis of heat sink

As the microgripper is specifically designed for manipulating biological samples, it becomes crucial to consider the temperature profile. In order to compare the temperature profiles of the designed electrothermally actuated microgripper with and without heat sink beams, Ansys^{TM} multiphysics software is used for analysis. This analysis effectively demonstrates the benefits of incorporating a heat sink. The temperature at the anchor points is set to 22°C. To examine the device response, a potential of 0 V is applied to one end of the actuator pad while 3.8 V is applied to the other end.

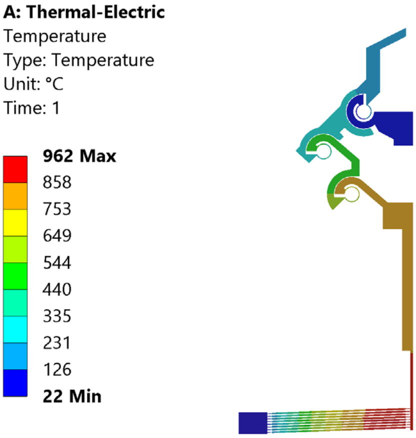

Figure 24. Temperature profile of microgripper without heat sink beams.

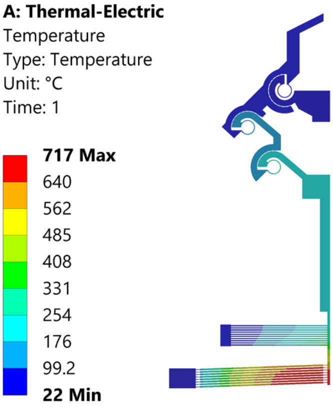

Figure 25. Temperature profile of microgripper with heat sink beams.

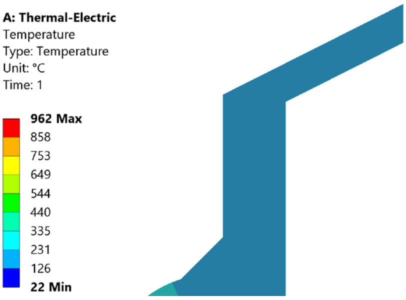

(a)

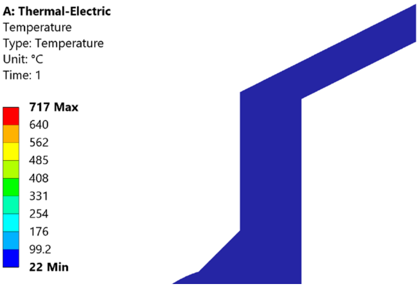

(b)

Figure 26. Temperature profile of the tweezers of the microgripper (a) without heat sink and (b) with heat sink.

The same input parameters were applied on the microgripper with and without a heat sink beams, and a finite element analysis was conducted. The corresponding results are pictorially presented in Figure 24 and 25. In both cases, the center of the shuttle exhibited high temperatures, while the gripper tweezers experienced temperature reduction due to dissipation. When heat sink beams were used, the temperature was further dissipated through the beams, resulting in additional reduction at the gripper tweezers. At 3.8 V, the temperature in the gripper tweezers was approximately 22 °C, which is considered a safe temperature for manipulating biological samples. This is significantly lower than the temperature experienced by the gripper without a heat sink (126 °C), as shown in Figure 26. Furthermore, this result was observed across a range of input voltages from 0.5 to 4 V, as shown in Figure 27. The plot clearly demonstrates that the gripper tweezers experience greater temperature reduction when a heat sink is used.

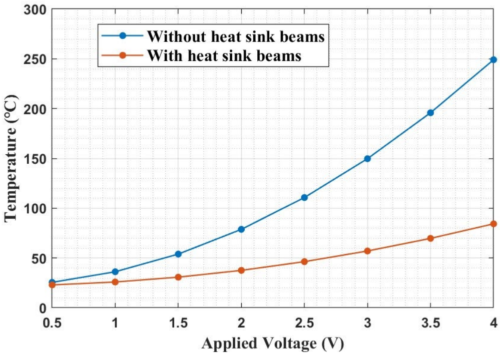

Figure 27. Temperature vs. Applied voltage with and without heat sink beams.

3.5. Displacement sensor

The sensor, which is a rotary type with CSFH, generates rotational motion. It is connected to the inclined linkages of the microgripper, as depicted in Figure 19 (with geometry details provided in Table 4). This sensor comprises variable capacitors, each of which has a fixed and a movable comb electrode.

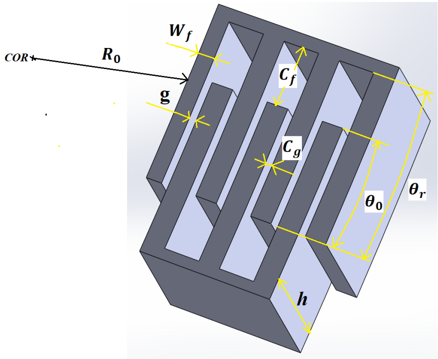

Figure 28. Solid model of the rotary comb finger electrodes.

As depicted in Figure 28, the capacitance caused by each movable comb finger comprises primarily of two components, namely C_g and C_f. The contribution of C_g arises from the gaps between the fingers, while C_f arises stems from the spaces between the fingertip surface and the side surface of the fixed arm. In typical scenarios, C_f is insignificant and can be disregarded. Consequently, the overall capacitance (C_{tot}) can be expressed as [85]:

$$C_{tot} = \varepsilon_0 \theta h \left\{ \sum_{i=1}^{n-1} \left[ln \frac{R_0 + 2i(W_f + g)}{R_0 + 2i(W_f + g) - g} \right]^{-1} + \sum_{i=0}^{n-1} \left[ln \frac{R_0 + (2i+1)(W_f + g)}{R_0 + 2i(W_f + g) + W_f} \right]^{-1} \right\} \tag{1}$$

Then, the total sensitivity (S_{total}) is calculated by the following formula:

$$S_{total} = \frac{C_{tot}}{x} \tag{2}$$

Where ε_0 is permittivity with a value of 8.854 x 10^{-12} F/m, θ is the final overlap angle, h is the finger thickness, R_0 is the inner radius of the first finger close to the central hinge, n is the number of movable fingers, W_f is the finger width of the comb fingers and x is the displacement of tweezers. By applying Equations (1) and (2), the total sensitivity of the capacitive position sensors is 102 $fF/\mu m$.

Table 4. Dimensions of the rotary capacitive sensor.

Geometrical parameters	Values
Thickness of device layer, t	25 μm
Number of movable fingers of each set, n	70
Finger width, W_f	6 μm
Finger gap, g	2 μm
Initial overlap angle, θ_0	1°
The angle between the stator arm and rotor arm, θ_r	9°
The inner radius of the first finger close to the central hinge, R_0	670 μm

Performance analysis of the CSFH-based microgripper: Analytical modeling and FEM-based simulations

4.1. Modeling of the microgripper

4.1.1. Kinematic modeling

According to a pseudo-rigid-body-method equivalent mechanism [86], the flexure hinges H_1–H_6 are equivalent to rotational springs, while the connecting links are rigid members (Figure 29(a)-(c)). The actuator provides the input displacement to the whole microgripper, which is D_{in}, which is provided by the actuator; D_{out} is the output displacement of the microgripper's grasping tweezers.

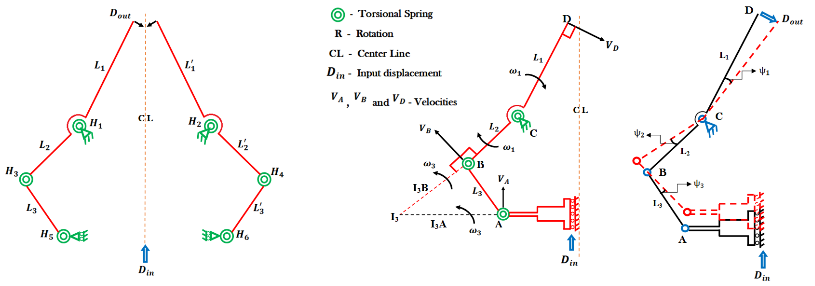

(a) (b) (c)

Figure 29. (a) Pseudo-rigid-body equivalent model of the microgripper; (b) velocity vector diagram of the microgripper; (c) angular changes of the microgripper.

Because of the symmetrical configuration of the microgripper, the kinematic analysis is performed on half of it, and the velocity vector diagram is shown in Figure 29(b). The instantaneous centers of the corresponding links can be determined using the velocity vector diagram.

The velocities at points A, B, and D can be calculated as follows (Figure 29(b)):

$$V_A = \omega_3 \times I_3 A \tag{3}$$

$$V_B = \omega_3 \times I_3B \tag{4}$$

$$\omega_3 = V_A/I_3A = V_B/I_3B \tag{5}$$

where ω_3 is the angular velocity of link 3, I_3A and I_3B are the relative positions from points A and B to the instantaneous center I_3, respectively.

By considering Figure 29, the following relationship between the velocity at point B and D can be derived as:

$$V_B = \omega_1 \times L_2 \tag{6}$$

$$V_D = \omega_1 \times L_1 \tag{7}$$

$$\omega_1 = V_B/L_2 = V_D/L_1 \tag{8}$$

where ω_1 is the angular velocity of links 1 and 2, L_1 and L_2 are the lengths of the corresponding links.
By considering Equations (5) and (8), we achieve:

$$V_A/V_B = I_3A/I_3B \tag{9}$$

$$V_B/V_D = L_2/L_1 \tag{10}$$

Combining Equations (9) and (10) and calculating V_D/V_A, which represents V_{out}/V_{in},

$$V_D/V_A = L_1/L_2 \times I_3B/I_3A \tag{11}$$

Therefore, the amplification ratio [87] can be computed as,

$$R = D_{out}/D_{in} \approx V_{out}/V_{in} \tag{12}$$

Furthermore, considering that during the kinematic modeling, only half of the microgripper is considered since the microgripper has a symmetrical configuration, the amplification ratio of the overall microgripper structure can be computed as,

$$R_{tot} = 2 \times V_D/V_A = 2 \times (L_1/L_2)/(I_3A/I_3B) \tag{13}$$

According to Expression (13), the amplification ratio is only related to the geometrical parameters of the microgripper. In the following section, we investigate further the static modeling of the microgripper to describe the force-deflection relationship of the flexure hinges.

4.1.2. Input stiffness of the microgripper

The input stiffness of the mechanism is an important parameter that qualifies the performance of a compliant mechanism [88]. In order to determine the relationship between force and displacement of the microgripper, input stiffness analysis is performed.

Input stiffness is defined as the ratio of input force at the shuttle of the microgripper (F_{in}) to axial displacement (D_{in}). There is formation of torque at the flexure hinges as a result of the effect of the input force, and the torque M_i generated at the rotational center of the flexure hinges can be calculated as [89]:

$$M_i = -K_i \Phi_i \quad i = A, B \ and \ C \tag{14}$$

where K_i represents the stiffness of the i-th flexure hinges and Φ_i represents its rotation angle. The negative sign indicates that the moment rotates in the opposite direction as the flexure hinge. When inhomogeneity and anisotropy in silicon microstructures and the corresponding stiffness matrix are ignored, and linear elastic beams with uniform, rectangular cross-sections are considered, and the bending moment is assumed to be constant, the stiffness of the flexure hinges (K_i) can be calculated as [81]:

$$K_i = \frac{EI}{\theta'_i r} = \frac{Etw^3}{12\theta'_i r} \quad i = A, B \ and \ C \tag{15}$$

where E is the Young’s modulus, r is the flexure hinge radius, θ' is the initial angle of the flexure hinges, and I is the moment of inertia of the cross-section, with $I = \frac{tw^3}{12}$ [50], t and w as the thickness and width, respectively.

To derive the input stiffness of the microgripper, the Castigliano's theorem is adopted [86], [87], [90], [91]. By considering the PRBM of the microgripper with input forces on the shuttle of the microgripper (F_{in}), output forces at the tip of the tweezer (F_{out}), and torques at each joint, the total virtual work of the system, δW_{sys}, can be written as:

$$\delta W_{sys} = \vec{F}_{in} \cdot \delta \vec{D}_{in} + \vec{F}_{out} \cdot \delta \vec{D}_{out} + \sum_{i=A}^{C} \vec{M}_i \cdot \delta \vec{\Phi}_i \quad , \quad i = A, B \text{ and } C \tag{16}$$

Based on the principle of virtual work, $\delta W_{sys} = 0$ and, since $\vec{M}_i = -K_i \cdot \delta \vec{\Phi}_i$; therefore, Equation (16) can be obtained as:

$$F_{in}\, D_{in} - F_{out}\, D_{out} - \sum_{i=A}^{C} K_i \Phi_i^2 = 0 \tag{17}$$

Recalling Expression (13), after substitution and re-arrangement of parameters, Equation (17) can be obtained as:

$$F_{in} = R_{tot} F_{out} + \frac{2U}{D_{in}} \tag{18}$$

where,

$$U = \frac{1}{2} \sum_{i=A}^{C} K_i \Phi_i^2 \tag{19}$$

The grasping procedure for micromanipulation of micro-objects includes closing both tweezers to approach and grasp the object, and firmly holding the object. Before the tweezers make contact with the object, the output force F_{out} is zero, and Equation (18) can be calculated as follows:

$$F_{in} = \frac{2U}{D_{in}} \tag{20}$$

where U is the deformation energy, F_{in} and D_{in} are the input force and the input displacement, respectively.

For a small input displacement D_{in}, the rotational angles Φ_A, Φ_B, and Φ_C of the flexure hinges *A*–*C* can be obtained as (Figure 29(c)):

$$\Phi_A = \psi_3 = \frac{D_{in}}{I_3 A} \tag{21}$$

$$\begin{aligned}\Phi_B &= \psi_3 + \psi_2 = \psi_3 + \psi_3\left(\frac{I_3 B}{L_2}\right) = \psi_3\left(1 + \frac{I_3 B}{L_2}\right)\\ &= D_{in}\left(\frac{1}{I_3 A} + \frac{I_3 B}{I_3 A L_2}\right)\end{aligned} \tag{22}$$

$$\Phi_C = \psi_1 = \frac{D_{in} R}{L_1} = \psi_2 \tag{23}$$

where ψ_1, ψ_2, and ψ_3 are the angular changes of the links *CD*, *BC*, and *AB*, respectively.

Substituting Equations (23)–(25) into (21) yields:

$$U = \frac{1}{2}\left(\frac{K_A D_{in}^2}{I_3 A^2}\right) + \frac{1}{2}\left(K_B\left(D_{in}\left(\frac{1}{I_3 A} + \frac{I_3 B}{I_3 A L_2}\right)\right)^2\right) + \frac{1}{2}\left(K_C\left(\frac{D_{in} R}{L_1}\right)^2\right) \tag{24}$$

Substitute Equation (24) into (20), and the input force can be obtained as:

$$\begin{aligned}F_{in} = \Bigg(&\frac{K_A}{I_3 A^2} + K_B\left(\frac{1}{I_3 A^2} + \frac{2 I_3 B}{I_3 A^2 L_2} + \frac{I_3 B^2}{I_3 A^2 {L_2}^2}\right)\\ &+ K_C\left(\frac{R^2}{L_1^2}\right)\Bigg) D_{in}\end{aligned} \tag{25}$$

The input stiffness of the microgripper can be derived as:

$$K_{in} = \frac{F_{in}}{D_{in}} = \left(\frac{K_A}{I_3 A^2} + K_B\left(\frac{1}{I_3 A^2} + \frac{2 I_3 B}{I_3 A^2 L_2} + \frac{I_3 B^2}{I3 A^2 {L_2}^2}\right) + K_C\left(\frac{R^2}{L_1^2}\right)\right) \tag{26}$$

4.2. Analytical modeling of V-shaped thermal actuator and heat sink beams

The actuator is constructed from v-shaped stepped beams and heat sink beams, whose behavior will be studied in the following subsections. According to the literature [92], the mechanical behavior of the electrothermal actuator can be analytically derived by considering the following assumptions: (i) The average temperature increase in the inclined beams of the electrothermal actuator is known; (ii) the central shuttle is rigid and not affected by the temperature increase; (iii) small strains and displacements are considered; and (iv) the shear deformation of the beams is negligible.

The thermal actuator in our microgripper design consists of pairs of stepped beams connected to the substrate and a central shuttle, and it is used to drive the microgripper. Each beam has a thinner section at both ends and a thicker section in the middle. Thinner parts are important for reducing stiffness and enabling a wider range of motion, as illustrated below. Despite the fact that it is widely adopted [93], [94], there is no exhaustive analytical model for this stepped beam thermomechanical actuator available in the literature.

Therefore, we report for the first time a complete analytical model of this actuator. In the proposed model, the small deformation hypothesis is adopted for both lateral bending and axial deformation of the beams.

Let us consider a single inclined beam; this can be modeled by three elements (e_1, e_2, e_3), with length L_1, L_2, and L_3, respectively, and four nodes in total (Figure 30c).

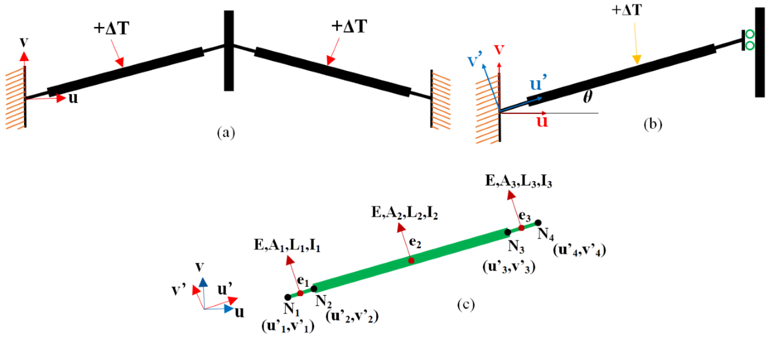

Figure 30. (a) Schematic of a pair of stepped inclined beams subjected to an average increase in temperature (ΔT). Each beam has a thicker and longer element in the center, and two thinner and shorter beams at the ends; (b) equivalent mechanical representation of a single beam in a local reference frame; (c) single inclined beam of the thermal actuator modeled by four nodes and three elements. Elements 1 and 3 correspond to the short beams that connect the central beam (element 2) to the anchor (left end) and shuttle (right end), respectively.

The displacement at node 4 in the v-direction, $v^{\Delta T}$, due to an average temperature increase in ΔT along the beam, can be derived analytically (see Equation (21) in the Appendix) according to the following procedure: (i) Discretize the inclined beam structure into its elements. Additionally, both lateral bending and axial deformation of the beams are considered. These considerations show that the beam element is treated as a frame element; (ii) compute the elastic stiffness matrix in a local reference frame (u', v'); (iii) transform the local stiffness matrix to global stiffness matrix by means of a rotation matrix; (iv) assemble the element matrices; and (v) impose the boundary conditions in the global matrix to find the displacements at each node (see Appendix A for details).

Displacement $v^{\Delta T}$ is dependent on geometrical quantities, such as the elements lengths, cross-sectional area, moment of inertia, the beam angle, the coefficient of thermal expansion of the beam material, and the Young's modulus of the material.

The response of two inclined beams subject to an external force (F) applied to the central shuttle along the v-direction, can be obtained similarly. In particular, the analytical expression for the displacement at node 4, v^F, due to an external force (see Equation (22) in the Appendix) can be obtained starting from a similar governing system of equations (14 reported in the Appendix), where the thermal load on the right side (i.e., $\alpha \Delta T E A$ is the thermal expansion force of the beams [95] is substituted with external force ($F/2$).

Then, ratio $K_A = F/v^F$ represents the stiffness of one v-shaped thermal actuator beam; in which the quantity multiplied by the number, m, of v-shaped beams provides the overall stiffness of the thermal actuator (see Equation (23) in the Appendix).

In the case that the v-shaped thermal actuator beam is subjected to both a temperature increase (ΔT) and an external force (F), the displacement can be obtained as:

$$v_4^{\Delta T+F} = v_4^{\Delta T} + v_4^{F} \tag{27}$$

To check the effectiveness of our model, we considered a thermal actuator beam with uniform cross-section. In this case (Figure 31(a)), we compared the results in terms of delivered displacement at varying temperature increase, obtained from our model with the ones that can be derived from the following literature model [92]:

$$U^{\Delta T} = U_y^{A} = \alpha \Delta T l \frac{\sin\theta}{\left(\sin^2\theta + \cos^2\theta\left(\frac{12I}{Al^2}\right)\right)} \tag{28}$$

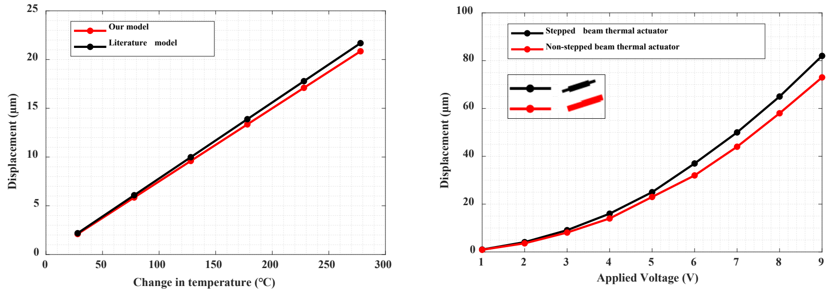

(a) (b)

Figure 31. (a) Displacement vs. temperature change in one inclined thermal actuator beam with uniform cross-section modeled through a literature model [36] and our model at a tilt angle of 2°; (b) comparison between non-stepped beam thermal actuator and stepped beam thermal actuator in terms of displacement when the actuator is biased with 1–9 V.

In Figure 31(a), the displacements delivered by the actuator beam obtained from both approaches have a good match with a maximum difference of ~4% at 278 °C. This result shows that our model can be effectively used for the analysis of non-stepped beam actuators, as well.

Then, we compared the performance of a stepped actuator beam with respect to a non-stepped one.

Figure 31(b) shows the displacement along the v-direction at the central shuttle as a function of the applied voltage for a non-stepped actuator and a stepped actuator with a ratio between the lengths of the external and the central region equal to $40/1150$. The plot shows that the stepped beam thermal actuator performs better than the classical non-stepped beam thermal actuator in terms of displacement delivery, with the produced displacement to be enhanced by up to 1.12× at 9 V; this also indicates that the stepped beam thermal actuator is less stiff than the classical one.

To achieve the intended application of the microgripper, we need to meet some design goals:

1. Input displacement of ~39 μm to achieve the desired output displacement of each tweezer (52.5 μm).
2. Ambient temperature (22 °C) at the tweezer region.

From Equations (21) and (23) in the Appendix, it is seen that the displacement and stiffness of the thermal actuator when unconstrained by heat sink beams depends on the beam lengths ($L_1, L_2,$ and L_3), the beam angle (θ), change in temperature (ΔT), and the cross-sectional area of the beams ($A_1, A_2,$ and A_3).

Figure 32(a) shows the stepped and non-stepped beam thermal actuator displacement provided by Equation (21) in the Appendix as a function of the stepped and non-stepped beam inclination angle. It is seen that the displacement increases with small angles in the range of $\theta \leq 2°$.

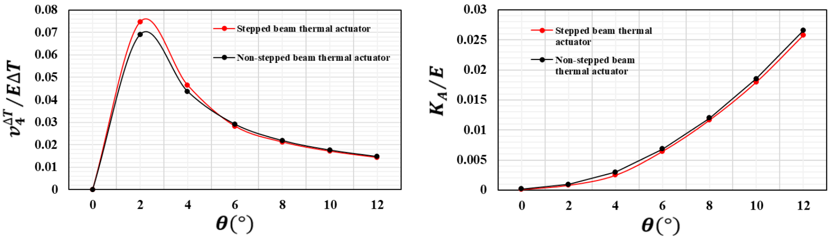

(a) (b)

Figure 32. (a) Displacement as a function of the inclined beam angle; (b) stiffness as a function of the inclined beam angle.

Figure 32(b) shows the stepped and non-stepped beam thermal actuator stiffness provided by Equation (23) in the Appendix as a function of the stepped and non-stepped beam inclination angle. The plot shows that the actuator stiffness increases with the beam angle. In light of these results, our microgripper was designed with v-shaped beams inclined by 2°, thus with high displacement capability and reduced stiffness.

Then, to manage the temperature increase produced by the thermal actuator, we can consider the presence of heat sink beams located between the thermal actuator and the tweezers (Figure 18). As we see from Figure 33 (half section of heat dissipation and thermal actuator model), at the left side of the heat sink beams, there is a clamp (since the beam is anchored to the substrate), while at the right side, the shuttle acts as a slider.

Heat sink beams are subject to transverse loading that produces significant bending effects.

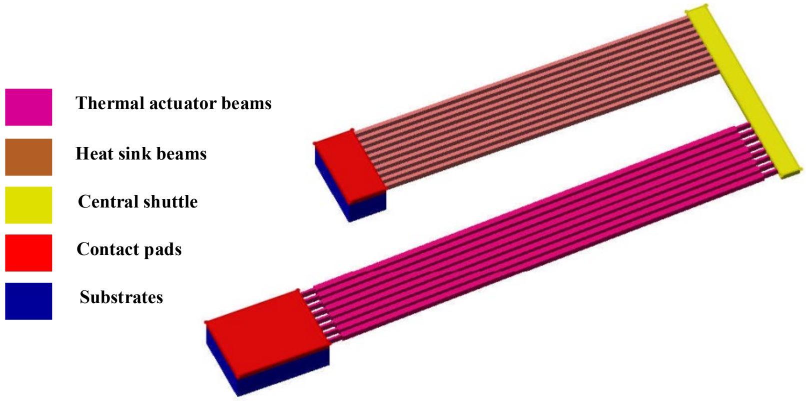

Figure 33. Connection of heat sink beams to the substrate and the actuator shuttle.

The displacement of the single heat sink beam due to the external force (P) at the central shuttle can be expressed as:

$$v^P = \frac{PL^3}{12EI} \tag{29}$$

Considering the heat dissipation mechanism consisting of n number of heat sink beams, the total stiffness will be:

$$K_{HS} = n\frac{12EI_{HS}}{{L_{HS}}^3} \tag{30}$$

To achieve the intended motion of the links of the microgripper, and to operate the microgripper safely, stiffness analysis of the overall structure is crucial. Therefore, stiffness analysis of the main structures (microgripper, heat dissipation mechanism, and thermal actuator) is performed.

Using Equations (24), (28), and Equation (23) in the Appendix, and the parameters reported in Tables 1 and 2 (silicon properties and geometrical parameters), the stiffness of microgripper, thermal actuator, and heat dissipation mechanism are 14, 1728, and 89 $\mu\mathrm{N}/\mu\mathrm{m}$, respectively.

Based on the above results, the stiffness of the electrothermal actuator is considerably larger than the stiffness of the microgripper and the stiffness of the heat sink beams; therefore, the actuator can drive the microgripper properly.

4.3. Comparison between the Performances of the Microgripper, the Electrothermal Actuator, and the Heat Dissipation Mechanism Obtained from the Analytical Modeling and Simulations

To verify the validity of the theoretical modeling approach discussed in the previous sections, FEA is performed in ANSYS$^{\mathrm{TM}}$ multiphysics (2021 R1, American company based in Canonsburg, USA). Three-dimensional structural and coupled electric-thermal-mechanical simulations are conducted.

The microgripper material is silicon, as in typical MEMS devices, and its main properties, used as input for the FE analysis are listed in Table 2.

4.3.1. Microgripper’s Deformation and Stress

The length of the links and all the other parameters defining the microgripper geometry were identified upon an optimization process, which was carried out to grant a compact microgripper design (i.e., footprint of 4.3 × 3.5 mm^2) that is compliant with the microfabrication constraints (i.e., minimum feature size) and operational requirements (i.e., tweezer offset and temperature), as reported in the Introduction. This optimization process resulted in the following values: I_3B = 523.9 µm, I_3A = 614.2 µm, L_1 = 775.2 µm, and L_2 = 487.6 µm. If we consider Equation (13), the overall amplification ratio (R_{tot}) can be 2.71.

Regarding the FEA, we performed a static structural analysis, where we applied a displacement of ~39 µm at the input end (i.e., at the shuttle of the microgripper). This indeed allowed the achievement of an output displacement of 52.5 µm at each tweezer's arm (i.e., a total of 105 µm output displacement). Ideally, this displacement is intended for cell manipulation, where a typical cell diameter can be in the order of 15–20 µm [96], by considering an offset between the tweezer's arms of 120 µm at rest to enable safe positioning in the vicinity of a cell.

The total displacement and stress field results obtained from the numerical simulations are shown in Figure 34(a) and (b).

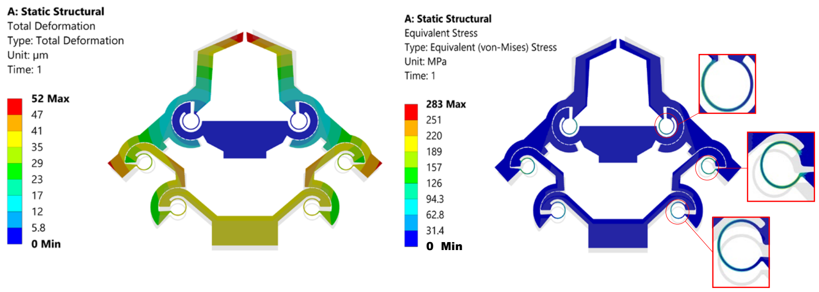

(a) (b)

Figure 34. (a) Total displacement; (b) stress field when 39.16 µm input displacement is applied at the shuttle of the gripper.

The output displacement of each tweezer resulted in a value of 52.5 µm (Figure 34(a)), i.e., the total output displacement of the tweezers was 105 µm, with a corresponding displacement amplification ratio of 2.68 (i.e., 105/39.16 µm).

As shown in Figure 34(b), the maximum stress of the microgripper was ~283 MPa, which is considerably less than the yield strength of the material (7 GPa); therefore, the device can be used safely.

By comparing the amplification ratio value obtained from the analytical modeling and simulations, there is a good match, with a relative difference of only ~1%, thus demonstrating the effectiveness of the PRBM approach in modeling the kinematics of the structure under investigation. The small difference between the analytical and numerical estimation can be due to different reasons, such as (i) the linkages are considered as rigid links in the theoretical model, but deformation occurred on the linkages in FEA simulation, and (ii) the rotation center of the flexure hinges drifted in FEA simulation, while in the theoretical modeling this cannot happen.

Figure 35 reports a plot showing the overall performance of the designed microgripper. In particular, it is possible to observe that the temperature in the gripper tweezer region is constant with 10 heat dissipation bars (which is around 22 °C) in a voltage range from 1 to 3.8 V, which is a safe temperature for biological sample manipulation. The range of the applied voltage is decided based on the desired output tweezer displacement, i.e., 52.5 μm. Moreover, the tweezer (jaw) and the overall gripper regions are considered for the analysis.

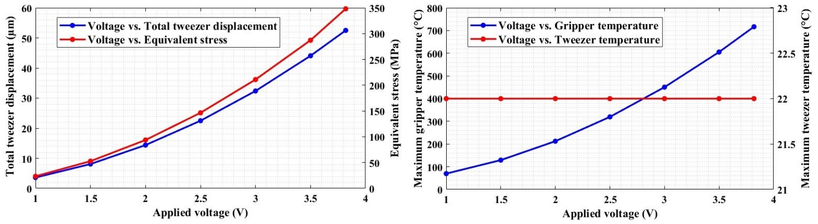

(a) (b)

Figure 35. (a) Tweezer displacement and equivalent stress as functions of the applied voltage; (b) microgripper and tweezer temperature as functions of the applied voltage

4.3.2. Microgripper Stiffness

Using Equation (26), the theoretical input stiffness of half of the microgripper is calculated as ~7 μN/μm, and regarding the FEA, we performed a static structural analysis, where we applied an input force (267.3 μN) at the input end (i.e., at the shuttle of the microgripper) (Figure 36(a)).

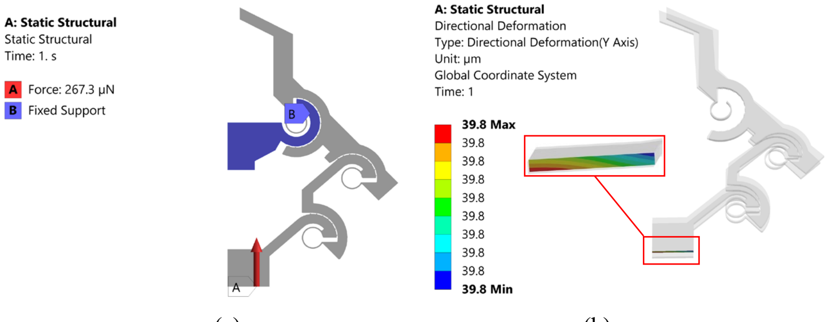

(a) (b)

Figure 36. (a) Boundary conditions of the static structural analysis; (b) directional displacement along the vertical direction at the shuttle of the microgripper when a full range input displacement is applied.

By considering an input force at the shuttle of the microgripper, the input stiffness of the half microgripper is (267.3/39.8) = 6.7 μN/μm. Therefore, the input stiffness's obtained from analytical modeling and FEA have a good match with a relative difference of ~4.5%.

4.3.3. Electrothermal Actuator

To verify Equation (21) in the Appendix, we performed a coupled steady-state thermal–static structural analysis, and we considered the same assumptions as the theoretical modeling, i.e., the central shuttle is rigid and not affected by the temperature increase. Geometrical parameters implemented in the numerical analysis are reported in Table 1.

The displacements at node 4 obtained from analytical modeling and simulation have a good match with a relative difference of ~2.8% in temperature (ΔT) range from room temperature to 278 °C (Figure 37).

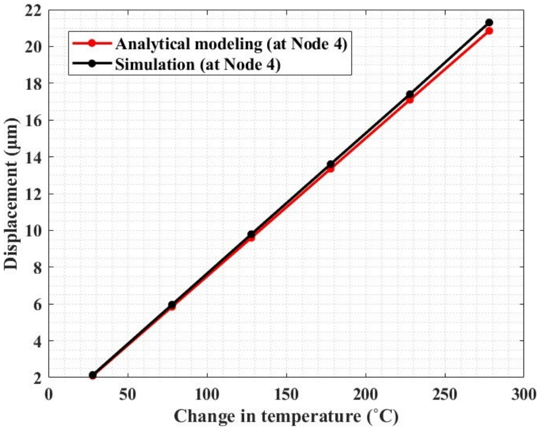

Figure 37. Comparison of the results, in terms of displacement vs. temperature change, obtained from analytical modeling and finite element simulations of the electrothermal actuator.

4.3.4. Thermomechanical Actuation and Heat Dissipation Mechanism

Multi-physics analysis is also performed to provide an assessment of the temperature across the microgripper. The simulation is carried out by considering the full range input displacement of the gripper (~39 µm) to achieve the desired total output displacement of 105 µm. Moreover, we selected a beam angle of 2° by considering Figure 32(a).

Figure 38(b) shows that we could achieve the intended 39 µm input displacement of the gripper with the proposed electrothermal model. However, the temperature at the tip of the actuator shuttle (Figure 38(a)) is significantly high.

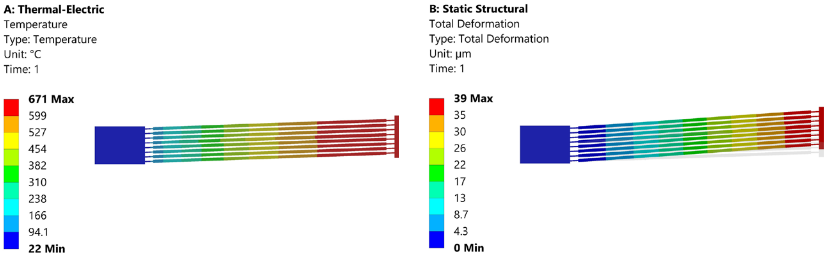

(a) (b)

Figure 38. (a) Temperature field; (b) displacement field when the thermal actuator is biased with 6.2 V.

To examine the effectiveness of heat sink beams in controlling the temperature increase around the tweezer region, the number of pairs of the heat sink beams is considered.

Based on our intended input displacement and minimum temperature requirement around the tweezer region of the gripper, eight and ten numbers of heat sink beams can both be effective (Figure 39). However, we observed that there was an increment of temperature around the capacitive readout region with eight heat sink beams.

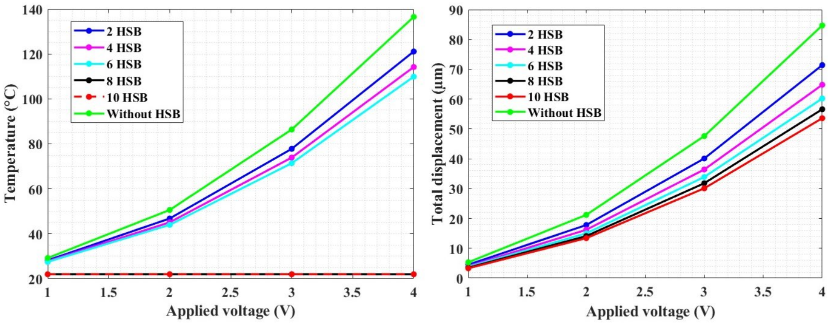

(a) (b)

Figure 39. (a) Temperature at the tweezer region; (b) displacement at the tip of the tweezer for various numbers of heat sink beams (HSB) when the actuator is biased with 1–4 V.

Indeed, for the safety of the microgripper structure, and to provide position feedback, rotary type capacitive sensors were implemented on the links of our microgripper. Therefore, changes in humidity or temperature can interfere with the operation of the sensors, and, in some cases, it can stop the sensor from working altogether [97].

By considering the drawbacks of temperature increase on the sensor, the electrothermal actuator with 10 pairs of heat sink beams is selected for our proposed microgripper structure.

Displacement amplification mechanism

5.1. A C-shaped hinge for displacement magnification in MEMS rotational structures

In this study, we investigated two distinct rotational structures based on MEMS technology. Both of these structures were designed using the same guidelines, specifically the same footprint and critical dimensions. The first structure, known as the symmetric lancet design, was similar to previously documented structures [70], [77]–[79], but with two improvements. The rotation points were strategically positioned along the pointer axes (Figure 40(a)), and the pointer was tilted to the maximum angle (θ) that would still fit within the desired footprint. The second structure, called the C-shaped rotational structure, was a completely original design for this field. The MEMS rotational structures shown in Figure 40 consisted of various interconnected components that worked together to achieve rotational motion. These components consisted a double set of opposing thermal actuators made up of chevron beams, a rotational mechanism, a straight beam, and a tilted arm. The straight beam and rotational mechanism were responsible for facilitating movement and ensuring that the tilted arm rotated smoothly and efficiently.

Both MEMS rotational structures use actuators as the source of input force and displacement. There are several driving devices available in the literature that are capable of producing displacements, such as electrostatic, piezoelectric, electromagnetic, and electrothermal actuators [98]. Each of these devices has its own advantages and disadvantages. The choice of the optimal driving mechanism for actuation depends on specific application requirements, including force output, displacement range, cost, and size. For instance, electrostatic actuators have high force generation but limited displacement. Piezoelectric actuators offer high force density and large displacement, but they can be relatively expensive. Electromagnetic actuators can generate substantial forces and displacements, but they typically require magnetic fields and may be bulky [99].

Conversely, electrothermal actuators exploit the thermal expansion of materials due to electrical current flow, resulting in significant force generation. Electrothermal actuators are often preferred when compactness, low voltage, large output force, and stability are of utmost importance [75].

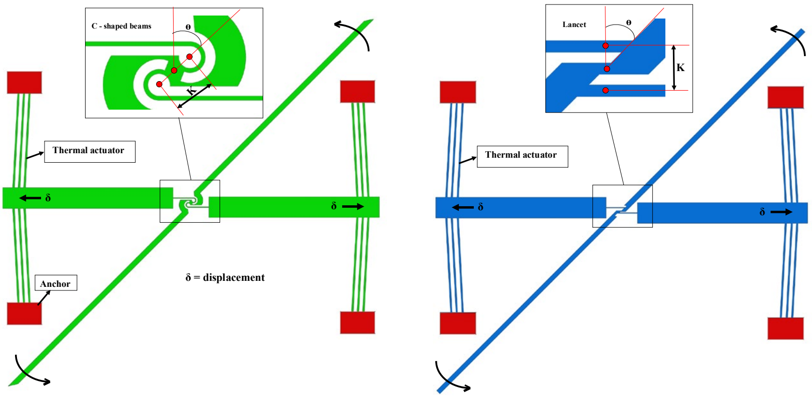

(a) (b)

Figure 40. Schematics of the two investigated MEMS rotational structures: (a) symmetric lancet and (b) symmetrical C-shaped structures.

MEMS rotational structures are highly suitable for use in microscale systems that require precise control over their motion. The criticality of the rotational mechanism design is evident in its impact on the overall performance of the rotating MEMS structure. The selection of design parameters for the symmetric lancet MEMS rotational structure was based on relevant literature sources [70], [78], [100], whereas the optimization of the C-shaped MEMS rotational structure employed the design of experiments (DOE) method [101] and analytical modeling. The optimization process involved systematic testing of various design combinations to determine the optimal configuration for the C-shaped structure, taking into account the specific requirements and limitations of the application, including fabrication constraints.

5.1.1. Working principle of the C-shaped based displacement magnification mechanism

In our MEMS rotational structures, the actuation of a thermal actuator resulted in linear motion that was then transmitted to the central shuttle and straight beam. Subsequently, the rotational mechanisms transformed this linear motion into rotational motion, which could be utilized for a variety of microelectromechanical applications. By integrating thermal actuators on both sides of the central shuttle and straight beam, more precise control over the rotational displacement produced by the device as depicted in Figure 40.

5.2. Parameter optimization by using DOE method

Design of experiments (DOE) is a statistical technique employed to identify the correlation between the independent variables (factors) and the dependent variables (responses or outputs) of a given process or system. This method facilitates a systematic investigation and optimization of complex systems, processes, or designs. DOE helps in identifying the most significant factors that affect the output performance, as well as their interactions, and optimizes the system to achieve maximum efficiency and effectiveness. Various approaches exist, such as one-factor, factorial design, robust parameter design, and reliability design, are available to analyze and enhance the system output response [102], [103].

The response surface method (RSM) in combination with central composite design (CCD) run via JMP® statistical software was used to optimize the design parameters of our innovative MEMS rotational structure. RSM is a widely utilized multivariate technique that models the relationship between a dependent variable (response) and multiple independent variables [103], [104]. The focus of this study was investigating the impact of two parameters that characterize the geometry of the C-shaped hinge: the curved beam width (W) and the gap (K) between the upper and lower curved beam centers of rotation. These parameters were identified as the independent variables that influence the response of the system, specifically the displacement at the tip of the tilted arm. To determine the optimal values for these independent variables, three levels were chosen for each factor: low (-), medium (0), and high (+). Taking into account fabrication limits, the low and high levels for W were set at 2.3 µm and 6 µm, respectively. Additionally, an intermediate level of 4.5 µm was considered. Similarly, the low and high levels for K were set at 15 µm and 30 µm, respectively, with an intermediate level at 22.5 µm. For each combination of W and K, finite element method (FEM)-based 3D thermal-electric-structural simulations in the Ansys software were conducted to determine the corresponding displacement at the tip of the tilted arm. The use of RSM in conjunction with CCD enabled a comprehensive investigation of the effect of the independent variables on the response and the identification of the optimal design parameters for the structures.

The total variation in the output response of each factor can be assessed by computing the total sources of variance, referred to as SST. SST comprises of two components: factor sum of squares (SSA), which accounts for the effects of the factors, and error sum of squares (SSE), which represents random error. These values can be calculated by using the following formulas [103]:

$$SS_T = SS_A + SS_E \tag{31}$$

$$SS_A = \sum_{i=1}^{a} \sum_{j=1}^{n_i} (\bar{y}_{ij} - \bar{y})^2 \tag{32}$$

$$SS_E = \sum_{i=1}^{a} \sum_{j=1}^{n_i} (y_{ij} - \overline{y_{ij}})^2 \tag{33}$$

Where $\bar{y}_{ij}$ is the factor level group mean, $\bar{y}$ is the overall mean, a is the number of levels of the factor, y_{ij} is the j^{th} response in the i^{th} factor level and n_i is the number for which the factor is at level i.

To determine the significant factors influencing the output response, an F test based on ANOVA (analysis of variance) can be performed. This test investigates the following hypothesis for each factor (μ_i):

$H_0: \mu_1 = \mu_2 = \cdots = \mu_a$

$H_1: \mu_i \neq \mu_j$ for at least one pair (*i,j*)

The F-value (F_0) can be obtained by:

$$F_0 = \frac{SS_A/a-1}{SS_A/N-a} = \frac{MS_A}{MS_E} \tag{34}$$

Where $(a-1)$ is the degrees of freedom for factor A, $(N-a)$ is the error degrees of freedom MS_A, and MS_E are the mean sum of squares and the error sum of squares for factor A, respectively. If F_0 is higher than the threshold value $F_{\alpha,a-1,N-a}$, where α is the level of significance, the null hypothesis is rejected. The analysis of variance for the two factors is presented in Table 5 along with the corresponding F and p values. The relevant factors impacting the output response are thought to be screened out at the 95% level of significance (p value <0.05) [103].

Table 5. Effect test results from JMP® Statistical Software.

Varying Factor	Degree of freedom	Sum of squares	F-value (F_0)	P-value (<0.05)	Significance
W	1	17.647350	814.1799	0.0012	Yes
K	1	0.007350	0.3391	0.6193	No
W:K	1	0.497025	22.9308	0.0409	Yes
W:W	1	0.232408	10.7224	0.0820	No
K:K	1	0.023408	1.0800	0.4078	No

The DOE findings indicated that the model had statistical significance based on the p-value, which was below 0.05. The output displacements were most affected by the minimal gap between the centers of rotation of the two curved beams and a smaller hinge width. This was evident from the results presented in Table 5. Specifically, the results showed that changes in the width of the curved beam (W) had the greatest impact on the output displacement (1st row of Table 5) when all other parameters were held constant. Furthermore, the combination of the curved beam width (W) and hinge gaps (K) had a secondary influence on the performance (3rd row of Table 5). This finding can be valuable when optimizing the parameters of the MEMS device as it highlights the significance of these specific design factors in determining overall performance.

Based on these findings, we conducted a performance analysis using Ansys® software on the symmetrical C-shaped rotational structure. We examined how the variations in curved beam width (Figure 41(a)) and the gap between the curved beam's center of rotation (Figure 41(b)) affected the system. These results were consistent with the observations made in the DOE analysis presented in Table 6. Specifically, both parameters had an impact on the system response, but the nature of their influence was different. In particular, reducing the width of the curved beam and the gap between the centers of rotation led to an increase in displacement, making the system more sensitive to changes in the first parameter compared to the second parameter. Within the range considered, the best performance was achieved with a width of 2.3 µm and a gap of 14.6 µm, which were the values used for device fabrication.

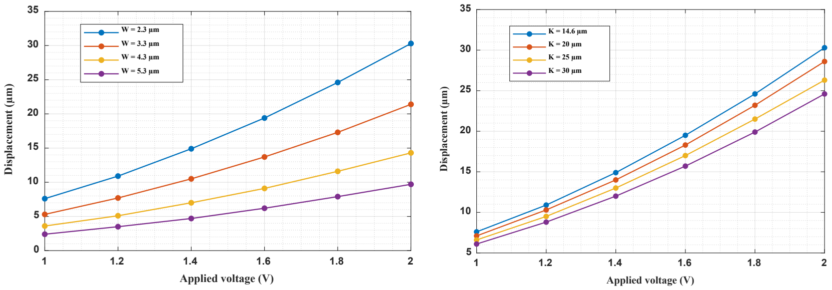

(a) (b)

Figure 41. Performance analysis of the symmetrical C-shaped rotational structure: dependence of the output displacement on (a) the curved beam width and (b) the gap between the hinges center of rotation.

5.3. Analytical modeling

Due to the symmetrical nature of the C-shaped rotational structure, we can analyze its behavior by simplifying it to the structure shown in Figure 42(c). This simplified version consists of a straight beam (AB) with a length of x_s, connected to a curved beam (BC) with a radius of R, and further connected to a rigid element DC with a length of x_r. Regarding the boundary conditions, we can assume the presence of a slider at point A, which accounts for the thermal actuator delivering horizontal displacement and force (F_A), and a hinge at point D, as the structure can freely rotate around it.

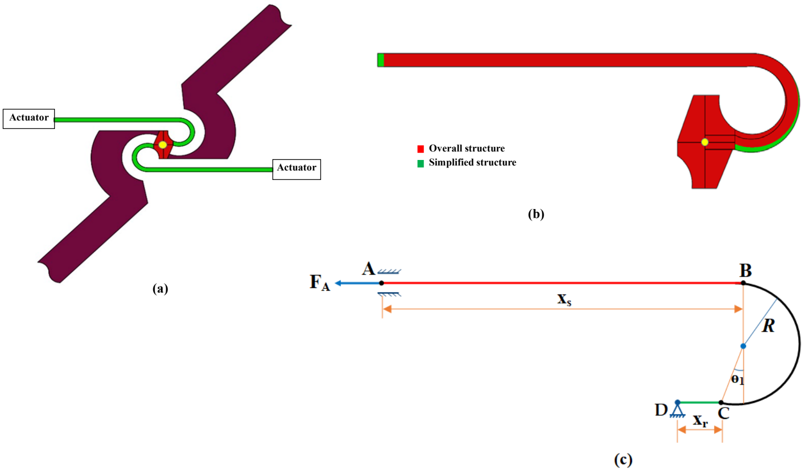

Figure 42. Schematic diagram of symmetrical C-shaped structure implemented in the real device (a), comparison between the designed and simplified curved beam structure (b) studied in the analytical model (c).

To calculate the horizontal displacement (δ_A) of the straight beam (which serves as the input to the system), we employed Castigliano's second theorem. This theorem allows us to express the displacement as a function of the force exerted by the thermal actuator (F_A) [105], [106]. According to this theorem, in a linearly elastic structure, if the strain energy can be expressed as a function of the generalized force, F_i, then the generalized displacement δ_i in the direction of F_i can be determined by taking the partial derivative of the total strain energy, U_{total}, with respect to the generalized force, F_i [107]. In our specific case, this calculation yields the following relationship:

$$\delta_A = \frac{\partial U_{total}}{\partial F_A} \tag{35}$$

The total strain energy can be found [29]:

$$\begin{aligned} U_{total} &= U_{straight\ beam} + U_{curved\ beam} \\ &= \int_0^{x_s} \frac{M^2(x\,)}{2EI}\,dx + \int_0^{\pi+\theta_1} \frac{M^2(\alpha)}{2EI} R d\alpha \end{aligned} \tag{36}$$

Where I is the moment of inertia of the cross-section (i.e., $I = \frac{W^3 h}{12}$, being h the thickness) and E the Young's modulus.

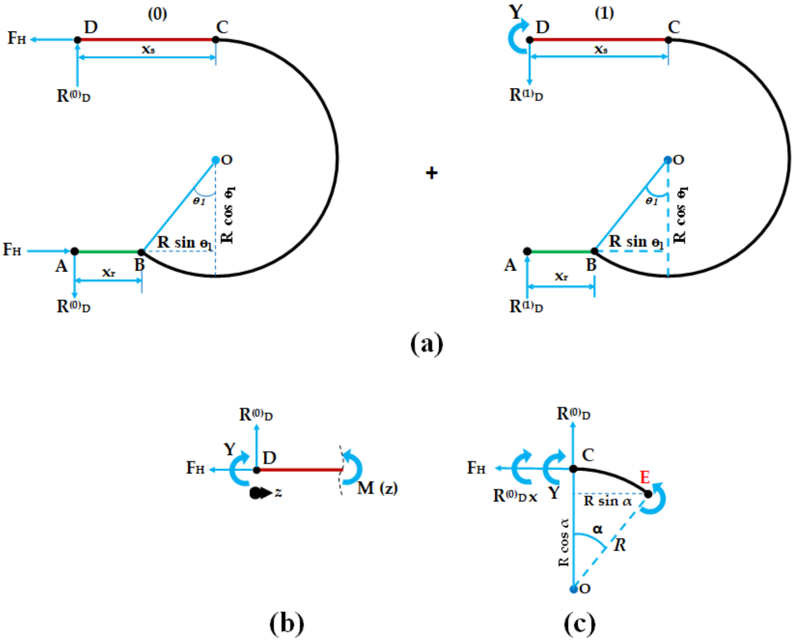

Figure 43. Free body diagrams.

By considering Figure 43, the moment along the straight $M\ (x)$ and the curved $M\ (\alpha)$ beams can be written as follows:

$$\mathrm{M}(x) = \mathrm{R_A} \cdot x + \mathrm{Y} \tag{37}$$

$$\mathrm{M}(\alpha) = -F_A\mathrm{R}(1 - \cos\alpha) + R_A(x_s + R\sin\alpha) + \mathrm{Y} \tag{38}$$

Where R_A and Y are the vertical reaction force and the moment provided by the slider at A, respectively.

R$_\mathrm{A}$ can be computed as $R_A = R_A^{(0)} - YR_A^{(1)}$, being $R_A^{(0)} = \frac{F_A R(1+\cos\theta_1)}{x_s-(x_r+R\sin\theta_1)}$ and $R_A^{(1)} = \frac{1}{x_s-(x_r+R\sin\theta_1)}$

While Y can be computed for example by the virtual work method as:

$$\mathrm{Y} = -\left(\frac{\left[-R_A^{(0)}R_A^{(1)}\left(\frac{z^3}{3}\right) + R_A^{(0)}\left(\frac{z^2}{2}\right)\right]_{z=0}^{z=x_s} + \left[\begin{matrix}-R_A^{(1)}F_AR^2\cos\alpha - R_A^{(1)}F_AR^2\left(\frac{\sin^2\alpha}{2}\right) + R_A^{(1)}F_ARx_s\alpha - R_A^{(1)}F_ARx_s\sin\alpha - F_AR\alpha + F_AR\sin\alpha - R_A^{(0)}R_A^{(1)}R^2\left(\frac{\alpha}{2}-\frac{\sin 2\alpha}{4}\right)\\ - R_A^{(0)}R\cos\alpha - R_A^{(0)}R_A^{(1)}{x_s}^2\alpha + 2R_A^{(0)}R_A^{(1)}Rx_s\cos\alpha + R_A^{(0)}x_s\alpha\end{matrix}\right]_{\alpha=0}^{\alpha=\pi+\theta_1}}{\left[{R_A^{(1)}}^2\left(\frac{z^3}{3}\right) - 2R_A^{(1)}\left(\frac{z^2}{2}\right) + z\right]_{z=0}^{z=x_s} + \left[{R_A^{(1)}}^2{x_s}^2\alpha - 2{R_A^{(1)}}^2Rx_s\cos\alpha + {R_A^{(1)}}^2R^2\left(\frac{\alpha}{2}-\frac{\sin 2\alpha}{4}\right) - 2R_A^{(1)}x_s\alpha + 2R_A^{(1)}R\cos\alpha + \alpha\right]_{\alpha=0}^{\alpha=\pi+\theta_1}}\right)$$

For the geometrical parameters, we considered the values reported in Table 6; these were selected to achieve a trade-off between fabrication limits, requirements of a compact design, and high performance, considering the DOE analysis results. Notably, for the simplified structure of Figure 42(b) to correctly reproduce the behavior (i.e., having an overlapping center of rotation) of the original structure (in red in Figure 42(b)), we considered a curved beam with a radius 1.1 larger than that of the original structure.

Table 6. Geometrical parameters of MEMS rotational structures.

Geometrical parameters	Values
Actuator beam length	300 µm
Actuator beam width	4.7 µm
Actuator beam angle	3°
Total number of beams	6
Device thickness	25 µm

Straight beam length	65.5 µm
Straight beam width	2.3 µm
Curved beam width	2.3 µm
Curved beam radius (R)	7.5 µm
Curved beam angle (θ)	34.15°
Gap (K)	14.6 µm
Tilted arm length	780 µm
Tilted arm width	16.7 µm
Angle (θ_1)	34.15°
Curved beam radius (R)	7.5 µm
Width (W)	2.3 µm
Straight beam length (x_s)	65.5 µm
Thickness (h)	25 µm
Rigid beam length (x_r)	5.3 µm

After substituting equations (37) and (38) into equation (36), the strain energies of the straight and the curved beams result to be:

$$U_{straight\ beam} = \frac{1}{2EI}\left[\left(\frac{x^3}{3}\right)\left(\left(R_A^{(0)}\right)^2 - 2R_A^{(0)}R_A^{(1)}Y + {R_A^{(1)}}^2 Y^2\right) + \left(\frac{x^2}{2}\right)\left(2R_A^{(0)}Y - 2R_A^{(1)}Y^2\right) + Y^2 x\right]_{x=0}^{x=x_s} \tag{39}$$

$$U_{curved\ beam} = \frac{1}{2EI}\Bigg[-2YF_AR^2\alpha\left(1 + R_A^{(1)}x_s\right) + F_AR^2 \sin\alpha\left(2Y + 2R_A^{(0)}x_s - 2F_AR\right) + R\alpha\left(YR_A^{(0)}x_s + Y^2{R_A^{(1)}}^2{x_s}^2 - 2YR_A^{(0)}R_A^{(1)}{x_s}^2 + \left(R_A^{(0)}\right)^2{x_s}^2 + \left(R_A^{(0)}\right)x_sY\right) - 2YR_A^{(0)}R^2\cos\alpha\left(1 + 2R_A^{(1)}x_s\right) + 2Y^2R_A^{(1)}R^2\cos\alpha - Y^2R\alpha\left(2R_A^{(1)}x_s + 1\right) - 2YR_A^{(1)}x_sF_AR^2\sin\alpha - 2YR_A^{(1)}R^2\cos\alpha\left(YR_A^{(1)}x_s - F_AR\right) - R^3\left(\frac{\alpha}{2} - \frac{\sin 2\alpha}{4}\right)\left(2YR_A^{(0)}R_A^{(1)} - Y^2{R_A^{(1)}}^2 - \left(R_A^{(0)}\right)^2\right) + 2R_A^{(0)}R^2\cos\alpha\left(F_AR - R_A^{(0)}x_s\right) + 2R_A^{(0)}F_AR^3\left(\frac{\sin^2\alpha}{2}\right) - \alpha\left(2R_A^{(0)}FR^2x_s + {F_A}^2R^3\right) + {F_A}^2R^3\left(\frac{\alpha}{2} + \frac{\sin 2\alpha}{4}\right)\Bigg]_{\alpha=0}^{\alpha=\pi+\theta_1} \tag{40}$$

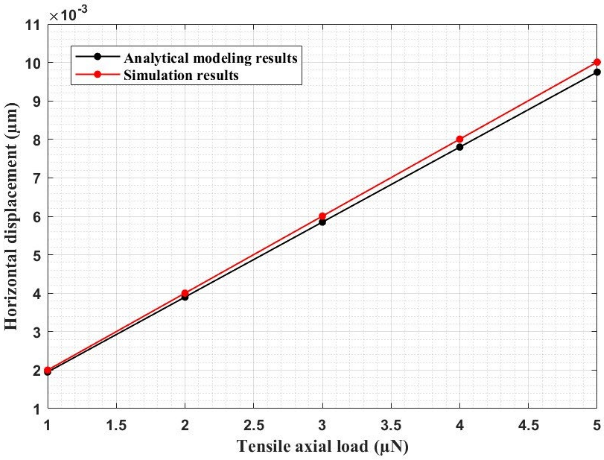

Figure 44. Comparison between the horizontal displacement at the beginning of straight beam obtained from analytical modeling and numerical simulations as a function of the force delivered by the thermal actuators.

Figure 44 illustrates the relationship between the displacement δ_A and the force F_A, which was obtained using equation (35). The strain energy was computed based on equation (39), and the FEM-based structural analysis was conducted using Ansys® software. As expected, the δ_A-F_A relationship is linear, with the slope from the numerical simulations being very similar to that obtained from the analytical model (i.e., a difference of 2.6%). These results indicate the accuracy of the analytical model in predicting the behavior of the structure.

By substituting equations (39)-(40) into equations (36) and (35), it is possible to derive an analytical expression that demonstrates how δ_A varies with different geometrical quantities, such as the width and radius of the curved beam, the length of the straight beam, and the angle of the curved beam (see Appendix - B).

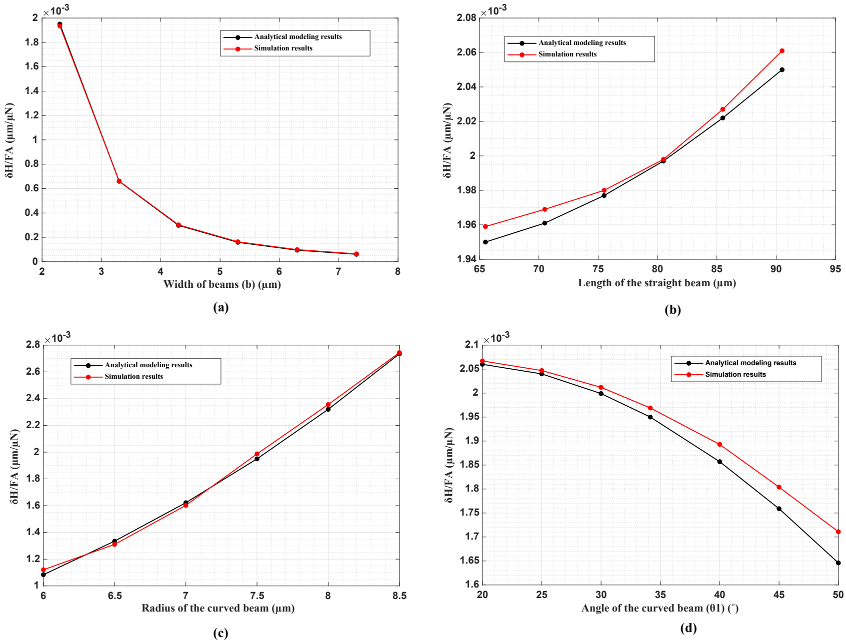

Figure 45. Investigating the impact of symmetrical C-shape geometry on the displacement at the beginning of the straight beam determined from the analytical model based on Castigliano's second theorem: study of (a) curved and straight beams width, (b) straight beam length, (c)curved beam radius, and (d) angle.

For instance, Figure 45(a) presents the relationship between δ_A and the width of the curved and straight beams, as determined by Appendix equation (B.1). The results show that as the beam width increases, the displacement decreases, reaching its maximum value at a beam width of 2.3 µm, as also predicted by the DOE results presented in the previous section.

In Figure 45(b)-(d), δ_A is shown as a function of the length of the straight beam, as well as the radius and angle of the curved beam. The plots, which are based on the expressions B.2–4 in the Appendix, demonstrate that the displacement increases almost linearly as the length of the straight beam (particularly after 70.5 µm) and the radius of the curved beam are increased. However, when the angle of the curved beam is increased, the displacement is significantly reduced.

In addition to the results of the analytical model, Figure 45 also presents the results obtained from FEM-based structural analysis, which show a good agreement.

5.4. Multiphysics simulations

Coupled multiphysics simulations were conducted on both the novel C-shaped and symmetrical lancet (for comparison) rotational structures using the Ansys® finite element software in thermal-electric-structural interaction mode. The actuator anchors were mechanically fixed in the structural boundary conditions, while all other boundaries were free to move. The faces in contact with the substrate were set at a constant temperature of 22 °C for the thermal boundary conditions. In the electrical domain, a DC voltage was applied between the actuator anchors (contact pads), resulting in both temperature and displacement fields in the MEMS rotational structure output. When voltage is applied across the anchors, heat is generated due to Joule heating and simultaneously dissipated until it reaches a steady state of heat balance. The dimensions used in the simulations are listed in Table 6. The silicon material properties used in the simulations can be found in Table 7.

Table 7. Silicon properties [108].

Material properties	Values
Young’s modulus (E)	169 GPa
Poisson's ratio (ν)	0.28
Density (ρ)	2330 kg/m^3
Thermal conductivity (K)	130 [W/(m·K)]
Coefficient of thermal expansion (α)	2.6×10^{-6} K^{-1}
Resistivity	0.005 Ω·cm

The lancet and symmetrical C-shaped MEMS-based rotational structures have same width, thickness, length, and number of chevron beams in the thermal actuators, as well as the same straight beam and tilted arm geometry, shuttle lengths, and rotational hinge angles.

Due to the dissipation of heat through the anchors in a vacuum, the shuttle area experienced the highest temperatures, as it was the farthest from the anchors. As a result, temperatures were not uniform. This non-uniformity also led to non-uniform displacement in the device, as illustrated in Figure 46. Figure 46 also depicts the distribution of stress and displacement in both MEMS rotational structures when a voltage of 2 V is applied. The data from the simulations showed that the symmetric lancet structure had a maximum displacement of 23.9 µm and a stress value of 229 MPa (Figure 46(a)). On the other hand, the symmetrical C-shaped structure performed better, achieving a higher output displacement (31.8 µm) and lower stress (176 MPa) at the same actuation voltage (Figure 46(b)).

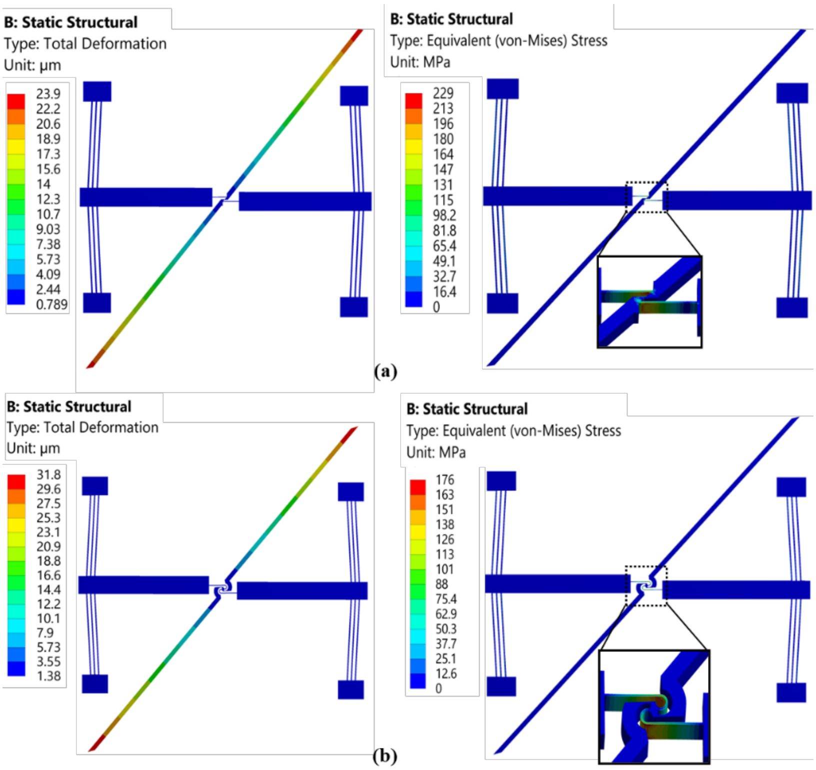

Figure 46. Maximum displacement and stress when the actuators are biased with 2V in symmetrical C-shape (a) and symmetrical lancet structure (b).

Microfabrication, electrical characterization and packaging

6.1. Microfabrication techniques

Typically, microgrippers and rotational structures have been developed using two main fabrication techniques: surface micromachining and bulk micromachining. Surface micromachining is a well-established process for the fabrication of MEMS structures involving the deposition of thin films, often using methods like low-pressure chemical vapor deposition (LPCVD) or physical vapor deposition (PVD), on a substrate surface. These films are then selectively etched and patterned to form the desired device structure. However, these thin films deposited during surface micromachining can often exhibit residual stress due to various factors like processing conditions used during the deposition, type of material system (thin films and substrate materials) and other processing steps performed after the thin-film layer deposition, particularly those involving exposure to elevated temperatures [109]. This residual stress can accumulate and lead to mechanical instabilities in the fabricated structures. High levels of residual stress might cause buckling, warping, or even cracking of the thin films or devices upon release from sacrificial layers.

On the other hand, bulk micromachining involves the deep etching of the substrate material, typically silicon, to create the desired device structures. This approach has certain advantages over surface micromachining. Firstly, it leverages the properties of single-crystal silicon to produce structures that are more robust and stable compared to the thin films used in surface micromachining. Thin films are more prone to deformations and long-term stability issues. Secondly, bulk micromachining uses anisotropic etching processes to produce oriented structures with three-dimensional dimensions and shapes. Moreover, the mechanical superiority of single-crystal silicon enhances the appeal of micromachining as it provides stiffness, strength, and wear resistance, all of which are crucial attributes for MEMS devices that require robust mechanical integrity. Additionally, bulk micromachining helps address challenges related to stress during fabrication in comparison to surface micromachining, which involves film deposition and release procedures that introduce significant residual stresses that can adversely impact performance. The choice between surface and bulk micromachining depends on the specific requirements of the application at hand. While surface micromachining provides versatility and cost effectiveness, bulk micromachining is better suited for applications that prioritize reliability, stability, and intricate three-dimensional structures.

In this particular study, we have developed a novel MEMS-based microgripper and rotational structure (embedding C-shaped symmetrical hinges to provide displacement magnification capability). The fabrication of these devices was carried out using a bulk micromachining process with silicon-on-insulator (SOI) wafers. These SOI wafers are composed of a top layer made of single-crystal silicon, an insulating layer, and a bottom layer called the handle layer [110]. The use of SOI wafers have several advantages over traditional silicon bulk substrates. Firstly, SOI wafers exhibit lower residual stresses in the structural layer, resulting in higher quality and reliability. Secondly, the insulating layer serves as an excellent etch stop, thereby simplifying the fabrication process. Thirdly, the isolation of the single-crystal layer from the bulk substrate leads to lower parasitic capacitances, enabling the creation of high-speed devices with lower power consumption. Lastly, the complete isolation of n-well and p-well devices in the SOI wafers provides protection against latch-up effects and enhances the radiation hardness [111]. Leveraging the advantages provided by SOI wafers, our novel microgripper and rotational structure exhibit excellent mechanical robustness.

6.1.1. Fabrication of devices

I. Front DRIE

Both devices were fabricated using a 6-inch SEMI standard SOI wafer as the starting material. The SOI wafer consisted of three layers: a device layer with a thickness of 25 μm, a buried SiO_2 layer with a thickness of 1.5 μm, and a handle layer with a thickness of 525 μm. The fabrication process involved six main steps, which were similar to previously reported microfabrication procedures in [112]–[114].

The microfabrication process (Figure 48) began with cleaning the wafer using a standard RCA (Radio Corporation of America) cleaning method to remove any organic and ionic contaminants. The first and second steps included depositing an 800 nm thick layer of aluminum and then patterning the aluminum thin film to define the connection pads on the SOI wafer (Figure 48(b) and (c)). In the third step, a 600 nm thick protective layer was deposited on top of the patterned aluminum using a PlasmaPro 100 Cobra ICP PECVD (plasma enhanced chemical vapordeposition) tool. Following that, a sputtered aluminum layer with a thickness of 150 nm and a silicon oxide layer with a thickness of 200 nm were deposited as masking layers to remove the presence of micromasking [114] using a PECVD process.

In order to expose the underlying silicon, the layers were patterned with stepper photolithography and etched in a plasma etching process. Next, the exposed silicon device layer was etched down to the buried oxide layer using an Alcatel AMS200 DRIE process, which allowed for anisotropic etching with higher selectivity and verticality. This fourth step was crucial in outlining the main features of the device. In the fifth step, a combination of dielectric and metal etchers were used to etch the masking layers and form the device. Finally, the sacrificial islands and buried oxide layer were etched using HF vapor etching with an SPTS Primaxx® uEtch etcher from SPTS Technologies Ltd, resulting in the release of the device.

II. Back DRIE

In our microgripper device, we have implemented underpass technology to separate the gripping mechanism from the electrothermal actuation system, as shown in Figure 47. The use of underpass technology ensures that the operation and integrity of the gripping mechanism are not affected by electrical signals or disturbances from other parts of the device, such as the electrothermal actuation system. This separation is crucial for the independent functioning of different components within the microgripper device, which enhances its reliability, performance, and functionality.

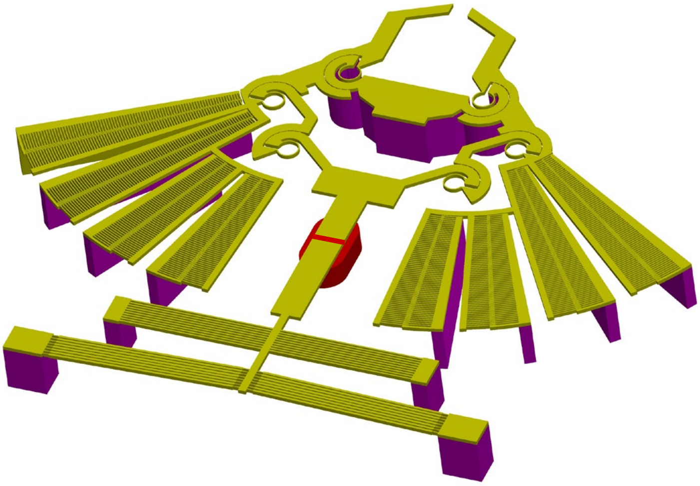

(a)

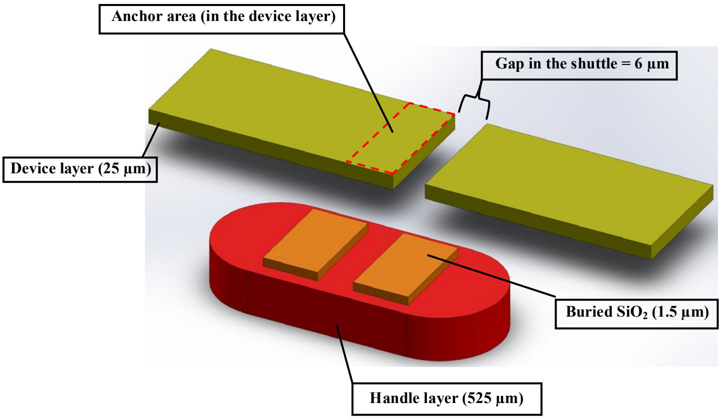

(b)

Figure 47. (a) Full microgripper structure with underpass, and (b) details of the underpass.

Furthermore, the underpass is constructed using Backside Deep Reactive Ion Etching. The same procedure is carried out on the backside of the wafer (Figure 48(a') and (b')), where an identical Aluminum mask is deposited and patterned, followed by DRIE to eliminate the bulk silicon until reaching the buried oxide layer. The devices are now held in place by the buried silicon oxide, which is dissolved by wet etching in an HF-based solution to release them.

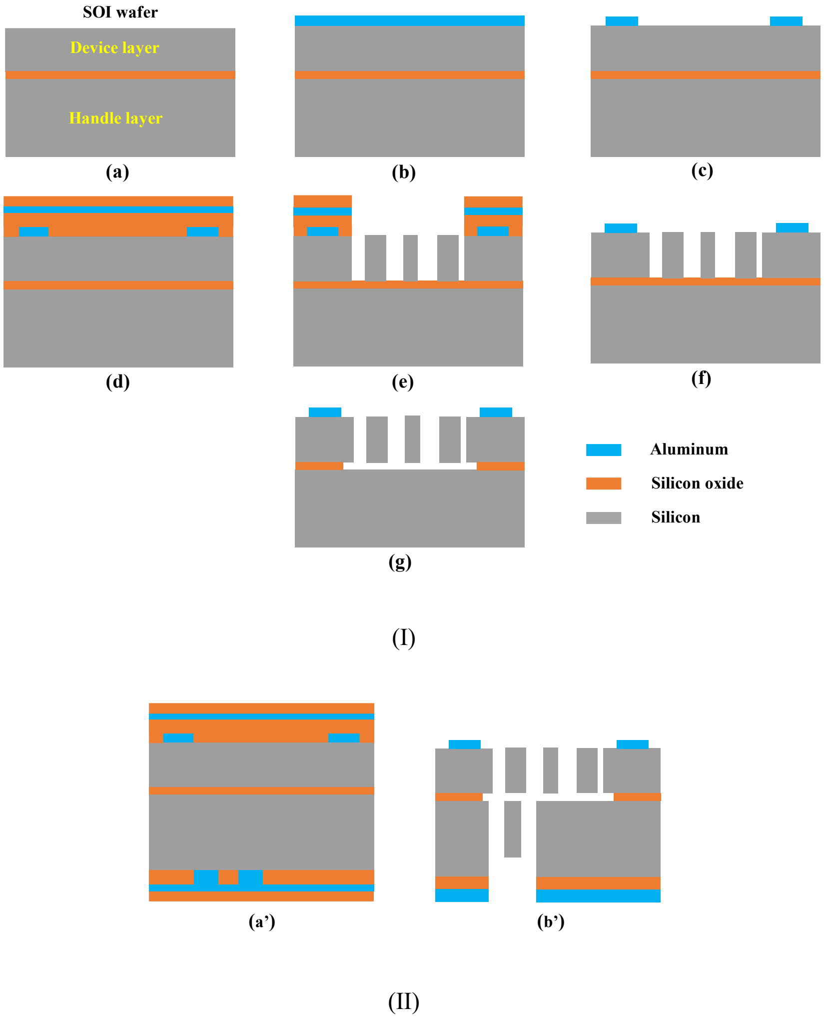

Figure 48. Process sequence and main steps for the fabrication of the devices: (I) Front DRIE process, and (II) Back DRIE process.

6.2. Experimental characterization of the microgripper and the rotating structure

The devices were fabricated according to the process outlined in Figure 48(I) and (II), and after fabrication, they appeared as shown in the scanning electron microscope (SEM) images of Figure 49(a), (b) and (c) including the underpass.

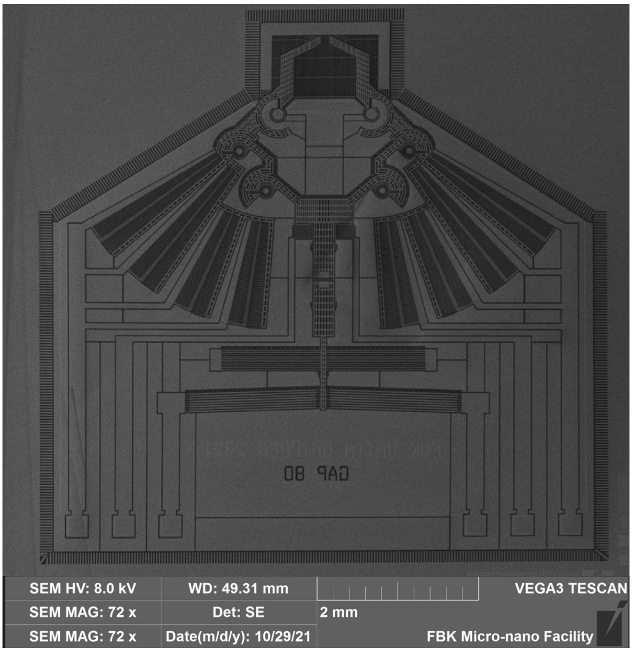

(a)

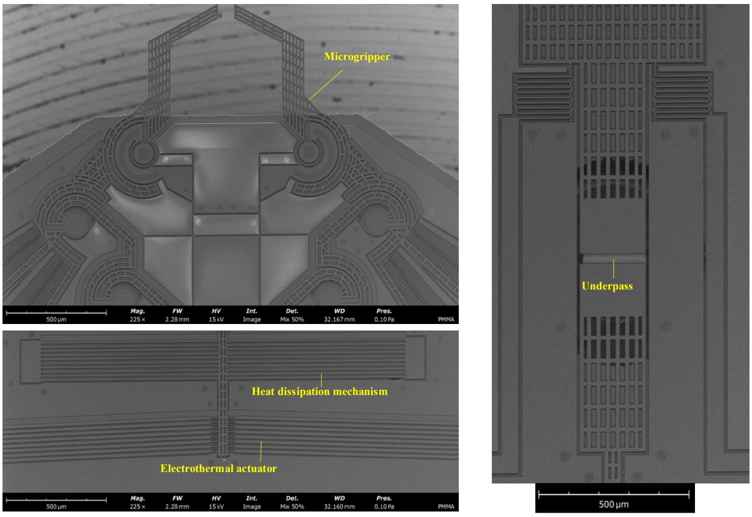

(b)

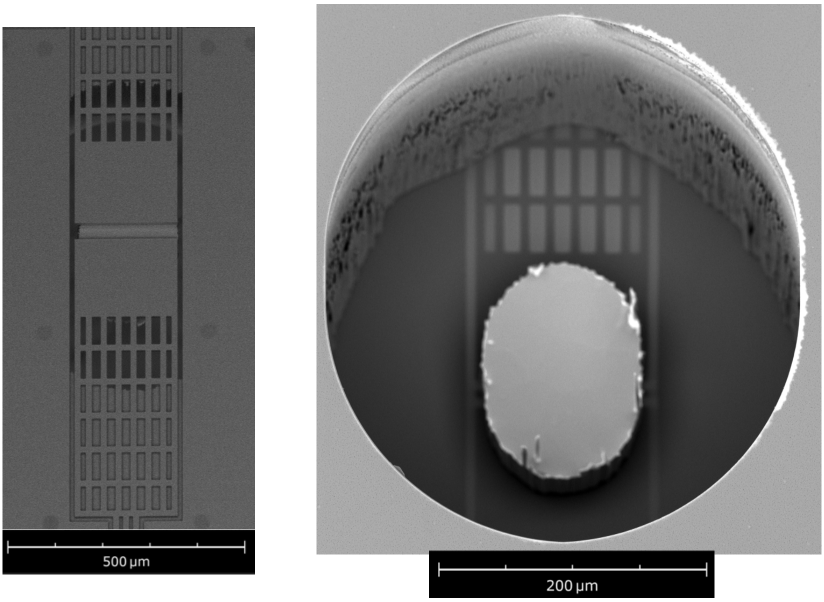

(c)

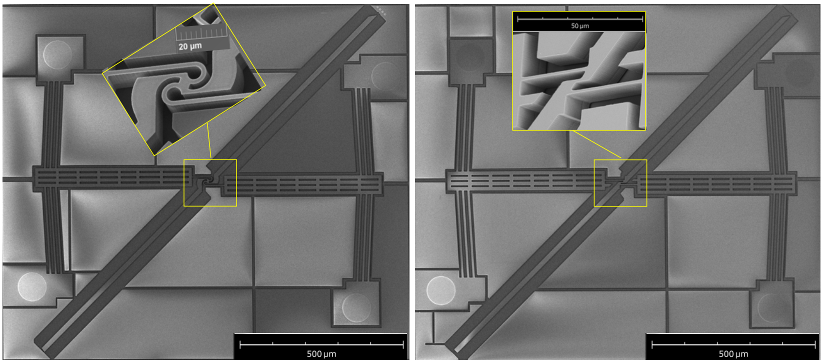

(d)

Figure 49. (a) Overall microgripper structure before HF release, (b) Main parts of the structure after HF release, (c) Front and back side view of the released underpass, and (d) Completely released symmetric lancet and C-shaped rotational structures.

6.2.1. Electrical DC experiments

The I-V sweep technique involves systematically varying the applied voltage across a device or component while measuring the resulting current. This method enables the characterization of the devices behavior concerning voltage variations, generating I-V curves that illustrate its electrical characteristics.

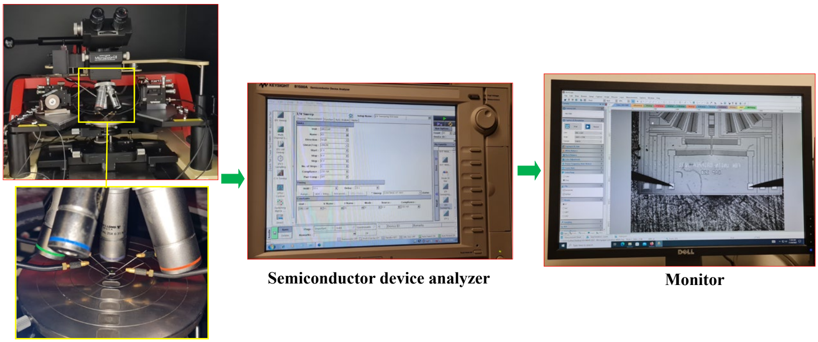

Semiconductor device analyzer

Monitor

Manual probe station

Figure 50. Experimental set up of the actuation system.

I. Microgripper

We carried out a preliminary experiment to measure the displacement of the actuator shuttle and the total displacement of the tweezers at different voltage ranges (ranging from 2V to 6V) in order to evaluate the performance of the gripper mechanism. Once we obtained these experimental values, we used the displacement of the actuator shuttle as an input for a static structural analysis of the gripper mechanism using Ansys. This simulation enabled us to determine the predicted total displacement of the tweezers based on the structural analysis. Finally, we compared the results obtained from the simulation (total tweezers displacement calculated using the input of actuator shuttle displacement) with the experimental results of the total tweezers displacement obtained directly from the experiments.

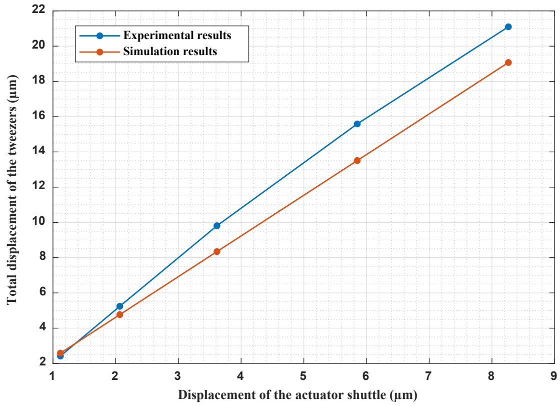

Figure 51. Comparison of experimental and simulation results of total tweezers displacement.

Figure 51 shows the comparison of experimental and simulation results of total tweezers displacement. This comparison is based on both experimental and simulation results, and they had a maximum difference of approximately 15 %.

II. C-shaped hinge

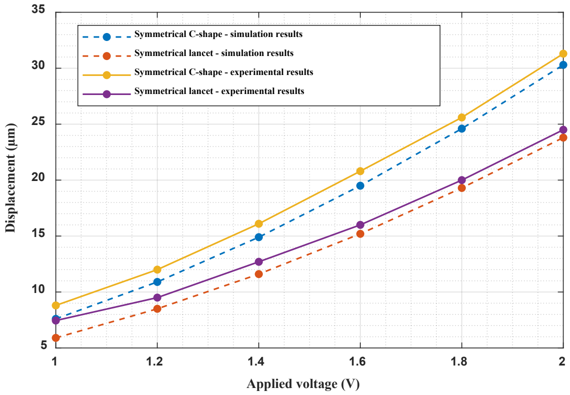

Figure 52. Comparative analysis of the symmetrical lancet and C-shaped MEMS rotational structures: simulation and experimental results.

Figure 52 illustrates the comparison of the displacement at the tilted arm tip between two structures: the symmetric lancet and the C-shaped MEMS rotational structures. This comparison is based on both multiphysics simulations and experimental results. The curves of the experimental and numerical results started to diverge at lower voltages due to fabrication tolerances. These tolerances resulted in thinner structures, which in turn led to increased displacement. In the case of the C-shaped MEMS rotational structure, the difference between the experimental and simulation results was higher at lower voltages, approximately 12 %. However, this difference gradually decreased to a maximum of 3.3 % at higher voltages. On the other hand, the symmetrical lancet structure had a maximum difference of approximately 2.9 % at higher voltages. This divergence could be attributed to environmental factors, such as air resistance. In comparison between the symmetrical C-shaped and lancet structures, as discussed in the previous section, it was observed that the C-shaped structure always had a larger maximum displacement. At 2 V, the C-shaped structure exhibited an increase of about 28 % compared to the symmetrical lancet model.

6.3. Packaging of the microgripper

Like many sensors, actuators, and electromechanical systems, most MEMS devices require a certain level of protection from different environmental conditions. Depending on the specific device, the packaging may be responsible for isolating it from temperature, protecting it from humidity, dust, and debris, withstanding harsh chemicals, suppressing electrical noise, or meeting a wide range of other requirements. Moreover, the packaging often needs to allow certain interactions outside of the package. For instance, various MEMS devices need to establish electrical contact with external circuitry. Therefore, the packaging of MEMS is a crucial consideration in the overall system [115].

The designed microgripper will be packaged in a liquid proof housing to enable the first ever MEMS microgripper operation in liquid environment immersion, as required for in vitro manipulation of biological samples. The preliminary design of the packaging, which includes the chip and other components, is depicted in Figures 53. The packaging will consist of a lower (support) and upper (sealing) covers that will enclose the silicon chip. Distance from the top cover will be granted by metal spacers embedded in the silicon device, to allow for the free movement of the chip parts. This arrangement will create a chamber between the top cover and the chip, in which all moving parts will be enclosed. Moreover, this chamber cannot be completely sealed against water, there will be two openings at the front where the gripper tweezers are located. To prevent any leaks from these small openings, either a hydrophobic coating or an overpressure will be applied inside the chamber.

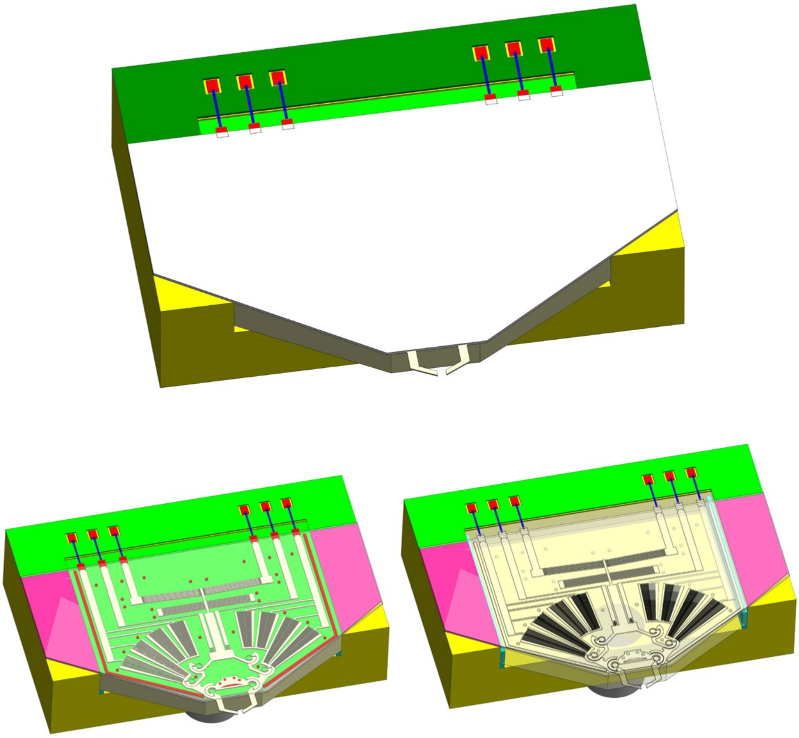

Figure 53. 3D assembly of the packaging system with the chip.

6.3.1. Construction of the packaging system

The development of a packaging system for microgrippers used in MEMS (Micro-Electro-Mechanical Systems) involves the creation and construction of protective enclosures and support structures. These components are essential for guaranteeing the dependability, effectiveness, and durability of these small-scale devices. Our packaging system comprises a top glass cover, a bottom plastic support, a silicon or plastic pipe, and a PCB, as shown in Figure 54 and 55.

First, PDMS or polymer layer is placed from the front of the assembly, and then the chip is smoothly slid onto it. After that, the glass cover is glued to the lower plastic support. Following this step, resin is dispensed between the chip and the plastic support, ensuring a secure lock. Finally, the pipe is attached to the opening on the bottom surface of the plastic support using glue, and then the lower side of the pipe is coated with resin.

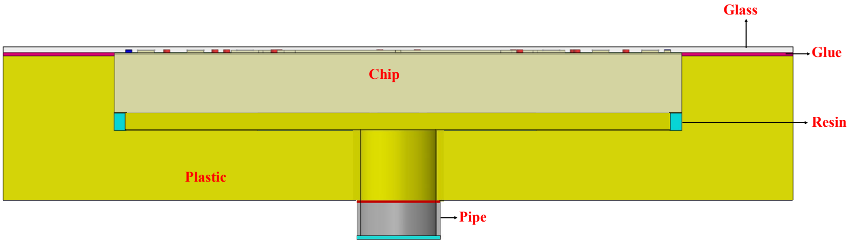

Figure 54. Full sectional view of the packaging system with the chip.

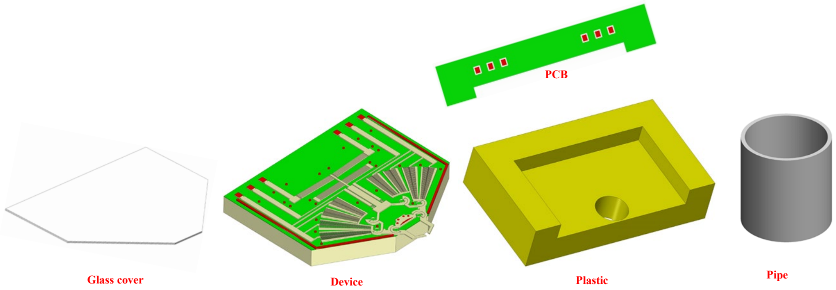

Figure 55. Main components of the packaging system.

Conclusions and Future research

The designed microgripper is intended for use in a liquid environment, and it adopts CSFH to achieve a compact design and to further amplify the displacement. To prevent damage to biological samples caused by high temperatures in the tweezers area, the conduction dissipation type heat sink beams are added to the central shuttle of the actuator. Moreover, rotary type capacitive sensors are implemented on the links of the compliant mechanism to ensure the safety of the gripper structure and provide position feedback. The developed microgripper has the capability to grip biological cells in the size range between 15 to 120 µm. In order to prevent any damage to the biological samples due to high temperature, it is necessary to maintain an ambient temperature of 22 °C in the tweezers region. During the design phase, certain limitations based on fabrication technology are considered, such as a minimum feature size of 6µm and a minimum gap size of 2µm.

An equation for the displacement amplification factor is developed using a kinematics modeling approach based on the pseudo-rigid-body method (PRBM), and this equation is then verified using FEM-based simulations. When the amplification ratio values from analytical modeling and simulations are compared, there is an excellent match with a relative difference of only 1%, demonstrating the effectiveness of the PRBM approach in modeling the kinematics of the structure under investigation. Furthermore, the design of the electrothermal actuator and heat dissipation mechanism is optimized using analytical modeling based on the finite elements method (FEM). The theoretical modeling is validated using FEM-based simulations, which show good agreement between the displacements derived from analytical modeling and simulations. The temperature difference (ΔT) across a range from room temperature to 278°C exhibits a relative difference of ~2.8%. In order to ensure the operation and integrity of the gripping mechanism are not affected by electrical signals or disturbances from other parts of the device, such as the electrothermal actuation system, underpass technology is implemented. This separation is crucial for the independent functioning of different components within the microgripper device, which in turn improves its reliability, performance, and functionality.

In addition to the study on the microgripper, we have developed a new and high-performing symmetrical C-shaped MEMS hinge to contribute to the advancement of MEMS technology. In this study, we demonstrated its ability to amplify displacement when used in a planar rotational structure, and we compared its performance to that of a traditional symmetrical lancet structure. Through the DOE method, we optimized the geometry of our proposed device, focusing on the width of the C-shaped mechanism and the distance between the centers of rotation of the C beams. These geometric parameters had a significant impact on the overall device performance, specifically the displacement at the tip of the tilted arm. Experimental tests revealed that our proposed device exhibited approximately 28% better performance than the symmetrical lancet structure, with the potential for further improvements in the future. Our analytical model, based on Castigliano's second theorem, provided valuable insights into the influence of different geometric parameters (such as angle, radius, and width of the curved beam) on the compliance of the C-shaped mechanism. It can serve as a reference for future designs. Overall, the combination of our experimental, numerical, and analytical findings affirms the validity and accuracy of our proposed hinge design. This design can be implemented in various MEMS rotating structures, replacing standard hinges based on thin straight beams to achieve displacement amplification. This represents a significant step forward in the development of next-generation MEMS devices with enhanced performance and functionality.

Both devices are fabricated using conventional MEMS technology from a silicon-on-insulator (SOI) wafer through the deep reactive ion etching (DRIE) technique. The future research will concentrate on characterizing the microgripper, the capacitive sensor and enclosing the MEMS microgripper in a liquid-resistant housing to allow its operation in a liquid environment. This is necessary for manipulating biological samples in vitro.

Appendixes

Appendix – A – Analytical modeling of the electrothermal actuator

1. Computation of the elastic stiffness matrix in a local reference frame (u′, v′), as shown in Figure 7.

$$[K_e]_{local}\{d\} = \{f_M\} + \{f_T\} \tag{1}$$

where $[K_e]$ is the element stiffness matrix, $\{d\}$ is the nodal displacement vector, $\{f_M\}$ is the mechanical nodal force, and $\{f_T\}$ is the thermal force. The thermal nodal forces can be computed as [40]:

$$\{f_T\} = \begin{Bmatrix} f_{T_i} \\ f_{T_{i+1}} \end{Bmatrix} = \begin{Bmatrix} -\alpha\Delta TEA_i \\ \alpha\Delta TEA_i \end{Bmatrix} i = 1, 2, and\ 3 \tag{2}$$

Element – 1

$$\begin{bmatrix} \frac{EA_1}{L_1} & 0 & 0 & -\frac{EA_1}{L_1} \\ 0 & \frac{12EI_1}{L_1^3} & \frac{6EI_1}{L_1^2} & 0 \\ 0 & \frac{6EI_1}{L_1^2} & \frac{4EI_1}{L_1} & 0 \\ -\frac{EA_1}{L_1} & 0 & 0 & \frac{EA_1}{L_1} \end{bmatrix} \begin{Bmatrix} u'_1 \\ v'_1 \\ u'_2 \\ v'_2 \end{Bmatrix} = \begin{Bmatrix} -\alpha\Delta TEA_1 \\ 0 \\ \alpha\Delta TEA_1 \\ 0 \end{Bmatrix} + \begin{Bmatrix} R_u^{1'} \\ 0 \\ 0 \\ 0 \end{Bmatrix} \tag{3}$$

Element – 2

$$\begin{bmatrix} \frac{EA_2}{L_2} & 0 & 0 & -\frac{EA_2}{L_2} \\ 0 & \frac{12EI_2}{L_2^3} & \frac{6EI_2}{L_2^2} & 0 \\ 0 & \frac{6EI_2}{L_2^2} & \frac{4EI_2}{L_2} & 0 \\ -\frac{EA_2}{L_2} & 0 & 0 & \frac{EA_2}{L_2} \end{bmatrix} \begin{Bmatrix} u'_2 \\ v'_2 \\ u'_3 \\ v'_3 \end{Bmatrix} = \begin{Bmatrix} -\alpha\Delta TEA_2 \\ 0 \\ \alpha\Delta TEA_2 \\ 0 \end{Bmatrix} \tag{4}$$

Element–3

$$\begin{bmatrix} \frac{EA_3}{L_3} & 0 & 0 & -\frac{EA_3}{L_3} \\ 0 & \frac{12EI_3}{L_3^3} & \frac{6EI_2}{L_2^2} & 0 \\ 0 & \frac{6EI_3}{L_3^2} & \frac{4EI_2}{L_3} & 0 \\ -\frac{EA_3}{L_3} & 0 & 0 & \frac{EA_3}{L_3} \end{bmatrix} \begin{Bmatrix} u'_3 \\ v'_3 \\ u'_4 \\ v'_4 \end{Bmatrix} = \begin{Bmatrix} -\alpha\Delta TEA_3 \\ 0 \\ \alpha\Delta TEA_3 \\ 0 \end{Bmatrix} + \begin{Bmatrix} 0 \\ 0 \\ R_u^{4'} \\ 0 \end{Bmatrix} \tag{5}$$

2. Transformation of the local stiffness matrix to global stiffness matrix by means of a rotation matrix.

Relation between local and global stiffness:

$$[K]_{global} = [T]^T[K]_{local}[T] \tag{6}$$

By considering the axial stiffness:

$$[K]_{global-1} = \frac{EA}{L}\begin{bmatrix} c^2 & cs & -c^2 & -cs \\ cs & s^2 & -cs & -s^2 \\ -c^2 & -cs & c^2 & cs \\ -cs & -s^2 & cs & s^2 \end{bmatrix} \tag{7}$$

By considering the bending stiffness:

$$[K]_{global-2} = \frac{EI}{L^3}\begin{bmatrix} 12s^2 & -12cs & -12s^2 & 12cs \\ -12cs & 12c^2 & 12cs & -12c^2 \\ -12s^2 & 12cs & 12s^2 & -12cs \\ 12cs & -12c^2 & -12cs & 12c^2 \end{bmatrix} \tag{8}$$

Therefore,

$$[K]_{global} = [K]_{global-1} + [K]_{global-2} \tag{9}$$

Relation between local and global force vectors:

$$\{f\}_{global} = [T]\{f\}_{local} \tag{10}$$

Where, $[T]=\begin{bmatrix} c & -s & 0 & 0 \\ s & c & 0 & 0 \\ 0 & 0 & c & -s \\ 0 & 0 & s & c \end{bmatrix}$

By combining Equations (6) – (10), Equations (3) – (5) transform to:

Element–1

$$\begin{bmatrix} \frac{EA_1}{L_1}c^2+\frac{12EI_1}{L_1^3}s^2 & \frac{EA_1}{L_1}cs-\frac{12EI_1}{L_1^3}cs & -\frac{EA_1}{L_1}c^2-\frac{12EI_1}{L_1^3}s^2 & -\frac{EA_1}{L_1}cs+\frac{12EI_1}{L_1^3}cs \\ \frac{EA_1}{L_1}cs-\frac{12EI_1}{L_1^3}cs & \frac{EA_1}{L_1}s^2+\frac{12EI_1}{L_1^3}c^2 & -\frac{EA_1}{L_1}cs+\frac{12EI_1}{L_1^3}cs & -\frac{EA_1}{L_1}s^2-\frac{12EI_1}{L_1^3}c^2 \\ -\frac{EA_1}{L_1}c^2-\frac{12EI_1}{L_1^3}s^2 & -\frac{EA_1}{L_1}cs+\frac{12EI_1}{L_1^3}cs & \frac{EA_1}{L_1}c^2+\frac{12EI_1}{L_1^3}s^2 & \frac{EA_1}{L_1}cs-\frac{12EI_1}{L_1^3}cs \\ -\frac{EA_1}{L_1}cs+\frac{12EI_1}{L_1^3}cs & -\frac{EA_1}{L_1}s^2-\frac{12EI_1}{L_1^3}c^2 & \frac{EA_1}{L_1}cs-\frac{12EI_1}{L_1^3}cs & \frac{EA_1}{L_1}s^2+\frac{12EI_1}{L_1^3}c^2 \end{bmatrix} \begin{Bmatrix} u_1 \\ v_1 \\ u_2 \\ v_2 \end{Bmatrix} \tag{11}$$

$$= \begin{Bmatrix} -\alpha\Delta TEA_1c \\ -\alpha\Delta TEA_1s \\ \alpha\Delta TEA_1c \\ \alpha\Delta TEA_1s \end{Bmatrix} + \begin{Bmatrix} R_u^1 \\ 0 \\ 0 \\ 0 \end{Bmatrix}$$

Element–2

$$\begin{bmatrix} \frac{EA_2}{L_2}c^2+\frac{12EI_2}{L_2^3}s^2 & \frac{EA_2}{L_2}cs-\frac{12EI_2}{L_2^3}cs & -\frac{EA_2}{L_2}c^2-\frac{12EI_2}{L_2^3}s^2 & -\frac{EA_2}{L_2}cs+\frac{12EI_2}{L_2^3}cs \\ \frac{EA_2}{L_2}cs-\frac{12EI_2}{L_2^3}cs & \frac{EA_2}{L_2}s^2+\frac{12EI_2}{L_2^3}c^2 & -\frac{EA_2}{L_2}cs+\frac{12EI_2}{L_2^3}cs & -\frac{EA_2}{L_2}s^2-\frac{12EI_2}{L_2^3}c^2 \\ -\frac{EA_2}{L_2}c^2-\frac{12EI_2}{L_2^3}s^2 & -\frac{EA_2}{L_2}cs+\frac{12EI_2}{L_2^3}cs & \frac{EA_2}{L_2}c^2+\frac{12EI_2}{L_2^3}s^2 & \frac{EA_2}{L_2}cs-\frac{12EI_2}{L_2^3}cs \\ -\frac{EA_2}{L_2}cs+\frac{12EI_2}{L_2^3}cs & -\frac{EA_2}{L_2}s^2-\frac{12EI_2}{L_2^3}c^2 & \frac{EA_2}{L_2}cs-\frac{12EI_2}{L_2^3}cs & \frac{EA_2}{L_2}s^2+\frac{12EI_2}{L_2^3}c^2 \end{bmatrix} \begin{Bmatrix} u_2 \\ v_2 \\ u_3 \\ v_3 \end{Bmatrix} \tag{12}$$

$$= \begin{Bmatrix} -\alpha\Delta TEA_2c \\ -\alpha\Delta TEA_2s \\ \alpha\Delta TEA_2c \\ \alpha\Delta TEA_2s \end{Bmatrix}$$

Element–3

$$\begin{bmatrix} \frac{EA_3}{L_3}c^2+\frac{12EI_3}{L_3^3}s^2 & \frac{EA_3}{L_3}cs-\frac{12EI_3}{L_3^3}cs & -\frac{EA_3}{L_3}c^2-\frac{12EI_3}{L_3^3}s^2 & -\frac{EA_3}{L_3}cs+\frac{12EI_3}{L_1^3}cs \\ \frac{EA_3}{L_3}cs-\frac{12EI_3}{L_3^3}cs & \frac{EA_3}{L_3}s^2+\frac{12EI_3}{L_3^3}c^2 & -\frac{EA_3}{L_3}cs+\frac{12EI_3}{L_3^3}cs & -\frac{EA_3}{L_3}s^2-\frac{12EI_3}{L_3^3}c^2 \\ -\frac{EA_3}{L_3}c^2-\frac{12EI_3}{L_3^3}s^2 & -\frac{EA_3}{L_3}cs+\frac{12EI_3}{L_3^3}cs & \frac{EA_3}{L_3}c^2+\frac{12EI_3}{L_3^3}s^2 & \frac{EA_3}{L_3}cs-\frac{12EI_3}{L_3^3}cs \\ -\frac{EA_3}{L_3}cs+\frac{12EI_3}{L_3^3}cs & -\frac{EA_3}{L_3}s^2-\frac{12EI_3}{L_3^3}c^2 & \frac{EA_3}{L_3}cs-\frac{12EI_3}{L_3^3}cs & \frac{EA_3}{L_3}s^2+\frac{12EI_3}{L_3^3}c^2 \end{bmatrix} \begin{Bmatrix} u_3 \\ v_3 \\ u_4 \\ v_4 \end{Bmatrix} \tag{13}$$

$$= \begin{Bmatrix} -\alpha\Delta TEA_3c \\ -\alpha\Delta TEA_3s \\ \alpha\Delta TEA_3c \\ \alpha\Delta TEA_3s \end{Bmatrix} + \begin{Bmatrix} 0 \\ 0 \\ R_u^4 \\ 0 \end{Bmatrix}$$

3. Assembly of the element matrices.

$$\begin{bmatrix}
\frac{EA_1}{L_1}c^2+\frac{12EI_1}{L_1^3}s^2 & \frac{EA_1}{L_1}cs-\frac{12EI_1}{L_1^3}cs & -\frac{EA_1}{L_1}c^2-\frac{12EI_1}{L_1^3}s^2 & -\frac{EA_1}{L_1}cs+\frac{12EI_1}{L_1^3}cs & 0 & 0 & 0 & 0 \\
\frac{EA_1}{L_1}cs-\frac{12EI_1}{L_1^3}cs & \frac{EA_1}{L_1}s^2+\frac{12EI_1}{L_1^3}c^2 & -\frac{EA_1}{L_1}cs+\frac{12EI_1}{L_1^3}cs & -\frac{EA_1}{L_1}s^2-\frac{12EI_1}{L_1^3}c^2 & 0 & 0 & 0 & 0 \\
-\frac{EA_1}{L_1}c^2-\frac{12EI_1}{L_1^3}s^2 & -\frac{EA_1}{L_1}cs+\frac{12EI_1}{L_1^3}cs & \left(\frac{EA_1}{L_1}c^2+\frac{12EI_1}{L_1^3}s^2\right)+\left(\frac{EA_2}{L_2}c^2+\frac{12EI_2}{L_2^3}s^2\right) & \left(\frac{EA_1}{L_1}cs-\frac{12EI_1}{L_1^3}cs\right)+\left(\frac{EA_2}{L_2}cs-\frac{12EI_2}{L_2^3}cs\right) & -\frac{EA_2}{L_2}c^2-\frac{12EI_2}{L_2^3}s^2 & -\frac{EA_2}{L_2}cs+\frac{12EI_2}{L_2^3}cs & 0 & 0 \\
-\frac{EA_1}{L_1}cs+\frac{12EI_1}{L_1^3}cs & -\frac{EA_1}{L_1}s^2-\frac{12EI_1}{L_1^3}c^2 & \left(\frac{EA_1}{L_1}cs-\frac{12EI_1}{L_1^3}cs\right)+\left(\frac{EA_2}{L_2}cs-\frac{12EI_2}{L_2^3}cs\right) & \left(\frac{EA_1}{L_1}s^2+\frac{12EI_1}{L_1^3}c^2\right)+(\frac{EA_2}{L_2}s^2+\frac{12EI_2}{L_2^3}c^2) & -\frac{EA_2}{L_2}cs+\frac{12EI_2}{L_2^3}cs & -\frac{EA_2}{L_2}s^2-\frac{12EI_2}{L_2^3}c^2 & 0 & 0 \\
0 & 0 & -\frac{EA_2}{L_2}c^2-\frac{6EI_2}{L_2^3}s^2 & -\frac{EA_2}{L_2}cs+\frac{12EI_2}{L_2^3}cs & \frac{EA_2}{L_2}c^2+\frac{12EI_2}{L_2^3}s^2+\frac{EA_3}{L_3}c^2+\frac{12EI_3}{L_3^3}s^2 & \frac{EA_2}{L_2}cs-\frac{12EI_2}{L_2^3}cs+\frac{EA_3}{L_3}cs-\frac{12EI_3}{L_3^3}cs & -\frac{EA_3}{L_3}c^2-\frac{12EI_3}{L_3^3}s^2 & -\frac{EA_3}{L_3}cs+\frac{12EI_3}{L_3^3}cs \\
0 & 0 & -\frac{EA_2}{L_2}cs+\frac{12EI_2}{L_2^3}cs & -\frac{EA_2}{L_2}s^2-\frac{12EI_2}{L_2^3}c^2 & \frac{EA_2}{L_2}cs-\frac{12EI_2}{L_2^3}cs+\frac{EA_3}{L_3}cs-\frac{12EI_3}{L_3^3}cs & \frac{EA_2}{L_2}s^2+\frac{12EI_2}{L_2^3}c^2+\frac{EA_3}{L_3}s^2+\frac{12EI_3}{L_3^3}c^2 & -\frac{EA_3}{L_3}cs+\frac{12EI_3}{L_3^3}cs & -\frac{EA_3}{L_3}s^2-\frac{12EI_3}{L_3^3}c^2 \\
0 & 0 & 0 & 0 & -\frac{EA_3}{L_3}c^2-\frac{12EI_3}{L_3^3}s^2 & -\frac{EA_3}{L_3}cs+\frac{12EI_3}{L_3^3}cs & \frac{EA_3}{L_3}c^2+\frac{12EI_3}{L_3^3}s^2 & \frac{EA_3}{L_3}cs-\frac{12EI_3}{L_3^3}cs \\
0 & 0 & 0 & 0 & -\frac{EA_3}{L_3}cs+\frac{12EI_3}{L_3^3}cs & -\frac{EA_3}{L_3}s^2-\frac{12EI_3}{L_3^3}c^2 & \frac{EA_3}{L_3}cs-\frac{12EI_3}{L_3^3}cs & \frac{EA_3}{L_3}s^2+\frac{12EI_3}{L_3^3}c^2
\end{bmatrix}$$

$$\begin{Bmatrix} u_1 \\ v_1 \\ u_2 \\ v_2 \\ u_3 \\ v_3 \\ u_4 \\ v_4 \end{Bmatrix} = \begin{Bmatrix} -\alpha\Delta TEA_1c \\ -\alpha\Delta TEA_1s \\ \alpha\Delta TEA_1c-\ \alpha\Delta TEA_2c \\ \alpha\Delta TEA_1s-\alpha\Delta TEA_2s \\ \alpha\Delta TEA_2c-\ \alpha\Delta TEA_3c \\ \alpha\Delta TEA_2s-\alpha\Delta TEA_3s \\ \alpha\Delta TEA_3c \\ \alpha\Delta TEA_3s \end{Bmatrix} + \begin{Bmatrix} R_u^1 \\ 0 \\ 0 \\ 0 \\ 0 \\ 0 \\ R_u^4 \\ 0 \end{Bmatrix} \tag{14}$$

4. Boundary conditions.

$u_1 = u_4 = 0$,

$v_1 = 0$,

5. Imposition of boundary conditions in the global matrix (14) to find the displacement at node 4, and the global matrix is simplified as follows:

$$\begin{bmatrix}
\frac{EA_1}{L_1}c^2+\frac{12EI_1}{L_1^3}s^2 & \frac{EA_1}{L_1}cs-\frac{12EI_1}{L_1^3}cs & -\frac{EA_1}{L_1}c^2-\frac{12EI_1}{L_1^3}s^2 & -\frac{EA_1}{L_1}cs+\frac{12EI_1}{L_1^3}cs & 0 & 0 & 0 & 0 \\
\frac{EA_1}{L_1}cs-\frac{12EI_1}{L_1^3}cs & \frac{EA_1}{L_1}s^2+\frac{12EI_1}{L_1^3}c^2 & -\frac{EA_1}{L_1}cs+\frac{12EI_1}{L_1^3}cs & -\frac{EA_1}{L_1}s^2-\frac{12EI_1}{L_1^3}c^2 & 0 & 0 & 0 & 0 \\
-\frac{EA_1}{L_1}c^2-\frac{12EI_1}{L_1^3}s^2 & -\frac{EA_1}{L_1}cs+\frac{12EI_1}{L_1^3}cs & \left(\frac{EA_1}{L_1}c^2+\frac{12EI_1}{L_1^3}s^2\right)+\left(\frac{EA_2}{L_2}c^2+\frac{12EI_2}{L_2^3}s^2\right) & \left(\frac{EA_1}{L_1}cs-\frac{12EI_1}{L_1^3}cs\right)+\left(\frac{EA_2}{L_2}cs-\frac{12EI_2}{L_2^3}cs\right) & -\frac{EA_2}{L_2}c^2-\frac{12EI_2}{L_2^3}s^2 & -\frac{EA_2}{L_2}cs+\frac{12EI_2}{L_2^3}cs & 0 & 0 \\
-\frac{EA_1}{L_1}cs+\frac{12EI_1}{L_1^3}cs & -\frac{EA_1}{L_1}s^2-\frac{12EI_1}{L_1^3}c^2 & \left(\frac{EA_1}{L_1}cs-\frac{12EI_1}{L_1^3}cs\right)+\left(\frac{EA_2}{L_2}cs-\frac{12EI_2}{L_2^3}cs\right) & \left(\frac{EA_1}{L_1}s^2+\frac{12EI_1}{L_1^3}c^2\right)+(\frac{EA_2}{L_2}s^2+\frac{12EI_2}{L_2^3}c^2) & -\frac{EA_2}{L_2}cs+\frac{12EI_2}{L_2^3}cs & -\frac{EA_2}{L_2}s^2-\frac{12EI_2}{L_2^3}c^2 & 0 & 0 \\
0 & 0 & -\frac{EA_2}{L_2}c^2-\frac{12EI_2}{L_2^3}s^2 & -\frac{EA_2}{L_2}cs+\frac{12EI_2}{L_2^3}cs & (\frac{EA_2}{L_2}c^2+\frac{12EI_2}{L_2^3}s^2)+(\frac{EA_3}{L_3}c^2+\frac{12EI_3}{L_3^3}s^2) & \left(\frac{EA_2}{L_2}cs-\frac{12EI_2}{L_2^3}cs\right)+\left(\frac{EA_3}{L_3}cs-\frac{12EI_3}{L_3^3}cs\right) & -\frac{EA_3}{L_3}c^2-\frac{12EI_3}{L_3^3}s^2 & -\frac{EA_3}{L_3}cs+\frac{12EI_3}{L_3^3}cs \\
0 & 0 & -\frac{EA_2}{L_2}cs+\frac{12EI_2}{L_2^3}cs & -\frac{EA_2}{L_2}s^2-\frac{12EI_2}{L_2^3}c^2 & \left(\frac{EA_2}{L_2}cs-\frac{12EI_2}{L_2^3}cs\right)+\left(\frac{EA_3}{L_3}cs-\frac{12EI_3}{L_3^3}cs\right) & (\frac{EA_2}{L_2}s^2+\frac{12EI_2}{L_2^3}c^2)+(\frac{EA_3}{L_3}s^2+\frac{12EI_3}{L_3^3}c^2) & -\frac{EA_3}{L_3}cs+\frac{12EI_3}{L_3^3}cs & -\frac{EA_3}{L_3}s^2-\frac{12EI_3}{L_3^3}c^2 \\
0 & 0 & 0 & 0 & -\frac{EA_3}{L_3}c^2-\frac{12EI_3}{L_3^3}s^2 & -\frac{EA_3}{L_3}cs+\frac{12EI_3}{L_3^3}cs & \frac{EA_3}{L_3}c^2+\frac{12EI_3}{L_3^3}s^2 & \frac{EA_3}{L_3}cs-\frac{12EI_3}{L_3^3}cs \\
0 & 0 & 0 & 0 & -\frac{EA_3}{L_3}cs+\frac{12EI_3}{L_3^3}cs & -\frac{EA_3}{L_3}s^2-\frac{12EI_3}{L_3^3}c^2 & \frac{EA_3}{L_3}cs-\frac{12EI_3}{L_3^3}cs & \frac{EA_3}{L_3}s^2+\frac{12EI_3}{L_3^3}c^2
\end{bmatrix}$$

$$\begin{Bmatrix} u_1^{\Delta T}=0 \\ v_1^{\Delta T}=0 \\ u_2^{\Delta T} \\ v_2^{\Delta T} \\ u_3^{\Delta T} \\ v_3^{\Delta T} \\ u_4^{\Delta T}=0 \\ v_4^{\Delta T} \end{Bmatrix} = \begin{Bmatrix} -\alpha\Delta TEA_1c \\ -\alpha\Delta TEA_1s \\ \alpha\Delta TEA_1c-\ \alpha\Delta TEA_2c \\ \alpha\Delta TEA_1s\ -\ \alpha\Delta TEA_2s \\ \alpha\Delta TEA_2c-\ \alpha\Delta TEA_3c \\ \alpha\Delta TEA_2s-\alpha\Delta TEA_3s \\ \alpha\Delta TEA_3c \\ \alpha\Delta TEA_3s \end{Bmatrix} \tag{15}$$

After imposing the boundary conditions in the assembly matrix (14), we achieved five simultaneous equations (i.e., obtained from removing the rows and columns corresponding to the variables equal to zero), and for the purpose of simplicity, we assigned the coefficients with a symbol as follows:

$$u_2^{\Delta T}\left[\left(\frac{EA_1}{L_1}c^2+\frac{12EI_1}{L_1^3}s^2\right)+\left(\frac{EA_2}{L_2}c^2+\frac{12EI_2}{L_2^3}s^2\right)\right]+v_2^{\Delta T}\left[\left(\frac{EA_1}{L_1}cs-\frac{12EI_1}{L_1^3}cs\right)+\left(\frac{EA_2}{L_2}cs-\frac{12EI_2}{L_2^3}cs\right)\right]+u_3^{\Delta T}\left(-\frac{EA_2}{L_2}c^2-\frac{12EI_2}{L_2^3}s^2\right)+v_3^{\Delta T}\left(-\frac{EA_2}{L_2}cs+\frac{12EI_2}{L_2^3}cs\right)=\alpha\Delta TEA_1c-\alpha\Delta TEA_2c \tag{16}$$

$$u_2^{\Delta T}(I+N)+v_2^{\Delta T}(F+K)+u_3^{\Delta T}(O)+v_3^{\Delta T}(L)=\alpha\Delta TEA_1c-\alpha\Delta TEA_2c \tag{16'}$$

$$u_2^{\Delta T}\left[\left(\frac{EA_1}{L_1}cs-\frac{12EI_1}{L_1^3}cs\right)+\left(\frac{EA_2}{L_2}cs-\frac{12EI_2}{L_2^3}cs\right)\right]+v_2^{\Delta T}\left[\left(\frac{EA_1}{L_1}s^2+\frac{12EI_1}{L_1^3}c^2\right)+\left(\frac{EA_2}{L_2}s^2+\frac{12EI_2}{L_2^3}c^2\right)\right]+u_3^{\Delta T}\left(-\frac{EA_2}{L_2}cs+\frac{12EI_2}{L_2^3}cs\right)+v_3^{\Delta T}\left(-\frac{EA_2}{L_2}s^2-\frac{12EI_2}{L_2^3}c^2\right)=\alpha\Delta TEA_1s-\alpha\Delta TEA_2s \tag{17}$$

$$u_2^{\Delta T}(F+K)+v_2^{\Delta T}(H+M)+u_3^{\Delta T}(L)+v_3^{\Delta T}(R)=\alpha\Delta TEA_1s-\alpha\Delta TEA_2s \tag{17'}$$

$$u_2^{\Delta T}\left(-\frac{EA_2}{L_2}c^2-\frac{12EI_2}{L_2^3}s^2\right)+v_2^{\Delta T}\left(-\frac{EA_2}{L_2}cs+\frac{12EI_2}{L_2^3}cs\right)+u_3^{\Delta T}\left[\left(\frac{EA_2}{L_2}c^2+\frac{12EI_2}{L_2^3}s^2\right)+\left(\frac{EA_3}{L_3}c^2+\frac{12EI_3}{L_3^3}s^2\right)\right]+v_3^{\Delta T}\left[\left(\frac{EA_2}{L_2}cs-\frac{12EI_2}{L_2^3}cs\right)+\left(\frac{EA_3}{L_3}cs-\frac{12EI_3}{L_3^3}cs\right)\right]+v_4^{\Delta T}\left(-\frac{EA_3}{L_3}cs+\frac{12EI_3}{L_3^3}cs\right)=\alpha\Delta TEA_2c-\alpha\Delta TEA_3c \tag{18}$$

$$u_2^{\Delta T}(O)+v_2^{\Delta T}(L)+u_3^{\Delta T}[N+D]+v_3^{\Delta T}[K+B]+v_4^{\Delta T}(A)=\alpha\Delta TEA_2c-\alpha\Delta TEA_3c \tag{18'}$$

$$\begin{aligned}&u_2^{\Delta T}\left(-\frac{EA_2}{L_2}cs+\frac{12EI_2}{L_2^3}cs\right)+v_2^{\Delta T}\left(-\frac{EA_2}{L_2}s^2-\frac{12EI_2}{L_2^3}c^2\right)+\\&u_3^{\Delta T}\left[\left(\frac{EA_2}{L_2}cs-\frac{12EI_2}{L_2^3}cs\right)+\left(\frac{EA_3}{L_3}cs-\frac{12EI_3}{L_3^3}cs\right)\right]+v_3^{\Delta T}\left[\left(\frac{EA_2}{L_2}s^2+\right.\right.\\&\left.\left.\frac{12EI_2}{L_2^3}c^2\right)+\left(\frac{EA_3}{L_3}s^2+\frac{12EI_3}{L_3^3}c^2\right)\right]+v_4^{\Delta T}\left(-\frac{EA_3}{L_3}s^2-\frac{12EI_3}{L_3^3}c^2\right)=\\&\alpha\Delta \mathrm{TEA}_2\mathrm{s}-\alpha\Delta \mathrm{TEA}_3\mathrm{s}\end{aligned}\tag{19}$$

$$\begin{aligned}&u_2^{\Delta T}(L)+v_2^{\Delta T}(R)+u_3^{\Delta T}[K+B]+v_3^{\Delta T}[M+C]+v_4^{\Delta T}(P)=\\&\alpha\Delta \mathrm{TEA}_2\mathrm{s}-\alpha\Delta \mathrm{TEA}_3\mathrm{s}\end{aligned}\tag{19'}$$

$$\begin{aligned}&u_3^{\Delta T}\left(-\frac{EA_3}{L_3}cs+\frac{12EI_3}{L_3^3}cs\right)+v_3^{\Delta T}\left(-\frac{EA_3}{L_3}s^2-\frac{12EI_3}{L_3^3}c^2\right)+\\&v_4^{\Delta T}\left(\frac{EA_3}{L_3}s^2+\frac{12EI_3}{L_3^3}c^2\right)=\alpha\Delta \mathrm{TEA}_3\mathrm{s}\end{aligned}\tag{20}$$

$$u_3^{\Delta T}(A)+v_3^{\Delta T}(P)+v_4^{\Delta T}(C)=\alpha\Delta \mathrm{TEA}_3\mathrm{s}\tag{20'}$$

Using Mathematica software, we could achieve the following closed-form expression:

$$\begin{aligned}v^{\Delta T}&=v_v^4\\&=\left(\frac{1}{C}\right)E\Bigg(\Bigg(\frac{(-A_1P+A_2P+A_3R)s}{R}+\frac{(A_1-A_2)(LP-AR)(cR-Ls)}{R(-L^2+OR)}-\frac{(AL(C+M)+(F+K)LP-(C+M)OP-A(F+K)R)\big((-L^2+OR)\big((A_1-A_2)(C(C+M)-P^2)+(-A_2C+A_3(C+P))R\big)s-(A_1-A_2)\big(C^2L+CLM-C(F+K)R+P(-LP+AR)\big)(cR-Ls)\big)}{(L^2-OR)\big((L(C+M)-(F+K)R)(-CL(C+M)+LP^2+C(F+K)R-APR)+(-L^2+OR)\big((C+M)(-C(C+M)+P^2)+CR^2\big)\big)}\Bigg)\Bigg)\\&+\Bigg(\Bigg(-AFL-AKL-DLP-LNP+FOP+KOP+ADR+ANR+\frac{(AL(C+M)+(F+K)LP-(C+M)OP-A(F+K)R)\big(\big((F+K)(-C(C+M)+P^2)+CLR\big)(-L^2+OR)-(-(F+K)L+(D+N)R)(-CL(C+M)+LP^2+C(F+K)R-APR)\big)}{(L(C+M)-(F+K)R)(-CL(C+M)+LP^2+C(F+K)R-APR)+(-L^2+OR)\big((C+M)(-C(C+M)+P^2)+CR^2\big)}\Bigg)\Bigg)\\&\frac{\left(\begin{array}{c}\big(-(-(C+M)(C(F+K)-AP)+CLR)(-L^2+OR)-(L(C+M)-(F+K)R)\big(-C(F+K)L+C(D+N)R+A(LP-AR)\big)\big)\big((-L^2+OR)\big((A_1-A_2)(C(C+M)-P^2)+\big(-A_2C+A_3(C+P)\big)R\big)s-(A_1-A_2)\big(C^2L+CLM-C(F+K)R+P(-LP+AR)\big)(cR-Ls)\big)\\+\big((L(C+M)-(F+K)R)(-CL(C+M)+LP^2+C(F+K)R-APR)+(-L^2+OR)\big((C+M)(-C(C+M)+P^2)+CR^2\big)\big)\big((-A_1+A_2)\big(C(F+K)L-C(D+N)R+A(-LP+AR)\big)(cR-Ls)+(-L^2+OR)\big((-A_1+A_2)(-C(F+K)+AP)s+R(-A_2cC+A_3cC+AA_3s)\big)\big)\end{array}\right)}{\left(\begin{array}{c}(L^2-OR)\big(\big((F+K)(-C(C+M)+P^2)+CLR\big)(-L^2+OR)-(-(F+K)L+(D+N)R)(-CL(C+M)+LP^2+C(F+K)R-APR)\big)\big(\big((C+M)(C(F+K)-AP)-CLR\big)(-L^2+OR)-(L(C+M)-(F+K)R)\big(-C(F+K)L+C(D+N)R+A(LP-AR)\big)\big)+\\\big((L(C+M)-(F+K)R)(-CL(C+M)+LP^2+C(F+K)R-APR)+(-L^2+OR)\big((C+M)(-C(C+M)+P^2)+CR^2\big)\big)\big((-C(F+K)^2+A(F+K)P+CJR)(-L^2+OR)-\big((F+K)L-(D+N)R\big)\big(C(F+K)L-C(D+N)R+A(-LP+AR)\big)\big)\end{array}\right)\alpha\Delta T}\end{aligned}\tag{21}$$

The response of two inclined beams subject to an external force (F) applied to the central shuttle along the *y*-direction, can be obtained similarly.

The equation can be obtained starting from the governing system of Equations (A14), where the thermal load on the right side is substituted with external force ($F/2$). Then, we obtain:

$$
v^{F_4} = v_v^4 \\
= \frac{\left(\frac{F_e}{2E}\left(\begin{gathered}
F^4+4F^3K+6F^2K^2+4FK^3+K^4-2F^2L^2-4FKL^2-2K^2L^2+L^4-2DF^2M-4DFKM-2DK^2M+2FJLM+2JKLM-2DL^2M+D^2M^2-2F^2MN-4FKMN-2K^2MN-2L^2MN+2DM^2N+M^2N^2+2FLMO+2KLMO-JM^2O \\
+C^2((D+N)^2-JO)+2C\left(JKL+D^2M-F^2N-2FKN-K^2N-L^2N+MN^2-D((F+K)^2+L^2-2MN)+KLO-JMO+FL(J+O)\right)+DF^2P-F^3P+F^2JP+2DFKP-3F^2KP+2FJKP+DK^2P-3FK^2P+JK^2P-K^3P-2DFLP+F^2LP \\
-FJLP-2DKLP+2FKLP-JKLP+K^2LP+DL^2P+FL^2P+KL^2P-L^3P-D^2MP+DFMP-FJMP+DKMP-JKMP+DLMP+F^2NP+2FKNP+K^2NP-2FLNP-2KLNP+L^2NP-2DMNP+FMNP+KMNP+LMNP-MN^2P-FLOP-KLOP \\
+L^2OP+JMOP-LMOP+C(-D^2-JK+D(F+K+L-2N)+KN+LN-N^2+F(-J+N)+JO-LO)P-\left(-4DKL-4KLN+K^2O+L^2O+F^2(J+O)-(D+N)(D-K-L+N)P-KOP+J(K^2+L^2-LP+OP)+F\left(2K(J+O)-OP+(D+N)(-4L+P)\right)\right)R \\
-((D+N)^2-JO)R^2-A\left(-(F+K-L)^2+(D-J+N)(C+M-R)\right)(C-F-K-L+M+R)
\end{gathered}\right)\right)}{\left(\begin{gathered}
C^3((D+N)^2-JO)+2C^2\left(JKL+D^2M-F^2N-2FKN-K^2N-L^2N+MN^2-D((F+K)^2+L^2-2MN)+KLO-JMO+FL(J+O)\right)+\left(-JKL-D^2M+F^2N+2FKN+K^2N+L^2N-MN^2+D((F+K)^2+L^2-2MN)-KLO+JMO-FL(J+O)\right)P^2+AP \\
\left(-2F^3-6F^2K-6FK^2-2K^3+2KL^2+2DKM-JLM+2KMN+2C(F+K)(D+N)+2F\left(L^2+M(D+N)\right)-LMO-CL(J+O)+JKR-2DLR-2LNR+KOR+F(J+O)R\right)+A^2\left(-(C+M)\left(-(F+K)^2-L^2+(C+M)(D+N)\right)-2(F+K)LR+(D+N)R^2\right)+C \\
\left(F^4+4F^3K+K^4+L^4-2DL^2M+D^2M^2-2L^2MN+2DM^2N+M^2N^2-JM^2O-D^2P^2-2DNP^2-N^2P^2+JOP^2-L^2(J+O)R-((D+N)^2-JO)R^2+2KL(M(J+O)+2(D+N)R)+F^2\left(6K^2-2\left(L^2+M(D+N)\right)-(J+O)R\right)-K^2\left(2\left(L^2+M(D+N)\right)+(J+O)R\right)\right. \\
\left.+2F\left(2K^3-2K\left(L^2+M(D+N)\right)+LM(J+O)+2L(D+N)R-K(J+O)R\right)\right)
\end{gathered}\right)}
\tag{22}
$$

The ratio $K_A = F/v^F$ represents the stiffness of the v-shaped thermal actuator beam. Therefore, the equation will be:

$$
K_A = \\
\frac{2mE\left(\begin{gathered}
C^3((D+N)^2-JO)+2C^2\left(JKL+D^2M-F^2N-2FKN-K^2N-L^2N+MN^2-D((F+K)^2+L^2-2MN)+KLO-JMO+FL(J+O)\right)+\left(-JKL-D^2M+F^2N+2FKN+K^2N+L^2N-MN^2+D((F+K)^2+L^2-2MN)-KLO+JMO-FL(J+O)\right)P^2+AP \\
\left(-2F^3-6F^2K-6FK^2-2K^3+2KL^2+2DKM-JLM+2KMN+2C(F+K)(D+N)+2F\left(L^2+M(D+N)\right)-LMO-CL(J+O)+JKR-2DLR-2LNR+KOR+F(J+O)R\right)+A^2\left(-(C+M)\left(-(F+K)^2-L^2+(C+M)(D+N)\right)-2(F+K)LR+(D+N)R^2\right)+C \\
\left(F^4+4F^3K+K^4+L^4-2DL^2M+D^2M^2-2L^2MN+2DM^2N+M^2N^2-JM^2O-D^2P^2-2DNP^2-N^2P^2+JOP^2-L^2(J+O)R-((D+N)^2-JO)R^2+2KL(M(J+O)+2(D+N)R)+F^2\left(6K^2-2\left(L^2+M(D+N)\right)-(J+O)R\right)-K^2\left(2\left(L^2+M(D+N)\right)+(J+O)R\right)\right. \\
\left.+2F\left(2K^3-2K\left(L^2+M(D+N)\right)+LM(J+O)+2L(D+N)R-K(J+O)R\right)\right)
\end{gathered}\right)}{\left(\begin{gathered}
F^4+4F^3K+6F^2K^2+4FK^3+K^4-2F^2L^2-4FKL^2-2K^2L^2+L^4-2DF^2M-4DFKM-2DK^2M+2FJLM+2JKLM-2DL^2M+D^2M^2-2F^2MN-4FKMN-2K^2MN-2L^2MN+2DM^2N+M^2N^2+2FLMO+2KLMO-JM^2O \\
+C^2((D+N)^2-JO)+2C(JKL+D^2M-F^2N-2FKN-K^2N-L^2N+MN^2-D((F+K)^2+L^2-2MN)+KLO-JMO+FL(J+O))+DF^2P-F^3P+F^2JP+2DFKP-3F^2KP+2FJKP+DK^2P-3FK^2P+JK^2P-K^3P-2DFLP+F^2LP \\
-FJLP-2DKLP+2FKLP-JKLP+K^2LP+DL^2P+FL^2P+KL^2P-L^3P-D^2MP+DFMP-FJMP+DKMP-JKMP+DLMP+F^2NP+2FKNP+K^2NP-2FLNP-2KLNP+L^2NP-2DMNP+FMNP+KMNP+LMNP-MN^2P-FLOP-KLOP \\
+L^2OP+JMOP-LMOP+C(-D^2-JK+D(F+K+L-2N)+KN+LN-N^2+F(-J+N)+JO-LO)P-\left(-4DKL-4KLN+K^2O+L^2O+F^2(J+O)-(D+N)(D-K-L+N)P-KOP+J(K^2+L^2-LP+OP)+F\left(2K(J+O)-OP+(D+N)(-4L+P)\right)\right)R \\
-((D+N)^2-JO)R^2-A(-(F+K-L)^2+(D-J+N)(C+M-R))(C-F-K-L+M+R)
\end{gathered}\right)}
\tag{23}
$$

where m is the number of thermal actuator beams.

Appendix – B – Analytical modeling of a C-shaped hinge rotating structure

By computing the derivative of the strain energy reported in equation (35) with respect to the F_A, it is possible to find the displacement at the beginning of the straight beam δ_A as a function of different geometrical parameters. In particular, the following equations ((B.1) to (B.4)), report δ_A/F_A as a function of the width of the straight and curved beams, radius of the curved beam, length of the straight beam and angle of the curved beam, respectively. These relationships together with the geometrical parameters reported in Table 7 were used to draw the plots reported in Figure 43.

$$
\begin{aligned}
&\frac{\delta_A}{F_A}(W) = \left(\frac{6}{hEW^3}\right)\Bigl[2\left(\frac{R(1+\cos\theta_1)}{x_s-(x_r+R\sin\theta_1)}\right)^2\left(\frac{x^3}{3}\right) + 11.0104\left(\frac{R(1+\cos\theta_1)}{x_s-(x_r+R\sin\theta_1)}\right)\left(\frac{1}{x_s-(x_r+R\sin\theta_1)}\right)\left(\frac{x^3}{3}\right) - \\
&11.0104\left(\frac{R(1+\cos\theta_1)}{x_s-(x_r+R\sin\theta_1)}\right)\left(\frac{x^2}{2}\right) + 15.1536\left(\frac{1}{x_s-(x_r+R\sin\theta_1)}\right)^2\left(\frac{x^3}{3}\right) - \\
&30.3072\left(\frac{1}{x_s-(x_r+R\sin\theta_1)}\right)\left(\frac{x^2}{2}\right) + 15.1536\,x\Bigr]_{x=0}^{x=x_s} + \left(\frac{6}{hEW^3}\right)\Bigl[11.0104\,R^2\alpha - \\
&11.0104\,R^2\sin\alpha - 5.5052\left(\frac{R(1+\cos\theta_1)}{x_s-(x_r+R\sin\theta_1)}\right)x_sR\alpha + 11.0104\left(\frac{R(1+\cos\theta_1)}{x_s-(x_r+R\sin\theta_1)}\right)R^2\cos\alpha + \\
&30.3072\left(\frac{1}{x_s-(x_r+R\sin\theta_1)}\right)R^2\cos\alpha - 30.3072\left(\frac{1}{x_s-(x_r+R\sin\theta_1)}\right)x_sR\alpha - 5.5052\,R\alpha - \\
&11.0104\left(\frac{1}{x_s-(x_r+R\sin\theta_1)}\right)x_sR^2\alpha + 11.0104\left(\frac{1}{x_s-(x_r+R\sin\theta_1)}\right)x_sR^2\sin\alpha + \\
&11.0104\left(\frac{R(1+\cos\theta_1)}{x_s-(x_r+R\sin\theta_1)}\right)\left(\frac{1}{x_s-(x_r+R\sin\theta_1)}\right){x_s}^2R\alpha - \\
&22.0208\left(\frac{R(1+\cos\theta_1)}{x_s-(x_r+R\sin\theta_1)}\right)\left(\frac{1}{x_s-(x_r+R\sin\theta_1)}\right)x_sR^2\cos\alpha - \\
&30.3072\left(\frac{1}{x_s-(x_r+R\sin\theta_1)}\right)^2x_sR^2\cos\alpha + 15.1536\left(\frac{1}{x_s-(x_r+R\sin\theta_1)}\right)^2{x_s}^2R\alpha + \\
&11.0104\left(\frac{1}{x_s-(x_r+R\sin\theta_1)}\right)R^3\cos\alpha + 11.0104\left(\frac{R(1+\cos\theta_1)}{x_s-(x_r+R\sin\theta_1)}\right)\left(\frac{1}{x_s-(x_r+R\sin\theta_1)}\right)R^3\Bigl(\frac{\alpha}{2} - \\
&\frac{\sin 2\alpha}{4}\Bigr) + 15.1536\left(\frac{1}{x_s-(x_r+R\sin\theta_1)}\right)^2R^3\Bigl(\frac{\alpha}{2} - \\
&\frac{\sin 2\alpha}{4}\Bigr) + 4\left(\frac{R(1+\cos\theta_1)}{x_s-(x_r+R\sin\theta_1)}\right)R^3\cos\alpha + 4\left(\frac{R(1+\cos\theta_1)}{x_s-(x_r+R\sin\theta_1)}\right)R^3\left(\frac{\sin^2\alpha}{2}\right) - 4\left(\frac{R(1+\cos\theta_1)}{x_s-(x_r+R\sin\theta_1)}\right)^2R^2x_s\cos\alpha + \\
&2\left(\frac{R(1+\cos\theta_1)}{x_s-(x_r+R\sin\theta_1)}\right)^2R^3\Bigl(\frac{\alpha}{2} - \\
&\frac{\sin 2\alpha}{4}\Bigr) - 4\left(\frac{R(1+\cos\theta_1)}{x_s-(x_r+R\sin\theta_1)}\right)R^2x_s\alpha + 4\left(\frac{R(1+\cos\theta_1)}{x_s-(x_r+R\sin\theta_1)}\right)R^2x_s\sin\alpha + 2\left(\frac{R(1+\cos\theta_1)}{x_s-(x_r+R\sin\theta_1)}\right)^2{x_s}^2R\alpha - \\
&5.5052\left(\frac{R(1+\cos\theta_1)}{x_s-(x_r+R\sin\theta_1)}\right)x_sR\alpha - 4R^3\sin\alpha + 2R^3\left(\frac{\alpha}{2}+\frac{\sin 2\alpha}{4}\right) + 2R^3\alpha\Bigr]_{\alpha=0°}^{\alpha=214.15°}
\end{aligned}
\tag{B.1}
$$

$$
\begin{aligned}
&\frac{\delta_A}{F_A}(R) = \left(\frac{1}{2EI}\right)\Bigl[2\left(\frac{R(1+\cos\theta_1)}{x_s-(x_r+R\sin\theta_1)}\right)^2\left(\frac{x^3}{3}\right) - 4(Y')\left(\frac{R(1+\cos\theta_1)}{x_s-(x_r+R\sin\theta_1)}\right)\left(\frac{1}{x_s-(x_r+R\sin\theta_1)}\right)\left(\frac{x^3}{3}\right) + \\
&4(Y')\left(\frac{R(1+\cos\theta_1)}{x_s-(x_r+R\sin\theta_1)}\right)\left(\frac{x^2}{2}\right) + 2(Y')^2\left(\frac{1}{x_s-(x_r+R\sin\theta_1)}\right)^2\left(\frac{x^3}{3}\right) - 4(Y')^2\left(\frac{1}{x_s-(x_r+R\sin\theta_1)}\right)\left(\frac{x^2}{2}\right) + \\
&2(Y')^2\,x\Bigr]_{x=0}^{x=x_s} + \left(\frac{1}{2EI}\right)\Bigl[-4\,(Y')R^2\alpha + 4\,(Y')\,R^2\sin\alpha + 2(Y')\left(\frac{R(1+\cos\theta_1)}{x_s-(x_r+R\sin\theta_1)}\right)x_sR\alpha - \\
&4\,(Y')\left(\frac{R(1+\cos\theta_1)}{x_s-(x_r+R\sin\theta_1)}\right)R^2\cos\alpha + 4(Y')^2\left(\frac{1}{x_s-(x_r+R\sin\theta_1)}\right)R^2\cos\alpha - \\
&4(Y')^2\left(\frac{1}{x_s-(x_r+R\sin\theta_1)}\right)x_sR\alpha + 2(Y')\,R\alpha + 4(Y')\left(\frac{1}{x_s-(x_r+R\sin\theta_1)}\right)x_sR^2\alpha - \\
&4\,(Y')\left(\frac{1}{x_s-(x_r+R\sin\theta_1)}\right)x_sR^2\sin\alpha - 4\,(Y')\left(\frac{R(1+\cos\theta_1)}{x_s-(x_r+R\sin\theta_1)}\right)\left(\frac{1}{x_s-(x_r+R\sin\theta_1)}\right){x_s}^2R\alpha + \\
&8\,(Y')\left(\frac{R(1+\cos\theta_1)}{x_s-(x_r+R\sin\theta_1)}\right)\left(\frac{1}{x_s-(x_r+R\sin\theta_1)}\right)x_sR^2\cos\alpha - 4(Y')^2\left(\frac{1}{x_s-(x_r+R\sin\theta_1)}\right)^2x_sR^2\cos\alpha + \\
&2(Y')^2\left(\frac{1}{x_s-(x_r+R\sin\theta_1)}\right)^2{x_s}^2R\alpha - 4\,(Y')\left(\frac{1}{x_s-(x_r+R\sin\theta_1)}\right)R^3\cos\alpha - \\
&4\,(Y')\left(\frac{R(1+\cos\theta_1)}{x_s-(x_r+R\sin\theta_1)}\right)\left(\frac{1}{x_s-(x_r+R\sin\theta_1)}\right)R^3\left(\frac{\alpha}{2}-\frac{\sin 2\alpha}{4}\right) + 2(Y')^2\left(\frac{1}{x_s-(x_r+R\sin\theta_1)}\right)^2R^3\Bigl(\frac{\alpha}{2} - \\
&\frac{\sin 2\alpha}{4}\Bigr) + 4\left(\frac{R(1+\cos\theta_1)}{x_s-(x_r+R\sin\theta_1)}\right)R^3\cos\alpha + 4\left(\frac{R(1+\cos\theta_1)}{x_s-(x_r+R\sin\theta_1)}\right)R^3\left(\frac{\sin^2\alpha}{2}\right) - 4\left(\frac{R(1+\cos\theta_1)}{x_s-(x_r+R\sin\theta_1)}\right)^2R^2x_s\cos\alpha + \\
&2\left(\frac{R(1+\cos\theta_1)}{x_s-(x_r+R\sin\theta_1)}\right)^2R^3\Bigl(\frac{\alpha}{2} - \\
&\frac{\sin 2\alpha}{4}\Bigr) - 4\left(\frac{R(1+\cos\theta_1)}{x_s-(x_r+R\sin\theta_1)}\right)R^2x_s\alpha + 4\left(\frac{R(1+\cos\theta_1)}{x_s-(x_r+R\sin\theta_1)}\right)R^2x_s\sin\alpha + 2\left(\frac{R(1+\cos\theta_1)}{x_s-(x_r+R\sin\theta_1)}\right)^2{x_s}^2R\alpha + \\
&2(Y')\left(\frac{R(1+\cos\theta_1)}{x_s-(x_r+R\sin\theta_1)}\right)x_sR\alpha - 4R^3\sin\alpha + 2R^3\left(\frac{\alpha}{2}+\frac{\sin 2\alpha}{4}\right) + 2R^3\alpha\Bigr]_{\alpha=0°}^{\alpha=214.15°}
\end{aligned}
\tag{B.2}
$$

$$
\begin{aligned}
&\frac{\delta_A}{F_A}(x) = \left(\frac{1}{2EI}\right)\Big[2\left(\frac{R(1+\cos\theta_1)}{x-(x_r+R\ \sin\theta_1)}\right)^2\left(\frac{x^3}{3}\right) - 4(Y')\left(\frac{R(1+\cos\theta_1)}{x-(x_r+R\ \sin\theta_1)}\right)\left(\frac{1}{x-(x_r+R\ \sin\theta_1)}\right)\left(\frac{x^3}{3}\right) + \\
&4(Y')\left(\frac{R(1+\cos\theta_1)}{x-(x_r+R\ \sin\theta_1)}\right)\left(\frac{x^2}{2}\right) + 2(Y')^2\left(\frac{1}{x-(x_r+R\ \sin\theta_1)}\right)^2\left(\frac{x^3}{3}\right) - 4(Y')^2\left(\frac{1}{x-(x_r+R\ \sin\theta_1)}\right)\left(\frac{x^2}{2}\right) + \\
&2(Y')^2\,x\Big]_0^x + \left(\frac{1}{2EI}\right)\Big[- 4\,(Y')R^2\alpha + 4\,(Y')\,R^2\sin\alpha + 2(Y')\left(\frac{R(1+\cos\theta_1)}{x-(x_r+R\ \sin\theta_1)}\right)xR\alpha - \\
&4\,(Y')\left(\frac{R(1+\cos\theta_1)}{x-(x_r+R\ \sin\theta_1)}\right)R^2\cos\alpha + 4(Y')^2\left(\frac{1}{x-(x_r+R\ \sin\theta_1)}\right)R^2\cos\alpha - \\
&4(Y')^2\left(\frac{1}{x-(x_r+R\ \sin\theta_1)}\right)xR\alpha + 2(Y')\,R\alpha + 4(Y')\left(\frac{1}{x-(x_r+R\ \sin\theta_1)}\right)xR^2\alpha - \\
&4\,(Y')\left(\frac{1}{x-(x_r+R\ \sin\theta_1)}\right)xR^2\sin\alpha - 4\,(Y')\left(\frac{R(1+\cos\theta_1)}{x-(x_r+R\ \sin\theta_1)}\right)\left(\frac{1}{x-(x_r+R\ \sin\theta_1)}\right)x^2R\alpha + \\
&8\,(Y')\left(\frac{R(1+\cos\theta_1)}{x-(x_r+R\ \sin\theta_1)}\right)\left(\frac{1}{x-(x_r+R\ \sin\theta_1)}\right)xR^2\cos\alpha - 4(Y')^2\left(\frac{1}{x-(x_r+R\ \sin\theta_1)}\right)^2 xR^2\cos\alpha + \\
&2(Y')^2\left(\frac{1}{x-(x_r+R\ \sin\theta_1)}\right)^2 x^2R\alpha - 4\,(Y')\left(\frac{1}{x-(x_r+R\ \sin\theta_1)}\right)R^3\cos\alpha - \\
&4\,(Y')\left(\frac{R(1+\cos\theta_1)}{x-(x_r+R\ \sin\theta_1)}\right)\left(\frac{1}{x-(x_r+R\ \sin\theta_1)}\right)R^3\left(\frac{\alpha}{2}-\frac{\sin 2\alpha}{4}\right) + 2(Y')^2\left(\frac{1}{x-(x_r+R\ \sin\theta_1)}\right)^2 R^3\Big(\frac{\alpha}{2} - \\
&\frac{\sin 2\alpha}{4}\Big) + 4\left(\frac{R(1+\cos\theta_1)}{x-(x_r+R\ \sin\theta_1)}\right)R^3\cos\alpha + 4\left(\frac{R(1+\cos\theta_1)}{x-(x_r+R\ \sin\theta_1)}\right)R^3\left(\frac{\sin^2\alpha}{2}\right) - 4\left(\frac{R(1+\cos\theta_1)}{x-(x_r+R\ \sin\theta_1)}\right)^2 R^2x\cos\alpha + \\
&2\left(\frac{R(1+\cos\theta_1)}{x-(x_r+R\ \sin\theta_1)}\right)^2 R^3\Big(\frac{\alpha}{2} - \\
&\frac{\sin 2\alpha}{4}\Big) - 4\left(\frac{R(1+\cos\theta_1)}{x-(x_r+R\ \sin\theta_1)}\right)R^2x\alpha + 4\left(\frac{R(1+\cos\theta_1)}{x-(x_r+R\ \sin\theta_1)}\right)R^2x\sin\alpha + 2\left(\frac{R(1+\cos\theta_1)}{x-(x_r+R\ \sin\theta_1)}\right)^2 x^2R\alpha + \\
&2(Y')\left(\frac{R(1+\cos\theta_1)}{x-(x_r+R\ \sin\theta_1)}\right)xR\alpha - 4R^3\sin\alpha + 2R^3\left(\frac{\alpha}{2}+\frac{\sin 2\alpha}{4}\right) + 2R^3\alpha\Big]_{\alpha=0^\circ}^{\alpha=214.15^\circ}
\end{aligned}
\tag{B.3}
$$

$$
\begin{aligned}
&\frac{\delta_A}{F_A}(\theta_1) = \left(\frac{1}{2EI}\right)\Big[2\left(\frac{R(1+\cos\theta_1)}{x_s-(x_r+R\ \sin\theta_1)}\right)^2\left(\frac{x^3}{3}\right) - 4(Y')\left(\frac{R(1+\cos\theta_1)}{x_s-(x_r+R\ \sin\theta_1)}\right)\left(\frac{1}{x_s-(x_r+R\ \sin\theta_1)}\right)\left(\frac{x^3}{3}\right) + \\
&4(Y')\left(\frac{R(1+\cos\theta_1)}{x_s-(x_r+R\ \sin\theta_1)}\right)\left(\frac{x^2}{2}\right) + 2(Y')^2\left(\frac{1}{x_s-(x_r+R\ \sin\theta_1)}\right)^2\left(\frac{x^3}{3}\right) - 4(Y')^2\left(\frac{1}{x_s-(x_r+R\ \sin\theta_1)}\right)\left(\frac{x^2}{2}\right) + \\
&2(Y')^2\,x\Big]_{x=0}^{x=x_s} + \left(\frac{1}{2EI}\right)\Big[- 4\,(Y')R^2\alpha + 4\,(Y')\,R^2\sin\alpha + 2(Y')\left(\frac{R(1+\cos\theta_1)}{x_s-(x_r+R\ \sin\theta_1)}\right)x_sR\alpha - \\
&4\,(Y')\left(\frac{R(1+\cos\theta_1)}{x_s-(x_r+R\ \sin\theta_1)}\right)R^2\cos\alpha + 4(Y')^2\left(\frac{1}{x_s-(x_r+R\ \sin\theta_1)}\right)R^2\cos\alpha - \\
&4(Y')^2\left(\frac{1}{x_s-(x_r+R\ \sin\theta_1)}\right)x_sR\alpha + 2(Y')\,R\alpha + 4(Y')\left(\frac{1}{x_s-(x_r+R\ \sin\theta_1)}\right)x_sR^2\alpha - \\
&4\,(Y')\left(\frac{1}{x_s-(x_r+R\ \sin\theta_1)}\right)x_sR^2\sin\alpha - 4\,(Y')\left(\frac{R(1+\cos\theta_1)}{x_s-(x_r+R\ \sin\theta_1)}\right)\left(\frac{1}{x_s-(x_r+R\ \sin\theta_1)}\right){x_s}^2R\alpha + \\
&8\,(Y')\left(\frac{R(1+\cos\theta_1)}{x_s-(x_r+R\ \sin\theta_1)}\right)\left(\frac{1}{x_s-(x_r+R\ \sin\theta_1)}\right)x_sR^2\cos\alpha - 4(Y')^2\left(\frac{1}{x_s-(x_r+R\ \sin\theta_1)}\right)^2 x_sR^2\cos\alpha + \\
&2(Y')^2\left(\frac{1}{x_s-(x_r+R\ \sin\theta_1)}\right)^2 {x_s}^2R\alpha - 4\,(Y')\left(\frac{1}{x_s-(x_r+R\ \sin\theta_1)}\right)R^3\cos\alpha - \\
&4\,(Y')\left(\frac{R(1+\cos\theta_1)}{x_s-(x_r+R\ \sin\theta_1)}\right)\left(\frac{1}{x_s-(x_r+R\ \sin\theta_1)}\right)R^3\left(\frac{\alpha}{2}-\frac{\sin 2\alpha}{4}\right) + 2(Y')^2\left(\frac{1}{x_s-(x_r+R\ \sin\theta_1)}\right)^2 R^3\Big(\frac{\alpha}{2} - \\
&\frac{\sin 2\alpha}{4}\Big) + 4\left(\frac{R(1+\cos\theta_1)}{x_s-(x_r+R\ \sin\theta_1)}\right)R^3\cos\alpha + 4\left(\frac{R(1+\cos\theta_1)}{x_s-(x_r+R\ \sin\theta_1)}\right)R^3\left(\frac{\sin^2\alpha}{2}\right) - 4\left(\frac{R(1+\cos\theta_1)}{x_s-(x_r+R\ \sin\theta_1)}\right)^2 R^2x_s\cos\alpha + \\
&2\left(\frac{R(1+\cos\theta_1)}{x_s-(x_r+R\ \sin\theta_1)}\right)^2 R^3\Big(\frac{\alpha}{2} - \\
&\frac{\sin 2\alpha}{4}\Big) - 4\left(\frac{R(1+\cos\theta_1)}{x_s-(x_r+R\ \sin\theta_1)}\right)R^2x_s\alpha + 4\left(\frac{R(1+\cos\theta_1)}{x_s-(x_r+R\ \sin\theta_1)}\right)R^2x_s\sin\alpha + 2\left(\frac{R(1+\cos\theta_1)}{x_s-(x_r+R\ \sin\theta_1)}\right)^2 {x_s}^2R\alpha + \\
&2(Y')\left(\frac{R(1+\cos\theta_1)}{x_s-(x_r+R\ \sin\theta_1)}\right)x_sR\alpha - 4R^3\sin\alpha + 2R^3\left(\frac{\alpha}{2}+\frac{\sin 2\alpha}{4}\right) + 2R^3\alpha\Big]_{0^\circ}^{\pi+\theta_1}
\end{aligned}
\tag{B.4}
$$

Where Y' is the moment at the slider, normalized by the force, F_A.

Bibliography

[1] P. Pan, W. Wang, C. Ru, Y. Sun, and X. Liu, “MEMS-based platforms for mechanical manipulation and characterization of cells,” *J. Micromechanics Microengineering*, vol. 27, no. 12, 2017, doi: 10.1088/1361-6439/aa8f1d.

[2] T. Luo, L. Fan, R. Zhu, and D. Sun, “Microfluidic single-cell manipulation and analysis: Methods and applications,” *Micromachines*, vol. 10, no. 2, Feb. 2019, doi: 10.3390/mi10020104.

[3] T. Tang *et al.*, “Rotation of Biological Cells: Fundamentals and Applications,” *Engineering*, vol. 10, pp. 110–126, 2022, doi: 10.1016/j.eng.2020.07.031.

[4] J. Barklie, P. Goodrich, A. Mckeown, and C. Hardacre, “Design of a novel magnetic platform for cell manipulation,” *J. Micromech. Microeng.* ., vol. 28, no. 2, 2018.

[5] M. Boudaoud and S. Regnier, “An overview on gripping force measurement at the micro and nano-scales using two-fingered microrobotic systems,” *Int. J. Adv. Robot. Syst.*, vol. 11, no. 1, 2014, doi: 10.5772/57571.

[6] J. P. Desai, A. Pillarisetti, and A. D. Brooks, “Engineering approaches to biomanipulation,” *Annu. Rev. Biomed. Eng.*, vol. 9, pp. 35–53, 2007, doi: 10.1146/annurev.bioeng.9.060906.151940.

[7] H. Yun, K. Kim, and W. G. Lee, “Cell manipulation in microfluidics,” *Biofabrication*, vol. 5, no. 2, 2013, doi: 10.1088/1758-5082/5/2/022001.

[8] S. Zhang, Y. Wang, P. Onck, and J. den Toonder, “A concise review of microfluidic particle manipulation methods,” *Microfluid. Nanofluidics*, vol. 24, no. 4, pp. 1–20, 2020, doi: 10.1007/s10404-020-2328-5.

[9] J. S. Kwon and J. H. Oh, “Microfluidic technology for cell manipulation,” *Appl. Sci.*, vol. 8, no. 6, 2018, doi: 10.3390/app8060992.

[10] E. Vuille-Dit-Bille *et al.*, “Tools for manipulation and positioning of microtissues,” *Lab Chip*, vol. 22, no. 21, pp. 4043–4066, 2022, doi: 10.1039/d2lc00559j.

[11] P. Faraday, T. Watch, M. Jb *et al*, *An Introduction to MEMS (Micro-electromechanical Systems) MEMS has been identified as one of the most promising technologies for PRIME Faraday Partnership*, vol. 2, no. 4, pp. 158-165, 2011.

[12] M. Jb, “A Review Study on MEMS (Micro Electro Mechanical Systems),” vol. 3, no. 8, pp. 748–753, 2016.

[13] S. Karumuri, Y. Srinivas, J. Sekhar, and K. Sravani, “Review on break through MEMS Technology,” *Arch. Phys. Res.*, vol. 2, no. 4, pp. 158–165, 2011.

[14] C. H. Liu *et al.*, “Adaptable and integrated packaging platform for MEMS-based combo sensors utilizing innovative wafer-level packaging technologies,” *Proc. - Electron. Components Technol. Conf.*, no. May 2013, pp. 1675–1681, 2013, doi: 10.1109/ECTC.2013.6575798.

[15] N. Chronis and L. P. Lee, “Electrothermally activated SU-8 microgripper for single cell manipulation in solution,” *J. Microelectromechanical Syst.*, vol. 14, no. 4, pp. 857–863, 2005, doi: 10.1109/JMEMS.2005.845445.

[16] Q. Xu, “Design, Fabrication, and Testing of an MEMS Microgripper with Dual-Axis Force Sensor,” *IEEE Sens. J.*, vol. 15, no. 10, pp. 6017–6026, 2015, doi: 10.1109/JSEN.2015.2453013.

[17] C. Clevy, A. Hubert, and N. Chaillet, “Micromanipulation and micro-assembly systems,” *Int. Adv. Robot. Program. 2006*, no. October 2006, pp. 2–7, 2006, [Online]. Available: http://scholar.google.com/scholar?hl=en&btnG=Search&q=intitle:Micromanipulation+and+Micro-Assembly+Systems#0.

[18] N. Dechev, W. L. Cleghorn, and J. K. Mills, “Microassembly of 3-D microstructures using a compliant, passive microgripper,” *J. Microelectromechanical Syst.*, vol. 13, no. 2, pp. 176–189, 2004, doi: 10.1109/JMEMS.2004.825311.

[19] S. Iamoni and A. Somà, “Design of an electro-thermally actuated cell microgripper,” *Microsyst. Technol.*, vol. 20, no. 4–5, pp. 869–877, 2014, doi: 10.1007/s00542-013-2065-8.

[20] M. Verotti, A. Dochshanov, and N. P. Belfiore, “A Comprehensive Survey on Microgrippers Design: Mechanical Structure,” *J. Mech. Des. Trans. ASME*, vol. 139, no. 6, pp. 1–46, 2017, doi: 10.1115/1.4036351.

[21] S. Yang and Q. Xu, “A review on actuation and sensing techniques for MEMS-based microgrippers,” *J. Micro-Bio Robot.*, vol. 13, no. 1–4, pp. 1–14, 2017, doi: 10.1007/s12213-017-0098-2.

[22] A. Dochshanov, M. Verotti, and N. P. Belfiore, “A Comprehensive Survey on Microgrippers Design: Operational Strategy,” *J. Mech. Des. Trans. ASME*, vol. 139, no. 7, 2017, doi: 10.1115/1.4036352.

[23] B. Zhu, X. Zhang, M. Liu, Q. Chen, and H. Li, “Topological and Shape Optimization of Flexure Hinges for Designing Compliant Mechanisms Using the Level Set Method,” *Chinese J. Mech. Eng. (English Ed.*, vol. 32, no. 1, 2019, doi: 10.1186/s10033-019-0332-z.

[24] V. Kolate, P. D. Darade, and N. Jadhav, “A Review Paper on Compound Displacement Amplification Mechanism,” vol. 7, no. 3, pp. 556–563, 2022.

[25] M. R. A. Raghavendra, A. S. Kumar, and B. N. Jagdish, “Design and analysis of flexure-hinge parameter in microgripper,” *Int. J. Adv. Manuf. Technol.*, vol. 49, no. 9–12, pp. 1185–1193, 2010, doi: 10.1007/s00170-009-2478-9.

[26] M. Ling, L. L. Howell, J. Cao, and G. Chen, “Kinetostatic and dynamic modeling of flexure-based compliant mechanisms: A survey,” *Appl. Mech. Rev.*, vol. 72, no. 3, 2020, doi: 10.1115/1.4045679.

[27] F. Chen, Q. Zhang, Y. Gao, and W. Dong, “A review on the flexure-based displacement amplification mechanisms,” *IEEE Access*, vol. 8, pp. 205919–205937, 2020, doi: 10.1109/ACCESS.2020.3037827.

[28] D. M. Bhoge and S. P. Deshmukh, “Comparison of Flexural Joints Used in Precision Scanning Mechanism Using FEA Tool,” *Int. Eng. Res. J.*, vol. 2, no. 2, pp. 197–204, 1961, [Online]. Available: www.ierjournal.org.

[29] E. A. G. Peeters, *Biomechanics of single cells under compression*, vol. 1, no. 2004. 2004.

[30] E. A. G. Peeters, C. W. J. Oomens, C. V. C. Bouten, D. L. Bader, and F. P. T. Baaijens, “Mechanical and failure properties of single attached cells under compression,” *J. Biomech.*, vol. 38, no. 8, pp. 1685–1693, 2005, doi: 10.1016/j.jbiomech.2004.07.018.

[31] Q. Xu, *Micromachines for biological micromanipulation*. 2018.

[32] L. Miao, Z. Dong, and H. Chan, “Displacement measurement of a thermally actuated polymer micro robotic gripper using the optical focus method,” *Proc. World Congr. Intell. Control Autom.*, vol. 5, pp. 3800–3804, 2004, doi: 10.1109/wcica.2004.1342198.

[33] S. S. S. Zadeh, V. Egan, and P. Walsh, “Real-Time Measurement Technique for Slug Flow Characterisation,” *J. Fluid Flow, Heat Mass Transf.*, vol. 9, pp. 191–199, 2022, doi: 10.11159/jffhmt.2022.023.

[34] K. Han, S. H. Lee, W. Moon, and J. S. Park, “Fabrication of the micro-gripper with a force sensor for manipulating a cell,” *2006 SICE-ICASE Int. Jt. Conf.*, pp. 5833–5836, 2006, doi: 10.1109/SICE.2006.315250.

[35] S. Yang and Q. Xu, “Design and simulation a MEMS microgripper with integrated electrothermal actuator and force sensor,” *ICARM 2016 - 2016 Int. Conf. Adv. Robot. Mechatronics*, pp. 271–276, 2016, doi: 10.1109/ICARM.2016.7606931.

[36] T. Chen, L. Chen, L. Sun, and X. Li, “Design and fabrication of a four-arm-structure MEMS gripper,” *IEEE Trans. Ind. Electron.*, vol. 56, no. 4, pp. 996–1004, 2009, doi: 10.1109/TIE.2008.2005147.

[37] J. Park and W. Moon, “A hybrid-type micro-gripper with an integrated force sensor,” *Microsyst. Technol.*, vol. 9, no. 8, pp. 511–519, 2003, doi: 10.1007/s00542-002-0267-6.

[38] F. Arai, D. Andou, Y. Nonoda, T. Fukuda, H. Iwata, and K. Itoigawa, “Integrated microendeffector for micromanipulation,” *IEEE/ASME Trans. Mechatronics*, vol. 3, no. 1, pp. 17–23, 1998, doi: 10.1109/3516.662864.

[39] D. H. Kim, M. G. Lee, B. Kim, and Y. Sun, “A superelastic alloy microgripper with embedded electromagnetic actuators and piezoelectric force sensors: A numerical and experimental study,” *Smart Mater. Struct.*, vol. 14, no. 6, pp. 1265–1272, 2005, doi: 10.1088/0964-1726/14/6/019.

[40] S. Shuib, M. I. Z. Ridzwan, and A. H. Kadarman, “Methodology of compliant mechanisms and its current developments in applications: A review,” *Am. J. Appl. Sci.*, vol. 4, no. 3, pp. 160–167, 2007, doi: 10.3844/ajassp.2007.160.167.

[41] L. B. Tang, Y. H. Chen, and X. J. He, “Multi-material compliant mechanism design and haptic evaluation,” *Virtual Phys. Prototyp.*, vol. 2, no. 3, pp. 155–160, 2007, doi: 10.1080/17452750701691831.

[42] A. MilojeviĆ, N. D. PavloviĆ, M. MiloševiĆ, and Miša TomiĆ, “New Software for Synthesis of Compliant Mechanisms New Software for Synthesis of Compliant Mechanisms,” *Mech. Eng. XXI century*, no. December, 2013.

[43] S. P. Jagtap, B. B. Deshmukh, and S. Pardeshi, “Applications of compliant mechanism in today’s world - A review,” *J. Phys. Conf. Ser.*, vol. 1969, no. 1, 2021, doi: 10.1088/1742-6596/1969/1/012013.

[44] Z. Lyu and Q. Xu, “Recent design and development of piezoelectric-actuated compliant microgrippers: A review,” *Sensors Actuators A Phys.*, vol. 331, p. 113002, 2021, doi: 10.1016/j.sna.2021.113002.

[45] Q. XING and Y. GE, “Parametric study of a novel asymmetric micro-gripper mechanism,” *J. Adv. Mech. Des. Syst. Manuf.*, vol. 9, no. 5, pp. JAMDSM0075–JAMDSM0075, 2015, doi: 10.1299/jamdsm.2015jamdsm0075.

[46] D. H. Wang, Q. Yang, and H. M. Dong, “A monolithic compliant piezoelectric-driven microgripper: Design, modeling, and testing,” *IEEE/ASME Trans. Mechatronics*, vol. 18, no. 1, pp. 138–147, 2013, doi: 10.1109/TMECH.2011.2163200.

[47] K. Lu, J. Zhang, W. Chen, J. Jiang, and W. Chen, “A monolithic microgripper with high efficiency and high accuracy for optical fiber assembly,” *Proc. 2014 9th IEEE Conf. Ind. Electron. Appl. ICIEA 2014*, pp. 1942–1947, 2014, doi: 10.1109/ICIEA.2014.6931486.

[48] Q. Shi, Z. Yu, H. Wang, T. Sun, Q. Huang, and T. Fukuda, “Development of a Highly Compact Microgripper Capable of Online Calibration for Multisized Microobject Manipulation,” *IEEE Trans. Nanotechnol.*, vol. 17, no. 4, pp. 657–661, 2018, doi: 10.1109/TNANO.2018.2793883.

[49] M. Verotti, R. Crescenzi, M. Balucani, and N. P. Belfiore, “MEMS-based conjugate surfaces flexure hinge,” *J. Mech. Des. Trans. ASME*, vol. 137, no. 1, pp. 1–10, 2015, doi: 10.1115/1.4028791.

[50] R. Crescenzi, M. Balucani, and and N. P. Belfiore, “Operational characterization of CSFH MEMS-Technology based hinges,” *J. Micromech. Microeng.*, vol. 28, no. 5, pp. 0–21, 2018, doi 10.1088/1361-6439/aaaf31

[51] M. Verotti, A. Dochshanov, and N. P. Belfiore, “Compliance Synthesis of CSFH MEMS-Based Microgrippers,” *J. Mech. Des. Trans. ASME*, vol. 139, no. 2, Feb. 2017, doi: 10.1115/1.4035053.

[52] A. Rossi and N. P. Belfiore, “Modal analysis of a four-bar linkage MEMS microgripper with cooperative electrostatic actuation,” *Mater. Res. Proc.*, vol. 26, pp. 647–652, 2023, doi: 10.21741/9781644902431-104.

[53] A. S. Algamili *et al.*, “A Review of Actuation and Sensing Mechanisms in MEMS-Based Sensor Devices,” *Nanoscale Res. Lett.*, vol. 16, no. 1, 2021, doi: 10.1186/s11671-021-03481-7.

[54] A. Wicaksana and T. Rachman, “*MEMS Linear and Nonlinear Statics and Dynamics*,”, vol. 3, pp. 10-27, no. 1. 2018.

[55] I. Morkvenaite-Vilkonciene, V. Bucinskas, J. Subaciute-Zemaitiene, E. Sutinys, D. Virzonis, and A. Dzedzickis, “Development of Electrostatic Microactuators: 5-Year Progress in Modeling, Design, and Applications,” *Micromachines*, vol. 13, no. 8, 2022, doi: 10.3390/mi13081256.

[56] J. C. Chiou and Y. J. Lin, “A novel large displacement electrostatic actuator: Pre-stress comb-drive actuator,” *J. Micromechanics Microengineering*, vol. 15, no. 9, pp. 1641–1648, 2005, doi: 10.1088/0960-1317/15/9/005.

[57] J. Varona, E. Saenz, S. Fiscal-Woodhouse, and A. A. Hamoui, “Design and fabrication of a novel microgripper based on electrostatic actuation,” *Midwest Symp. Circuits Syst.*, pp. 827–832, 2009, doi: 10.1109/MWSCAS.2009.5235896.

[58] H. Demaghsi, H. Mirzajani, and H. B. Ghavifekr, “A novel electrostatic based Microgripper (Cellgripper) integrated with contact sensor and equipped with vibrating system to release particles actively,” *Microsyst. Technol.*, vol. 20, no. 12, pp. 2191–2202, 2014, doi: 10.1007/s00542-013-1989-3.

[59] R. Cecchi *et al.*, “Development of micro-grippers for tissue and cell manipulation with direct morphological comparison,” *Micromachines*, vol. 6, no. 11, pp. 1710–1728, 2015, doi: 10.3390/mi6111451.

[60] Z. Guo, Z. Lyu, and Q. Xu, “Design of a Piezoelectric-Driven Microgripper With Three Working Modes,” *IEEE/ASME Trans. Mechatronics*, vol. PP, pp. 1–11, 2023, doi: 10.1109/TMECH.2023.3276191.

[61] M. Cauchi, I. Grech, B. Mallia, P. Mollicone, and N. Sammut, “The effects of cold arm width and metal deposition on the performance of a U-beam electrothermal MEMS microgripper

for biomedical applications," *Micromachines*, vol. 10, no. 3, 2019, doi: 10.3390/mi10030167.

[62] P. Vargas-Chable, J. Mireles Jr-Garcia, S. F. Rodriguez-Fuentes, S. I. Valle-Morales, and M. Tecpoyotl-Torres, "Microgripper based on simple compliance configurations, improved by using parameterization," *Actuators*, vol. 9, no. 4, pp. 1–21, 2020, doi: 10.3390/act9040140.

[63] F. Chollet and H. Liu, *A (not so) short introduction to MEMS*. 2011.

[64] A. P. Force, S. System, C. K. M. Fung, I. Elhaj, W. J. Lil, and N. Xi, "Force Sensing System for Micro-," *Micro*, no. May, pp. 1489–1494, 2002.

[65] M. Garces-Schroder, T. Zimmermann, C. Siemers, M. Leester-Schadel, M. Bol, and A. Dietzel, "Shape Memory Alloy Actuators for Silicon Microgrippers," *J. Microelectromechanical Syst.*, vol. 28, no. 5, pp. 869–881, 2019, doi: 10.1109/JMEMS.2019.2936288.

[66] S. Yang and Q. Xu, "A review on actuation and sensing techniques for MEMS-based microgrippers," *J. Micro-Bio Robot.*, vol. 13, no. 1–4, 2017, doi: 10.1007/s12213-017-0098-2.

[67] L. A. Velosa-Moncada, L. A. Aguilera-Cortes, M. A. González-Palacios, J. P. Raskin, and A. L. Herrera-May, "Design of a novel MEMS microgripper with rotatory electrostatic comb-drive actuators for biomedical applications," *Sensors (Switzerland)*, vol. 18, no. 5, 2018, doi: 10.3390/s18051664.

[68] P. Schmitt and M. Hoffmann, "Engineering a Compliant Mechanical Amplifier for MEMS Sensor Applications," *J. Microelectromechanical Syst.*, vol. 29, no. 2, pp. 214–227, 2020, doi: 10.1109/JMEMS.2020.2965260.

[69] S. Iqbal and A. Malik, "A review on MEMS based micro displacement amplification mechanisms," *Sensors Actuators, A Phys.*, vol. 300, p. 111666, 2019, doi: 10.1016/j.sna.2019.111666.

[70] A. Bagolini, B. Margesin, A. Faes, G. Turco, and F. Giacomozzi, "Novel test structures for stress diagnosis in micromechanics," *Sensors Actuators, A Phys.*, vol. 115, no. 2-3 SPEC. ISS., pp. 494–500, 2004, doi: 10.1016/j.sna.2004.03.050.

[71] Y. Du, T. Li, W. Ji, Y. Jiang, and F. Li, "Compliance modeling of planar flexure-based mechanisms and its application to micro-motion stages," *Int. J. Adv. Robot. Syst.*, vol. 13, no. 4, pp. 1–11, 2016, doi: 10.1177/1729881416658173.

[72] B. Zhu, X. Zhang, and S. Fatikow, "Design of single-axis flexure hinges using continuum topology optimization method," *Sci. China Technol. Sci.*, vol. 57, no. 3, pp. 560–567, 2014, doi: 10.1007/s11431-013-5446-4.

[73] N. Lobontiu, "Introduction," *Syst. Dyn. Eng. Students*, pp. 1–22, 2018, doi: 10.1016/b978-0-12-804559-6.00001-4.

[74] J. Hricko, "Compliant Mechanisms for Motion / Force Amplifiers for Robotics Compliant Mechanisms for Motion / Force Amplifiers for Robotics," no. January, 2020, doi: 10.1007/978-3-030-19648-6.

[75] T. S. Yallew, N. P. Belfiore, A. Bagolini, and M. F. Pantano, "Performance Analysis of a CSFH-Based Microgripper: Analytical Modeling and Simulation," *Micromachines*, vol. 13, no. 9, 2022, doi: 10.3390/mi13091391.

[76] C. Potrich *et al.*, "Innovative silicon microgrippers for biomedical applications: Design, mechanical simulation and evaluation of protein fouling," *Actuators*, vol. 7, no. 2, 2018, doi: 10.3390/act7020012.

[77] A. Sharma, M. Kaur, D. Kumar, and K. Rangra, "MEMS Test Structures for Residual Stress Measurements," *Engineering*, no. February 2015, 2010.

[78] Z. Liu, Q. A. Huang, and W. Li, "Analysis of optimized micro-rotating-structure for MEMS," *Int. Conf. Solid-State Integr. Circuits Technol. Proceedings, ICSICT*, vol. 3, pp. 1747–1750, 2004, doi: 10.1109/icsict.2004.1435171.

[79] A. Sharma *et al.*, "Fabrication and analysis of MEMS test structures for residual stress measurement," *Sensors and Transducers*, vol. 13, no. SPEC.ISSUE, pp. 21–30, 2011.

[80] A. Potekhina and C. Wang, “Review of electrothermal actuators and applications,” *Actuators*, vol. 8, no. 4, 2019, doi: 10.3390/ACT8040069.

[81] M. Verotti, R. Crescenzi, M. Balucani, and N. P. Belfiore, “MEMS-based conjugate surfaces flexure hinge,” *J. Mech. Des.*, vol. 137, no. 1, 2015, doi: 10.1115/1.4028791.

[82] A. Buzzin, S. Cupo, E. Giovine, G. de Cesare, and N. P. Belfiore, “Compliant nano-pliers as a biomedical tool at the nanoscale: Design, simulation and fabrication,” *Micromachines*, vol. 11, no. 12, pp. 1–13, 2020, doi: 10.3390/mi11121087.

[83] M. Tecpoyotl-Torres, P. Vargas-Chable, S. Robles-Casolco, and R. Cabello-Ruiz, “Dynamic Analysis of a Microgripper and Its Components,” *Br. J. Appl. Sci. Technol.*, vol. 9, no. 4, pp. 360–373, 2015, doi: 10.9734/bjast/2015/18042.

[84] K. E. Petersen, “Silicon as a Mechanical Material,” *Proc. IEEE*, vol. 70, no. 5, pp. 420–457, 1982, doi: 10.1109/PROC.1982.12331.

[85] H. Chang *et al.*, “A rotary comb-actuated microgripper with a large displacement range,” *Microsyst. Technol.*, vol. 20, no. 1, pp. 119–126, 2014, doi: 10.1007/s00542-013-1737-8.

[86] Q. Gao, D. Zhang, D. Xu, and Z. Zhang, “A kinematics modeling and stress analysis method for flexible micro-gripper,” *2012 IEEE Int. Conf. Mechatronics Autom. ICMA 2012*, pp. 825–830, 2012, doi: 10.1109/ICMA.2012.6283249.

[87] X. Sun *et al.*, “A novel piezo-driven microgripper with a large jaw displacement,” *Microsyst. Technol.*, vol. 21, no. 4, pp. 931–942, 2015, doi: 10.1007/s00542-014-2199-3.

[88] N. Lobontiu and E. Garcia, “Analytical model of displacement amplification and stiffness optimization for a class of flexure-based compliant mechanisms,” *Comput. Struct.*, vol. 81, no. 32, pp. 2797–2810, 2003, doi: 10.1016/j.compstruc.2003.07.003.

[89] C. Liang *et al.*, “A novel monolithic piezoelectric actuated flexure-mechanism based wire clamp for microelectronic device packaging,” *Rev. Sci. Instrum.*, vol. 86, no. 4, 2015, doi: 10.1063/1.4918621.

[90] K. Shrivastava, and S. S. Joshi, “Design and development of compliant microgripper-based assembly station,” *Proceedings of the ASME 2016 International Mechanical Engineering Congress and Exposition*, no. i, pp. 1–8, 2017.

[91] Y. L. Yang, Y. D. Wei, J. Q. Lou, G. Tian, X. W. Zhao, and L. Fu, “A new piezo-driven microgripper based on the double-rocker mechanism,” *Smart Mater. Struct.*, vol. 24, no. 7, 2015, doi: 10.1088/0964-1726/24/7/075031.

[92] Y. Zhu, A. Corigliano, and H. D. Espinosa, “A thermal actuator for nanoscale in situ microscopy testing: Design and characterization,” *J. Micromechanics Microengineering*, vol. 16, no. 2, pp. 242–253, 2006, doi: 10.1088/0960-1317/16/2/008.

[93] M. Tecpoyotl-T., P. Vargas Ch., S. Koshevaya, R. Cabello-R., A. Ocampo-D., and J. G. Vera-D., “Design and simulation of a MEM pressure microgripper based on electrothermal microactuators,” *Thin Film. Sol. Energy Technol. VIII*, vol. 9936, no. October, p. 99360I, 2016, doi: 10.1117/12.2237533.

[94] H. Steiner, F. Keplinger, J. Schalko, W. Hortschitz, and M. Stifter, “Highly Efficient Passive Thermal Micro-Actuator,” *J. Microelectromechanical Syst.*, vol. 24, no. 6, pp. 1981–1988, 2015, doi: 10.1109/JMEMS.2015.2457094.

[95] D. H. Norrie, *A first course in the finite element method*, vol. 3, no. 2. 1987.

[96] C. Wu, R. Zhang, W. Du, L. Cheng, and G. Liang, *Alkaline phosphatase-triggered self-assembly of near-infrared nanoparticles for the enhanced photoacoustic imaging of tumors*, 1st ed., vol. 657. Elsevier Inc., 2021.

[97] Susan Pratt, “Environmental Compensation on the AD7142: The Effects of Temperature and Humidity on Capacitance Sensors,” pp. 1–8, 2005, [Online]. Available: https://www.analog.com/media/en/technicaldocumentation/application-notes/AN-829.pdf.

[98] A. S. Algamili *et al.*, “A Review of Actuation and Sensing Mechanisms in MEMS-Based Sensor Devices,” *Nanoscale Res. Lett.*, vol. 16, no. 1, 2021, doi: 10.1186/s11671-021-03481-7.

[99] L. F. Zhao, Z. F. Zhou, M. Z. Meng, M. J. Li, and Q. A. Huang, "An efficient electro-thermo-mechanical model for the analysis of V-shaped thermal actuator connected with driven structures," *Int. J. Numer. Model. Electron. Networks, Devices Fields*, vol. 34, no. 3, pp. 1–14, 2021, doi: 10.1002/jnm.2843.

[100] P. J. French *et al.*, "The development of a low-stress polysilicon process compatible with standard device processing," *J. Microelectromechanical Syst.*, vol. 5, no. 3, pp. 187–196, 1996, doi: 10.1109/84.536625.

[101] ReliaSoft Corporation, "Experiment Design & Analysis Reference," p. 368, 2015, [Online]. Available: http://reliawiki.com/index.php/Experiment_Design_and_Analysis_Reference.

[102] J. Ramakrishnan, P. T. R. Gaurav, N. S. Chandar, and N. M. Sudharsan, "Structural design, analysis and DOE of MEMS-based capacitive accelerometer for automotive airbag application," *Microsyst. Technol.*, vol. 27, no. 3, pp. 763–777, 2021, doi: 10.1007/s00542-020-04979-3.

[103] M. M. Saleem and A. Somá, "Design of experiments based factorial design and response surface methodology for MEMS optimization," *Microsyst. Technol.*, vol. 21, no. 1, pp. 263–276, 2015, doi: 10.1007/s00542-014-2186-8.

[104] P. Bhattacharjee, K. R. Kumar, and T. A. J. Reddy, "Structural reliability evaluation of a pressure vessel using Response Surface method," *Proc. 2009 8th Int. Conf. Reliab. Maintainab. Safety, ICRMS 2009*, pp. 972–977, 2009, doi: 10.1109/ICRMS.2009.5269978.

[105] R. G. Budynas, *Advanced strength and Applied Stress Analysis*, Second edition, 1999.

[106] Y. Gangamwar, V. Deo, S. Chate, M. Bhandare, and P. H. N. Deshpande, "Determination of Curved Beam Deflection by Using Castigliano's Theorem," *Int. J. Res. Emerg. Sci. Technol.*, no. 3, 2016.

[107] Y. Gangamwar, S. Chate, M. Bhandare, V. Deo, and H. N. Deshpande, “Analytical, Experimental Determination of Deflection of Curved Beams and its Validation,” *Int. J. Innov. Res. Sci. Eng. Technol. (An ISO*, vol. 3297, 2007, doi: 10.15680/IJIRSET.2015.0506158.

[108] M. F. Pantano, R. A. Bernal, L. Pagnotta, and H. D. Espinosa, “Multiphysics design and implementation of a microsystem for displacement-controlled tensile testing of nanomaterials,” *Meccanica*, vol. 50, no. 2, pp. 549–560, 2015, doi: 10.1007/s11012-014-9950-9.

[109] M. Huff, “Review Paper: Residual Stresses in Deposited Thin-Film Material Layers for Micro- and Nano-Systems Manufacturing,” *Micromachines*, vol. 13, no. 12, 2022, doi: 10.3390/mi13122084.

[110] H. Moriceau, F. Fournel, and F. Rieutord, *Materials and manufacturing techniques for silicon-on-insulator (SOI) wafer technology*. Woodhead Publishing Limited, 2014.

[111] T. E. Rudenko, A. N. Nazarov, and V. S. Lysenko, “The advancement of silicon-on-insulator (SOI) devices and their basic properties,” *Semicond. Physics, Quantum Electron. Optoelectron.*, vol. 23, no. 3, pp. 227–252, 2020, doi: 10.15407/spqeo23.03.227.

[112] N. P. Belfiore *et al.*, “Design, fabrication, testing and simulation of a rotary double comb drives actuated microgripper,” *Micromachines*, vol. 12, no. 10, pp. 1–21, 2021, doi: 10.3390/mi12101263.

[113] A. Bagolini, S. Ronchin, P. Bellutti, M. Chistè, M. Verotti, and N. P. Belfiore, “Fabrication of Novel MEMS Microgrippers by Deep Reactive Ion Etching With Metal Hard Mask,” *J. Microelectromechanical Syst.*, vol. 26, no. 4, pp. 926–934, 2017, doi: 10.1109/JMEMS.2017.2696033.

[114] A. Bagolini, P. Scauso, S. Sanguinetti, and P. Bellutti, “Silicon Deep Reactive Ion Etching with aluminum hard mask,”vol. 6, no. 8, pp. 0–6, 2020, doi: 10.1088/2053-1591/ab2423.

[115] A. P. Malshe, W. P. Eaton, and C. O. Neal, “Challenges in the Packaging of MEMS,” *International Symposium on Advanced Packaging Materials*, 1999.